nature COMMUNICATIONS

ARTICLE

https://doi.org/10.1038/s41467-021-27852-x OPEN

Biosensor for branched-chain amino acid metabolism in yeast and applications in isobutanol and isopentanol production

Yanfei Zhang[1], Jeremy D. Cortez[2,6], Sarah K. Hammer[1,6], César Carrasco-López[1], Sergio Á. García Echauri[1], Jessica B. Wiggins[3], Wei Wang[3] & José L. Avalos[1,2,4,5]✉

Branched-chain amino acid (BCAA) metabolism fulfills numerous physiological roles and can be harnessed to produce valuable chemicals. However, the lack of eukaryotic biosensors specific for BCAA-derived products has limited the ability to develop high-throughput screens for strain engineering and metabolic studies. Here, we harness the transcriptional regulator Leu3p from *Saccharomyces cerevisiae* to develop a genetically encoded biosensor for BCAA metabolism. In one configuration, we use the biosensor to monitor yeast production of isobutanol, an alcohol derived from valine degradation. Small modifications allow us to redeploy Leu3p in another biosensor configuration that monitors production of the leucine-derived alcohol, isopentanol. These biosensor configurations are effective at isolating high-producing strains and identifying enzymes with enhanced activity from screens for branched-chain higher alcohol (BCHA) biosynthesis in mitochondria as well as cytosol. Furthermore, this biosensor has the potential to assist in metabolic studies involving BCAA pathways, and offers a blueprint to develop biosensors for other products derived from BCAA metabolism.

[1] Department of Chemical and Biological Engineering, Princeton University, Princeton, NJ, USA. [2] Department of Molecular Biology, Princeton University, Princeton, NJ, USA. [3] Genomics Core Facility, Lewis-Sigler Institute for Integrative Genomics, Princeton University, Princeton, NJ, USA. [4] Andlinger Center for Energy and the Environment, Princeton University, Princeton, NJ, USA. [5] High Meadows Environmental Institute, Princeton University, Princeton, NJ, USA. [6] These authors contributed equally: Jeremy D. Cortez, Sarah K. Hammer. ✉email: javalos@princeton.edu

The metabolism of branched chain amino acids (BCAAs), including valine, leucine, and isoleucine is central to microbial production of many valuable products[1–8]. Among microbial hosts that produce BCAAs and BCAA-derived compounds, the yeast *Saccharomyces cerevisiae* is a favored industrial organism due to its genetic tractability, resistance to phage contamination, and ability to grow at low pH and high alcohol concentrations[9]. However, the rate at which genetic diversity can be introduced in strains greatly outpaces the rate at which they can be screened for production; and, unfortunately, there are currently no eukaryotic biosensors specific for individual BCAAs and their derived products, which could be used to develop high-throughput screens and accelerate strain development[10–15].

BCAA and BCAA-derived product biosynthesis originates from mitochondrial pyruvate[16] (Supplementary Fig. 1). In the biosynthesis of valine and leucine, an acetolactate synthase (ALS, encoded by *ILV2*) first catalyzes the condensation of two pyruvate molecules to produce acetolactate. The subsequent activities of a ketol-acid reductoisomerase (KARI, encoded by *ILV5*), and a dehydroxyacid dehydratase (DHAD, encoded by *ILV3*) yield α-ketoisovalerate (α-KIV), the precursor to valine. Next, α-KIV is acetylated in either mitochondria or the cytosol by α-isopropylmalate (α-IPM) synthases (encoded by *LEU4* and *LEU9*) to produce α-IPM. In the cytosol, α-IPM is converted by isopropylmalate isomerase (encoded by *LEU1*) and β-isopropylmalate dehydrogenase (encoded by *LEU2*) to α-ketoisocaproate (α-KIC), the precursor to leucine. Isoleucine biosynthesis resembles that of valine; however for isoleucine, Ilv2p condenses pyruvate with α-ketobutyrate derived from threonine. Subsequent Ilv5p and Ilv3p activity produces α-keto-3-methylvalerate (α-K3MV), the precursor to isoleucine. Finally, the three α-ketoacid precursors (α-KIV, α-KIC, and α-K3MV) are transaminated by branched-chain amino acid aminotransferases in mitochondria (encoded by *BAT1*) and cytosol (encoded by *BAT2*) to produce valine, leucine, and isoleucine, respectively[16] (Supplementary Fig. 1).

Many biosensors are based on transcription factors (TFs) that activate expression of a reporter gene, such as green fluorescent protein (GFP), in response to elevated concentrations of a specific molecule, which may be a product of interest, by-product, or precursor[12,13,17–19]. Leu3p is a yeast TF that regulates several genes in BCAA biosynthesis in response to selectively binding to α-IPM, acting as an activator in the presence of α-IPM and a repressor in its absence[20–22]. Because α-IPM is a by-product of valine biosynthesis and an intermediate of leucine biosynthesis (Supplementary Fig. 1), its levels are correlated to the activity of both pathways. This makes Leu3p an ideal TF to use in a biosensor for BCAA metabolic activity, which could enable high-throughput screens for production of BCAA-derived products such as branched-chain higher alcohols (BCHAs).

There is great interest in producing BCHAs, as they are among the top ten advanced biofuels identified by the U.S. Department of Energy for their potential to boost gasoline engine efficiency[23,24], and can be upgraded to renewable jet fuel[25]. BCHA production can be enhanced by overexpressing enzymes from the Ehrlich degradation pathway[26]. In this pathway, α-ketoacid decarboxylases (α-KDCs) and alcohol dehydrogenases (ADHs) convert the α-ketoacid precursors α-KIV, α-KIC, and α-K3MV to isobutanol, isopentanol, and 2-methyl-1-butanol, respectively (Supplementary Fig. 1).

Here, we report the development and application of a genetically encoded biosensor for eukaryotic BCAA metabolism and BCHA biosynthesis. The biosensor is based on the α-IPM-dependent function of Leu3p to control expression of GFP. Two biosensor configurations enable high-throughput screening for improved isobutanol or isopentanol production. These two configurations differ mechanistically, by monitoring α-IPM as either a by-product of isobutanol or a precursor of isopentanol. We apply the biosensor to isolate high-producing strains, identify mutant enzymes with enhanced activity, and construct biosynthetic pathways for production of isobutanol and isopentanol in both mitochondria and cytosol. This biosensor has the potential to accelerate the development of yeast strains to produce BCHAs as well as other products derived from BCAA metabolism.

Results

Design and construction of a biosensor for branched-chain higher alcohol biosynthesis. To construct a biosensor for BCHAs, isobutanol and isopentanol, we introduced a copy of yeast-enhanced green fluorescent protein (yEGFP) under the control of the Leu3p-regulated *LEU1* promoter (P_{LEU1}) and a constitutively expressed leucine-insensitive Leu4p mutant. We tested 8 different biosensor constructs using 4 different Leu4p variants, and the yEGFP tagged or untagged with a proline-glutamate-serine-threonine-rich (PEST) protein degradation tag[27] to test different stability levels of the reporter. We compared the change in fluorescence caused by overexpressing the BCHA biosynthetic pathway in strains with or without a *LEU2* deletion, which respectively favors isobutanol or isopentanol production, in a total of 16 different strains (Supplementary Note 1). When *LEU2* is deleted, the construct using a Leu4p variant with a truncated leucine regulatory domain ($Leu4^{1-410}$) and a PEST-tagged yEGFP gives the largest change in fluorescence (Supplementary Fig. 2a). The better performance of the PEST-tagged yEGFP is consistent with the expected accumulation of IPM molecules when *LEU2* is deleted (Supplementary Fig. 1), which would boost Leu3p activation and lead to higher background (Supplementary Note 1). In contrast, when *LEU2* is present, having a Leu4p variant with a Ser547 deletion ($Leu4^{\Delta S547}$)[28] and untagged yEGFP shows the largest difference in fluorescence (Supplementary Fig. 2b). This is consistent with lower α-IPM concentrations due to Leu2p activity, which lowers Leu3p background activation and thus requires higher stability of yEGFP for enhanced biosensor sensitivity. We also found that deleting the endogenous *LEU4* and *LEU9* reduces the biosensor background in *LEU2* strains (Supplementary Note 1). Because *LEU2* favors isopentanol production, while *LEU2* deletion favors isobutanol, the constructs containing yEGFP-PEST/$LEU4^{1-410}$/*leu2Δ* (henceforth called the isobutanol configuration) and yEGFP/$Leu4^{\Delta S547}$/*LEU2*/*leu4Δ*/ *leu9Δ* (henceforth called the isopentanol configuration) make suitable biosensor configurations to screen for improved isobutanol and isopentanol production, respectively (Fig. 1a, c).

To characterize the biosensor in the isobutanol configuration, we measured its response to key metabolites supplemented in the growth medium as well as to enhanced isobutanol biosynthesis in engineered strains. We found that the fluorescence emitted by the biosensor responds linearly to increasing concentrations of α-IPM ($R^2 = 0.96$, Supplementary Fig. 3a) or α-KIV ($R^2 = 0.97$, Supplementary Fig. 3b) supplemented in the media at concentrations below 80 μM. At higher concentrations, the response loses linearity, possibly due to cellular import bottlenecks of α-IPM and α-KIV (Supplementary Fig. 3c, d, and Supplementary Note 2). In contrast, the biosensor does not respond to the isoleucine precursor α-K3MV, when supplemented in the media (Supplementary Fig. 3e, f). We next examined the correlation between GFP fluorescence and isobutanol production in strains containing the biosensor and different constructions of the BCHA biosynthetic pathway, resulting in varying levels of isobutanol production. We found that there is a strong linear correlation ($R^2 = 0.97$) between GFP fluorescence during the exponential phase and total isobutanol biosynthesis (Fig. 1b), providing a

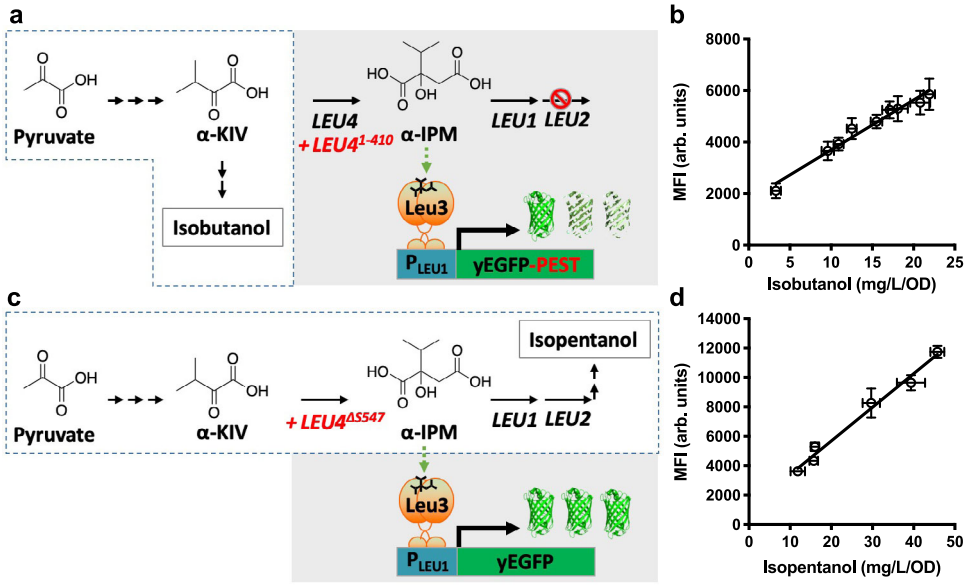

Fig. 1 Design and characterization of two BCHA biosensor configurations. a Schematics of the biosensor in the isobutanol configuration (gray box) and simplified isobutanol pathway (enclosed by dashed lines; each arrow represents one enzymatic step). The α-isopropylmalate (α-IPM), which activates Leu3p (green dashed arrow), is an isobutanol by-product that accumulates due to deletion of *LEU2*. Thus, adding a PEST tag to destabilize yEGFP reduces background. α-KIV, α-ketoisovalerate. **b** Correlation between specific isobutanol titers (mg/L/OD) produced by engineered strains and GFP median fluorescence intensity (MFI) from the isobutanol biosensor. Strains used (from left to right): YZy121, YZy230, YZy81, YZy231, YZy232, YZy233, YZy234, YZy235, and YZy236 (Supplementary Table 1). **c** Schematics of the biosensor in the isopentanol configuration (gray box) and simplified isopentanol pathway (enclosed by dashed lines; each arrow represents one enzymatic step). In this case, α-IPM is an isopentanol precursor that does not accumulate due to *LEU2* activity, so the PEST tag on yEGFP is not required. **d** Correlation between specific isopentanol titers (mg/L/OD) produced by engineered strains and GFP median fluorescence intensity (MFI) from the isopentanol biosensor. Strains used (from left to right): SHy187, SHy188, SHy192, SHy159, SHy176, and SHy158 (Supplementary Table 1). The MFI for each strain was measured 13 h after inoculation, during the exponential phase, and plotted against the corresponding specific isobutanol or isopentanol titers obtained after 48-h high-cell-density fermentations. MFI are represented in arbitrary units (arb. units). All data are shown as mean values. Error bars represent the standard deviation of at least three biological replicates. Source data are provided as a Source Data file.

conservative estimate of its dynamic range (Supplementary Note 2). Moreover, measuring the intracellular α-IPM concentrations of an isobutanol-producing strain against a control strain (see Methods) revealed that Leu3p-sensing of α-IPM concentrations during exponential growth is predictive of the total isobutanol produced by the end of the fermentation (Supplementary Fig. 4a–c and Supplementary Note 3). These results validate the applicability of this biosensor to measure isobutanol production in yeast.

We next validated the efficacy of the biosensor in the isopentanol configuration. To achieve this, we measured the fluorescence of several *LEU2* strains containing this biosensor configuration and various constructs of the BCHA biosynthetic pathway, resulting in different levels of isopentanol production. We found a strong linear correlation ($R^2 = 0.98$) between the biosensor fluorescence during the exponential phase and total isopentanol production by the end of the fermentation (Fig. 1d and Supplementary Note 2). Time-course measurements of fluorescence and intracellular α-IPM concentrations of an isopentanol-producing strain revealed that the biosensor in this configuration is highly sensitive to small differences in α-IPM (Supplementary Fig. 4d–f). Interestingly, fluorescence measurements of strains with the biosensor in the isopentanol configuration do not correlate to isobutanol production (Supplementary Fig. 5). Therefore, mechanistic differences between the biosensor configurations allow them to measure specifically either isobutanol or isopentanol production (Supplementary Note 3).

Using the biosensor to isolate high-isobutanol-producing strains. We applied the isobutanol configuration of the biosensor to isolate the highest isobutanol producers from a library of strains containing random combinations of genes from the mitochondrial isobutanol biosynthesis pathway[29]. Equal molar amounts of cassettes containing either upstream *ILV* genes (*ILV2, ILV3*, and *ILV5*), downstream Ehrlich pathway genes (KDC and ADH), or the full isobutanol pathway, all designed to randomly integrate into YARCdelta5 δ-sites[29,30], were pooled and used to transform strain YZy81, which has the biosensor in the isobutanol configuration (Supplementary Tables 1, 2). After subjecting the transformed population to two rounds of fluorescence activated cell sorting (FACS, see Methods), 11 out of 24 randomly chosen colonies produce more than 600 mg/L isobutanol. This is more than twice the mean isobutanol titer (268 mg/L) obtained from 24 random colonies from the unsorted population; in fact, none of the unsorted colonies produced more than 600 mg/L and only one produced more than 500 mg/L (Fig. 2). Additionally, using digital droplet PCR (see methods), we found only two different genotypes in the top 6 isobutanol-producing strains (those producing 700 mg/L isobutanol or more), suggesting a substantial enrichment from the ~2×10^5 individual transformants in the original library (Supplementary Table 3). These results demonstrate that the isobutanol biosensor configuration enables high-throughput screening with FACS to isolate high-isobutanol producers from mixed strain populations.

Applying the isobutanol configuration of the biosensor to identify ILV6 mutants insensitive to valine inhibition. We next utilized the isobutanol biosensor configuration to identify mutants of the acetolactate synthase regulatory protein, encoded by *ILV6*, with reduced feedback inhibition from valine. Ilv6p

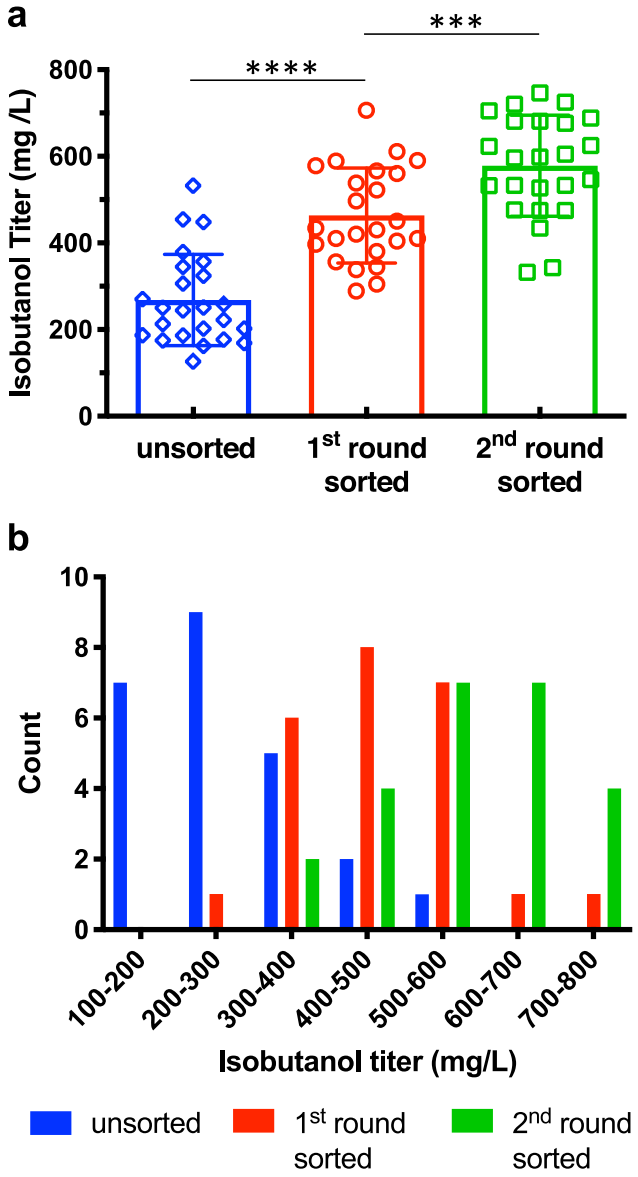

Fig. 2 Applying the biosensor in its isobutanol configuration for high-throughput screening of a library of strains combinatorially transformed with the mitochondrial isobutanol biosynthetic pathway. a Isobutanol titers of 24 colonies randomly selected from unsorted (blue), first round sorted (red), or second round sorted (green) populations derived from a library of strains transformed with constructs overexpressing different combinations of the mitochondrial isobutanol pathway. All data are shown as mean values. Error bars represent the standard deviation of the titers of the 24 colonies analyzed. A two-sided *t*-test was used to determine the statistical significance of the differences in isobutanol titers of analyzed strains from each population; From left to right: $P < 0.0001$, $P = 0.001$; $^{***}P \leq 0.001$, $^{****}P \leq 0.0001$. **b** Histogram showing the number of colonies exhibiting different ranges of isobutanol production, out of the same 24 randomly selected strains from the unsorted (blue), first round sorted (red), or second round sorted (green) populations shown in (**a**). Source data are provided as a Source Data file.

localizes to mitochondria where it interacts with acetolactate synthase, Ilv2p, both enhancing its activity and bestowing upon it feedback inhibition by valine[31,32] (Fig. 3a). Mutations identified in the Ilv6p homolog from *Streptomyces cinnamonensis* (IlvN) that confer resistance to valine analogues[33] informed the design of an Ilv6p$^{V90D/L91F}$ mutant, which has been shown to retain Ilv2p activation, have reduced sensitivity to valine inhibition, and improve isobutanol production[34,35]. However, these mutations are likely not unique or optimal. If alternative mutations exist, some potentially conferring higher Ilv2p/Ilv6p complex activity, we hypothesized that we could find them with the aid of our BCHA biosensor.

To find Ilv6p mutants insensitive to valine inhibition, we used the isobutanol biosensor configuration to isolate highly fluorescent strains transformed with libraries of randomly mutagenized *ILV6* and grown in the presence of valine. To avoid biosensor signal interference, the parent strain of these libraries (YZy91) contains *BAT1* and *BAT2* deletions, which eliminates interconversion between valine and α-KIV, as well as an *ILV6* deletion to rule out endogenous valine inhibition of Ilv2p (Supplementary Table 1, Fig. 3a). Two libraries, generated via error-prone PCR of either the wild-type *ILV6* or the *ILV6*$^{V90D/L91F}$ variant, were used separately to transform YZy91. After culturing the two resulting yeast libraries in media containing excess valine (see Methods) and three rounds of FACS, we measured the isobutanol production of 24 colonies randomly picked from each sorted library. All 48 colonies randomly selected after the third round of sorting show higher fluorescence and isobutanol production in the presence of valine than the strain overexpressing wild-type *ILV6* (Supplementary Fig. 6), demonstrating an undetectable low rate of false positives.

We next analyzed the *ILV6* mutations found in the sorted strains. First, we tested whether each *ILV6* mutant was responsible for the enhanced isobutanol production and biosensor signal by curing each strain of the plasmid that contains it (expecting a return to parental phenotypes), as well as by re-transforming the parental strain (YZy91) with each isolated plasmid (expecting a return to enhanced phenotypes). These experiments confirmed that the *ILV6* mutants indeed confer the enhanced phenotypes (Fig. 3b and Supplementary Fig. 7), although the retransformation experiments in some strains suggest that additional background mutations attenuate (e.g., strain 8) or boost (e.g., strain 11) the effects of these mutants. Sequencing the 48 isolated plasmids revealed 24 unique sequences and several previously unknown *ILV6* mutations that achieve similar or higher levels of isobutanol production than the previously known *ILV6*$^{V90D/L91F}$ (Supplementary Table 4). Variant 6, with a single mutation at Val110 (V110E), produces the most isobutanol (378 mg/L ± 10 mg/L), which is a 3.2-fold increase over the wild-type *ILV6*, and a small but statistically significant ($P = 0.0055$) improvement over the previously identified *ILV6*$^{V90D/L91F}$ mutant (Fig. 3b). When we overexpress this *ILV6*^{V110E} variant in a strain containing the mitochondrial isobutanol biosynthetic pathway, the production is 1.6 times higher than the equivalent strain overexpressing the wild-type *ILV6* (Fig. 3c). Mapping the mutations found in our isolated variants onto the crystal structure of the bacterial Ilv6p homologue IlvH revealed that most of the mutations are located in the regulatory valine binding domain (Supplementary Note 4 and Supplementary Fig. 8). Although the biosensor is able to aid in identifying both previously reported and unknown mutations that increase isobutanol production relative to wild-type *ILV6*, none of the previously unknown mutants achieve a substantial improvement in isobutanol production relative to *ILV6*$^{V90D/L91F}$. This could be because *ILV6*$^{V90D/L91F}$ enhances Ilv2p activity to an extent that is near the maximum achievable through Ilv6p engineering alone, or because the pathway bottleneck is no longer at the Ilv2p metabolic step after *ILV6*$^{V90D/L91F}$ is overexpressed.

Applying the isopentanol configuration of the biosensor to identify highly active LEU4 mutants. We next applied our

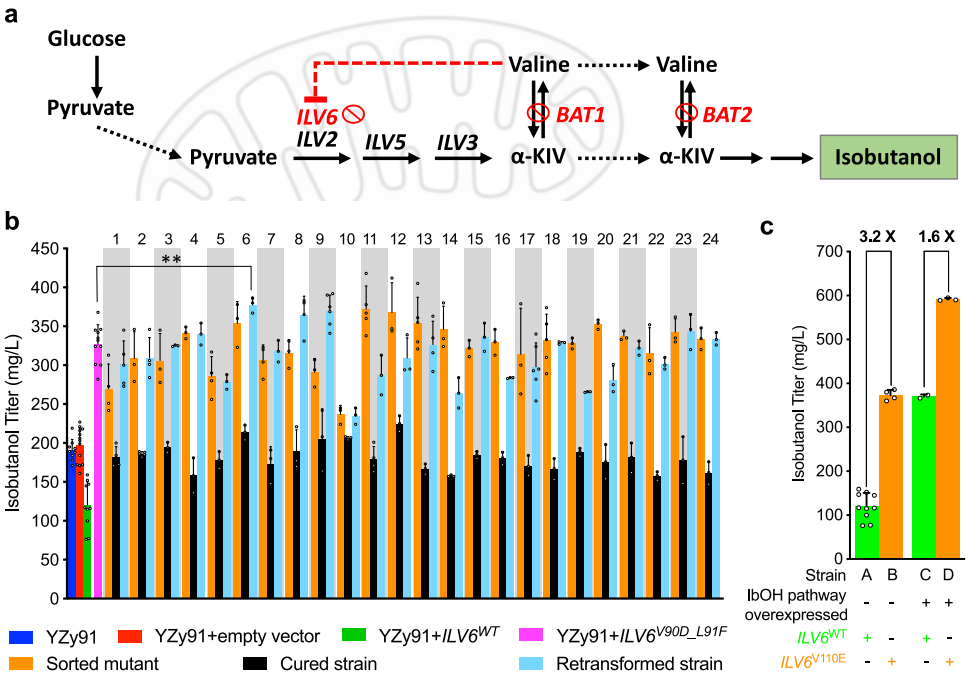

Fig. 3 High-throughput screen for metabolically hyperactive Ilv6p mutants using the biosensor in its isobutanol configuration. a Schematic representation of the genotype of the basal strain, YZy91, used for high-throughput screening of Ilv6p mutants with enhanced activity in the presence of valine; α-KIV: α-ketoisovalerate. Mitochondrion image created with BioRender. **b** Isobutanol titers after 48 h fermentations of sorted strains with unique *ILV6* mutant sequences (orange), plasmid-cured derivatives (black), and strains obtained from retransforming YZy91 with each unique plasmid isolated from the corresponding sorted strain (cyan). Titers obtained from YZy91 with (red) or without (blue) an empty vector, or transformed with plasmids containing $ILV6^{WT}$ (green) or $ILV6^{V90D\_L91F}$ (magenta), are shown as controls. The numbers on the upper x-axis identify each of the strains harboring screened mutants with unique *ILV6* sequences. *ILV6* mutants 1–10 were isolated from the sorted wild-type *ILV6* ($ILV6^{WT}$) mutagenesis library. *ILV6* mutants 11–24 were isolated from the sorted $ILV6^{V90D\_L91F}$ mutagenesis library. A two-sided *t*-test was used to determine the statistical significance of the difference in isobutanol titers between YZy91 with $ILV6^{V90D\_L91F}$ (magenta) and $ILV6^{V110E}$ (*ILV6* mutant #6). $P = 0.0055$; $^{**}P \leq 0.01$. **c** Isobutanol titers of YZy91 transformed with CEN plasmids containing $ILV6^{WT}$ (Strain A) or $ILV6^{V110E}$ (*ILV6* mutant #6, Strain B) compared to titers from a strain overexpressing the mitochondrial isobutanol pathway (YZy363) transformed with CEN plasmids containing $ILV6^{WT}$ (Strain C) or $ILV6^{V110E}$ (*ILV6* mutant #6, Strain D). All data are shown as mean values. Open circles represent individual data points. Error bars represent the standard deviation of at least three biological replicates. Source data are provided as a Source Data file.

biosensor in the isopentanol configuration to identify *LEU4* mutants with enhanced enzymatic activity. While the isopentanol configuration utilizes a *LEU4* mutant previously shown to have reduced sensitivity to leucine inhibition[28,36], we sought to identify a variant that is not only insensitive to leucine inhibition, but more catalytically active. To do so, we constructed two overexpression libraries of randomly mutagenized *LEU4* (using error-prone PCR): one with full-length *LEU4* mutagenized, and another with only the leucine regulatory domain mutagenized (residues 430–619). These libraries were separately used to transform a *ΔBAT1/ΔLEU4/ΔLEU9* strain containing a modified isopentanol configuration of the biosensor lacking the $LEU4^{\Delta S547}$ (YZy148, Supplementary Tables 1 and 2). Two major sub-populations in the full-length *LEU4* library (ep_Leu4) were observed during growth in the presence of leucine (Fig. 4a). The larger sub-population overlaps with the signal from the empty vector control, suggesting that most mutations are deleterious to Leu4p activity, and thus α-IPM synthesis. However, the smaller sub-population retains activity, with a substantial fraction exhibiting higher GFP fluorescence intensity than the wild-type *LEU4*. In contrast, the library derived from mutagenizing only the regulatory domain of *LEU4* (ep_Leu4_Reg) is dominated by a single population with a higher median GFP signal than wild-type *LEU4* (Fig. 4a), suggesting that many mutations in the regulatory domain enhance Leu4p enzymatic activity in the presence of leucine.

After three rounds of FACS, both sorted populations display increased median fluorescence intensity (Fig. 4b). The isopentanol production of 48 colonies randomly selected from the third round of sorting ranged between 375 mg/L and 725 mg/L (Fig. 4c and Supplementary Fig. 9), which represent 1.9- to 3.6-fold improvements over the strain overexpressing the wild-type *LEU4*. Similar to the isobutanol configuration, these results indicate that the isopentanol configuration displays a low (undetectable) rate of false positives. Taking the same approach as in the *ILV6* experiments above, we cured each strain from its *LEU4*-containing plasmid and retransformed the parent strain (YZy148) with the same extracted plasmids to compare fluorescence intensity (Supplementary Fig. 10) and isopentanol production (Fig. 4c) between the sorted, cured, and retransformed strains. Notably, the strain retransformed with mutant #6 achieves the highest isopentanol titer (963 mg/L ± 32 mg/L), which is 4.8-times higher than the titer achieved by overexpressing the wild-type *LEU4*, and significantly higher than the titer obtained with the $LEU4^{\Delta S547}$ mutant previously described[37] (842 mg/L ± 23 mg/L; *P*-value = 0.0021).

Sequencing the plasmids contained in the 48 randomly selected colonies (Supplementary Fig. 9), revealed 24 unique *LEU4* variants (Supplementary Table 5). Several newly found mutations may contribute to reduced regulation, enhanced catalytic activity, or both. Five variants have single mutations (H541R, Y485N, Y538N, V584E, and T590I), all of which are located in the regulatory domain of Leu4p (Supplementary Note 5 and Supplementary Fig. 11). Although we have not yet elucidated the combined effects of multiple amino acid substitutions in variants containing two or more mutations, seven residues (K51,

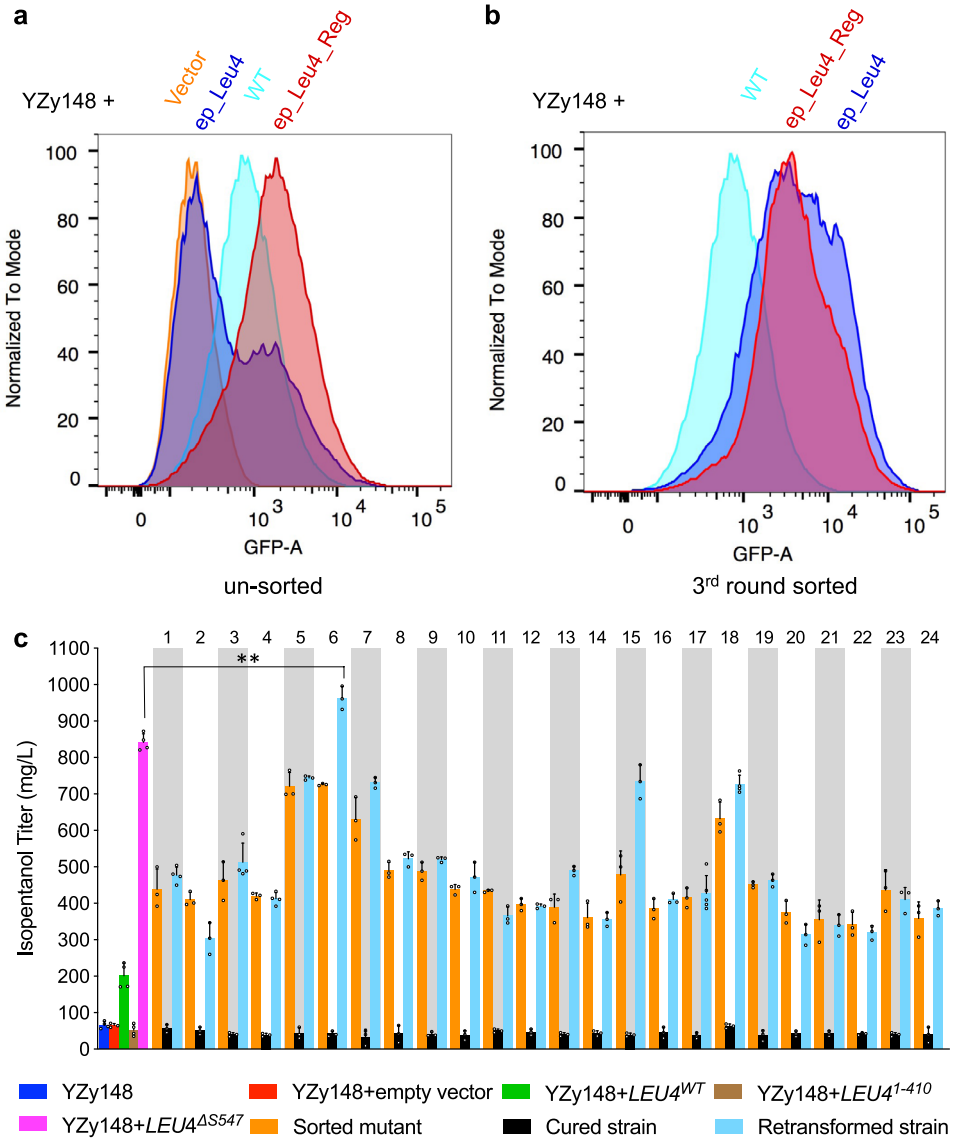

Fig. 4 High-throughput screen for hyperactive Leu4p variants using the isopentanol configuration of the biosensor. a Flow cytometry analysis of yeast libraries containing *LEU4* variants generated with error-prone PCR-based mutagenesis of the full-length *LEU4* (ep_Leu4, blue) or only the *LEU4* regulatory domain (ep_Leu4_Reg, red), compared to control strains containing an empty vector (Vector, orange) or wild-type *LEU4* (WT, cyan). Cell populations were normalized to the mode for comparison. **b** Flow cytometry analysis of the same libraries depicted in (**a**) after three rounds of FACS. **c** Isopentanol titers after 48 h fermentations of sorted strains with unique *LEU4* sequences (orange), plasmid-cured derivatives (black), and strains obtained from retransforming YZy148 with each unique plasmid isolated from the corresponding sorted strain (cyan). Titers obtained from the basal strain YZy148 (*leu4Δ leu9Δ bat1Δ LEU2*) with (red) or without (blue) an empty vector, or transformed with plasmids containing wild-type *LEU4* ($LEU4^{WT}$, green), $LEU4^{1\text{–}410}$ (brown), or $LEU4^{\Delta S547}$ (magenta), are shown as controls. The numbers on the upper x-axis identify each strain harboring a unique *LEU4* sequence. *LEU4* mutants 1–13 are derived from mutagenizing the full-length *LEU4*; and mutants 14–24 from mutagenizing the *LEU4* leucine regulatory domain. All data are shown as mean values. Open circles represent individual data points. Error bars represent the standard deviation of at least three biological replicates. A two-sided *t*-test was used to determine the statistical significance of the difference between isopentanol titers achieved by YZy148 transformed with a plasmid containing $LEU4^{\Delta S547}$ (magenta), or *LEU4* mutant #6 ($LEU4^{E86D\_K191N\_K374R\_A445T\_S481R\_N515I\_A568V\_S601A}$). $P = 0.0021$; $^{**}P \leq 0.01$. Source data are provided as a Source Data file.

Q439, F497, N515, V584, D578, and T590) are substituted in more than one variant (Supplementary Tables 5, 6), suggesting they are involved in enhancing Leu4p activity. Thus, our biosensor was able to identify 12 previously unreported residues in Leu4p that enhance isopentanol production when mutated (Supplementary Note 5).

Biosensor-assisted cytosolic isobutanol pathway engineering. The demonstrations above involve strains engineered with the BCHA biosynthetic pathway compartmentalized in mitochondria[29]; however, cytosolic pathways for isobutanol production have also been developed[38–41]. To investigate whether the isobutanol-configured biosensor can help improve pathways compartmentalized in either compartment, we used it to optimize an isobutanol pathway contained entirely in the cytosol, comprised of heterologous ALS, KARI, and DHAD (*ILV*) genes. We deleted *ILV3* from strain YZy121 (Supplementary Table 1) to eliminate mitochondrial α-KIV synthesis and ensure the biosensor signal and isobutanol production are derived only from cytosolic activity (Fig. 5a). We

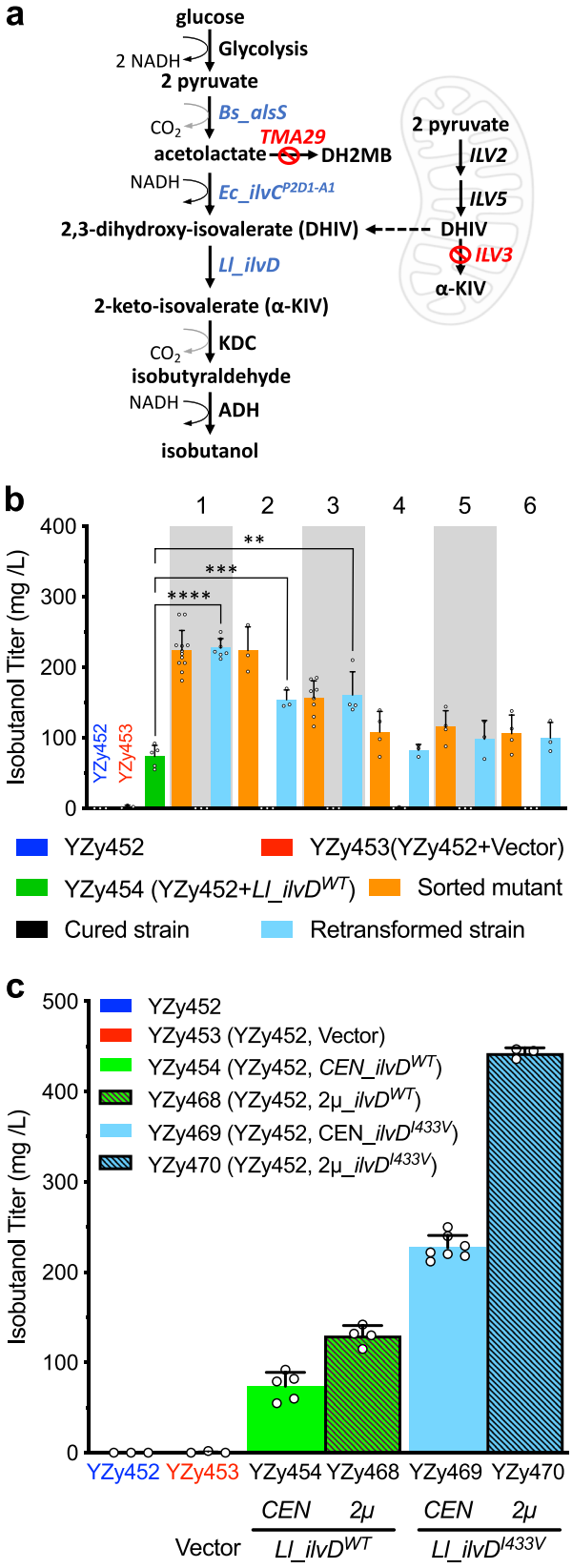

Fig. 5 Biosensor-assisted cytosolic isobutanol pathway engineering. **a** Schematic of the engineered cytosolic isobutanol pathway. *Bs_alsS*: acetolactate synthase (ALS) from *Bacillus subtilis*; *Ec_ilvC*$^{P2D1\text{-}A1}$: NADH-dependent ketol-acid reductoisomerase (KARI) variant from *E. coli*; *Ll_ilvD*: dihydroxyacid dehydratase (DHAD) from *Lactococcus lactis*; DH2MB: 2,3-dihydroxy-2-methyl butanoate. Mitochondrion image created with BioRender. **b** Isobutanol titers after 48 h fermentations in 15% glucose of sorted strains with unique *Ll_ilvD* sequences (orange), plasmid-cured derivatives (black), and strains obtained from retransforming YZy452 with each unique plasmid isolated from the corresponding sorted strain (cyan). The numbers on the upper *x*-axis identify each of the strains harboring screened mutants with unique *Ll_ilvD* sequences. Titers from YZy452 (containing the cytosolic isobutanol pathway with extra copies of *Ec_ilvC*$^{P2D1\text{-}A1}$) with (red) or without (blue) an empty vector, or transformed with a plasmid containing wild-type *Ll_ilvD* (green) are shown as controls. A two-sided *t*-test was used to determine the statistical significance of the difference between isobutanol titers achieved by YZy452 transformed with a plasmid containing *Ll_ilvD*^{WT} (green), or *Ll_ilvD* mutant #1 (*Ll_ilvD*^{I433V}), or mutant #2 (*Ll_ilvD*$^{V12A,\ S189P,\ H439R}$), or mutant #3 (*Ll_ilvD*^{K535R}). From left to right: $P < 0.0001$, $P = 0.0003$, $P = 0.0011$; $^{**}P \le 0.01$, $^{***}P \le 0.001$, $^{****}P \le 0.0001$. **c** Isobutanol titers of the basal stain YZy452 (blue) transformed with an empty vector (red), *Ll_ilvD*^{WT} (green), or *Ll_ilvD*^{I433V} (cyan), using CEN (solid) or 2μ (striped) plasmids. Isobutanol production was measured after 48 h fermentations in 15% glucose. All data are shown as mean values. Open circles represent individual data points. Error bars represent the standard deviation of at least three biological replicates. Source data are provided as a Source Data file.

also deleted *TMA29*, encoding an enzyme with acetolactate reductase activity that competes with KARI, producing the by-product 2,3-dihydroxy-2-methyl butanoate (DH2MB)[42]. We then integrated in the resulting strain (YZy443) a single copy of *Bs_alsS*, encoding an ALS from *Bacillus subtilis*[43], *Ec_ilvC*$^{P2D1\text{-}A1}$, encoding an engineered NADH-dependent KARI from *E. coli*[44], and *Ll_ilvD*, encoding a DHAD from *Lactococcus lactis* (Fig. 5a). Because *Ll*_IlvD requires iron-sulfur (Fe/S) cluster cofactors, we also overexpressed *AFT1*, a transcription factor involved in iron utilization and homeostasis[45]. The resulting strain (YZy449) contained a metabolic pathway to convert pyruvate to α-KIV in the cytosol, which can then be converted to isobutanol by endogenous cytosolic KDCs and ADHs (Fig. 5a).

We applied the isobutanol biosensor to find strains with increased expression of *Ec_ilvC*$^{P2D1\text{-}A1}$ that enhance cytosolic isobutanol production. Given that the catalytic rate constant (k_{cat}) of *Bs*_AlsS is about 28 times higher than that of *Ec_ilvC*$^{P2D1\text{-}A1}$ (Supplementary Table 7), we hypothesized that overexpressing additional copies of *Ec_ilvC*$^{P2D1\text{-}A1}$ would compensate for this difference and improve isobutanol production. Thus, we randomly integrated a cassette containing two copies of *Ec_ilvC*$^{P2D1\text{-}A1}$ (pYZ206) into YARCdelta5 δ-sites of YZy449 (Supplementary Tables 1, 2), and sorted for transformants with the highest fluorescence intensity. After three rounds of FACS, 20 randomly picked colonies produce an average of 296 ± 19 mg/L isobutanol from 15% galactose, with the highest producing strain (YZy452) achieving 310 ± 15 mg/L isobutanol (Supplementary Fig. 12). In contrast, 20 randomly picked colonies from the unsorted population produce on average only 188 ± 19 mg/L (Supplementary Fig. 12). These results demonstrate that the isobutanol-configured biosensor can identify strains with increased cytosolic isobutanol production.

We next explored if the isobutanol-configured biosensor could help identify *Ll_ilvD* variants that further enhance isobutanol production. Beginning with the highest producing strain isolated as described above (YZy452), we introduced an error-prone PCR library of *Ll_ilvD* mutants in CEN plasmids. Because the wild-type copy of *Ll_ilvD* in YZy452 is expressed from a P_{GAL10} promoter, growing the library in glucose ensures this wild-type copy is repressed, and only the *Ll_ilvD* variants from the CEN plasmid library (inserted downstream of a P_{TDH3} promoter) are expressed. After three rounds of FACS, all 24 randomly picked

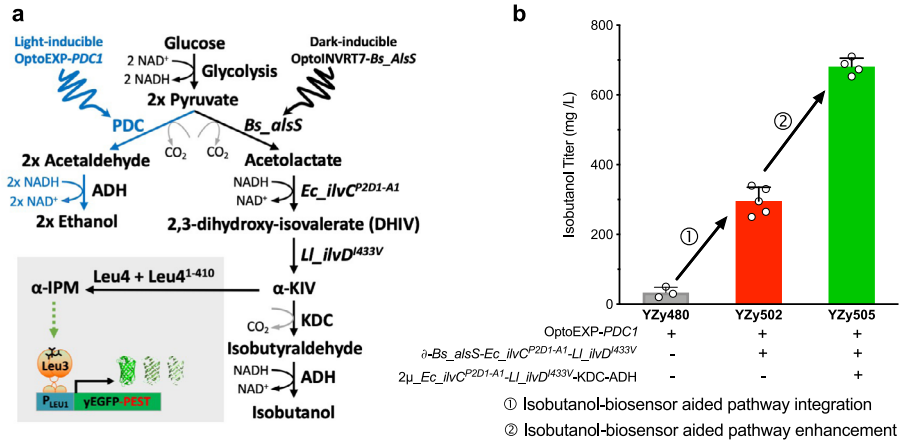

Fig. 6 Biosensor-assisted engineering of optogenetically controlled strains for cytosolic isobutanol production. a Schematic of the dark-inducible cytosolic isobutanol pathway (with *Bs_alsS* controlled by *OptoINVRT7*) and light-inducible *PDC1* (controlled by *OptoEXP*) in a triple *pdcΔ* strain containing the isobutanol configuration of the biosensor. **b** Isobutanol production of optogenetically regulated strains, including a basal strain containing only light-inducible *PDC1* (YZy480, gray); a strain also containing the dark-inducible upstream cytosolic pathway (*Bs_alsS, Ec_ilvC*$^{P2D1\text{-}A1}$, and *Ll_ilvD*^{I433V}) integrated in δ-sites (YZy502, red); and a strain containing additional enzymes from the cytosolic isobutanol pathway (*Ec_ilvC*$^{P2D1\text{-}A1}$, *Ll_ilvD*^{I433V}, KDC, and ADH) introduced in a 2μ plasmid (YZy505, green). Isobutanol production was measured after 48 h fermentations in media containing 2% glucose. Strains YZy502 and YZy505 where each isolated after two rounds of FACS. All data are shown as mean values. Open circles represent individual data points. Error bars represent the standard deviation of at least three biological replicates. Source data are provided as a Source Data file.

colonies produce between 150 mg/L and 260 mg/L isobutanol from 15% glucose, which is 2- to 3.5-times higher than a strain (YZy454) containing a plasmid with the wild-type *Ll_ilvD* (Supplementary Fig. 13a). Among the 24 random colonies examined, we found six unique *Ll_ilvD* sequences, most of them containing the sequence of mutant #1 (I433V, Supplementary Table 8). As described above for Ilv6p and Leu4p variants, fluorescence intensity measurements (Supplementary Fig. 13b) and isobutanol production (Fig. 5b) of sorted, cured, and retransformed strains were compared. Four of the six retransformed strains reproduce the isobutanol titers of the sorted strains, confirming the *Ll_ilvD* variants they contain cause the enhanced phenotypes and suggesting that background mutations in the two remaining sorted strains are responsible for them. The strain retransformed with the most active variant *Ll_ilvD*^{I433V} (YZy469) produces 227 ± 13 mg/L of isobutanol from 15% glucose, which is 3.1-fold higher than the strain harboring the wild-type *Ll_ilvD* (YZy454, Fig. 5c). When *Ll_ilvD*^{I433V} is overexpressed using a 2μ plasmid (YZy470), the titer further increases to 443 mg/L ± 6 mg/L, which is 3.4-fold higher than overexpressing the wild-type *Ll_ilvD* in a 2 μ plasmid (YZy468, Fig. 5c).

To gain structural insights on possible mechanisms by which *Ll_ilvD* activity is enhanced, we mapped the mutations in the most active variants onto the crystal structure of an IlvD homolog (Supplementary Fig. 14). *Ll*_IlvD mutants #1 and #3 each have a single mutation, I433V and K535R, respectively; however, mutant #2 has three residue substitutions (V12A, S189P, and H439R), which makes it more difficult to ascertain the importance and contribution of each mutation in this variant. Interestingly, all five mutations in the three variants are solvent exposed (Supplementary Fig. 14a, b), suggesting that some of them may improve the solubility, expression, or stability of the enzyme. In addition, mutations I433V and S189P, are located on opposing lobes that define the putative substrate entrance to the active site (Supplementary Fig. 14c, d), suggesting these mutations may enhance enzymatic activity by affecting the dynamics of opening and closing of the active site (Supplementary Note 6). In summary, our biosensor is capable of identifying previously unknown enzyme mutations that not only enhance isobutanol production, but may also improve our understanding of the molecular mechanisms that limit enzyme activity.

Finally, we set out to show that our biosensor could work in conjunction with optogenetic actuators to select for strains with enhanced flux through cytosolic isobutanol synthesis. We previously showed that optogenetically controlling the expression of the pyruvate decarboxylase (*PDC1*) and the mitochondrial isobutanol pathway in a triple *PDC* deletion background (*pdc1Δ pdc5Δ pdc6Δ*) boosts isobutanol production[46]. This is an effective way to increase metabolic flux towards pathways of interest that compete with *PDC1* without completely eliminating pyruvate decarboxylase activity, which causes a severe growth defect in glucose[47,48]. We tested our biosensor in a strain in which *PDC1* is controlled by *OptoEXP*[46], an optogenetic circuit that induces expression only in blue light (450 nm), and the first enzyme of the cytosolic pathway (*Bs*_AlsS) is controlled by *OptoINVRT7*[49], an optogenetic circuit that represses gene expression in blue light and activates it in the dark (Fig. 6a). The starting strain for this experiment (YZy502) has a triple *PDC* deletion background with a light-inducible *PDC1*, a dark-inducible cytosolic isobutanol pathway, and our biosensor in its isobutanol configuration (Supplementary Table 1). We transformed YZy502 with a 2μ plasmid (pYZ350, Supplementary Table 2) containing two copies of *Ec_ilvC*$^{P2D1\text{-}A1}$ and one copy each of *Ll_IlvD*^{I433V}, *ARO10* (KDC), and *Ll_adhA*^{RE1}(ADH)[50]. Using the biosensor in combination with optogenetic controls, we performed two rounds of FACS on a library of pooled transformants to isolate YZy505, which produces 681 mg/L ± 29 mg/L isobutanol in dark fermentations from 2% glucose, 20-times higher the starting strain (YZy480, Fig. 6b). Thus, our biosensor can assist in the construction of mitochondrial or cytosolic BCHA pathways, and is effective at identifying high-producing strains, including optogenetically controlled strains for enhanced flux towards isobutanol production.

Discussion

Genetically encoded biosensors have been developed to monitor microbial biosynthesis of several products of interest[51–60].

However, to our knowledge, biosensors for specific BCAAs and BCAA-derived products have not been reported in *S. cerevisiae*, which could enable high-throughput screens to develop strains for their production. Here we show that the endogenous Leu3p regulator of BCAA metabolism can be harnessed to develop genetically encoded biosensors for BCAA-derived product biosynthesis, such as the BCHAs isobutanol and isopentanol. Each application we describe demonstrates the use of the biosensor in either the isobutanol or isopentanol configuration for a specific purpose: to isolate high-producing strains from libraries of combinatorially assembled mitochondrial pathways (Fig. 2); to identify hyperactive enzymes for mitochondrial production of isobutanol (Fig. 3); or production of isopentanol across both mitochondria and cytosol (Fig. 4); to aid in the construction of a cytosolic isobutanol pathway (Fig. 5); and to use it in combination with optogenetic actuators, which opens future potential applications in dynamic control of metabolism (Fig. 6).

The fact that the biosensor acts by monitoring the intracellular concentrations of α-IPM[21,22] offers several advantages. Because α-IPM is a by-product of isobutanol and a precursor of isopentanol, the biosensor can be designed in two different configurations that indicate relative production of each BCHA specifically (Fig. 1 and Supplementary Fig. 4). The high selectivity stemming from the Leu3p mechanism of activation also makes each biosensor configuration unlikely to cross-react with other products, in contrast to previously reported alcohol biosensors in *E. coli*[61,62] and *S. cerevisiae*[63]. Furthermore, by monitoring the concentration of an intracellular metabolite (α-IPM), as opposed to the concentration of a secreted end product that easily traverses cell membranes bi-directionally, Leu3p-dependent biosensors facilitate the detection of BCAA-derived product biosynthesis in each individual cell (using flow cytometry), rather than the average production in a fermentation.

To improve isobutanol or isopentanol production in yeast, biosynthetic pathways have been engineered in mitochondria[29,37], cytosol[38,39], or simultaneously in both compartments[37,39,41,64], which makes the versatility of the biosensor to detect BCHA production in both compartments particularly valuable. For the mitochondrial isobutanol pathway, the isobutanol configuration of the biosensor allowed us to find strains from combinatorial libraries that produce, on average, more than twice as much isobutanol as strains randomly selected without assistance of a biosensor (Fig. 2), as well as strains with enhanced ALS activity (Ilv2p/Ilv6p, Fig. 3). For the cytosolic pathway, the same biosensor configuration helped us open two key bottlenecks at the KARI (*Ec_ilvC*$^{P2D1\text{-}A1}$, Supplementary Fig. 12), and DHAD (*Ll_Ilv-D*^{I433V}, Fig. 5c) metabolic steps. To our knowledge, no DHAD mutant to enhance isobutanol production has been previously reported. Additionally, the isopentanol configuration of the biosensor allowed us to identify strains with enhanced (α-IPM) synthase activity (Leu4p, Fig. 4), which is present in both mitochondria and cytosol. Altogether, high-throughput screens enabled by the biosensor in both configurations, allowed us to improve both mitochondrial and cytosolic isobutanol production by as much as 15- and 9-fold, respectively, as well as isopentanol production by approximately 20-fold (relative to wild-type strains).

In all our demonstrations, strains with higher fluorescence isolated after three rounds of sorting always have increased BCHA production, suggesting our biosensor has a very low rate of false positives. Beyond our initial characterizations (Fig. 1b, d), analyzing the strains randomly picked from subsequent sorting experiments confirmed the strong linear correlation ($R^2 = 0.95$, 0.96, 0.95) between fluorescence readout and BCHA production in actual screens (Supplementary Fig. 15), identifying virtually no false positives. This high efficiency is likely due to the fact that the source of diversity in all our applications is upstream of the α-IPM intermediate, for which the biosensor was designed. While most of the biosynthetic pathway and previously identified bottlenecks lay upstream of α-IPM, if the downstream pathway became limiting, the rate of false positives for isobutanol production could increase. Similarly, we do not expect the same high-throughput screens used in this study to be effective at identifying enhanced enzymes downstream of α-IPM. However, sorting strains with decreased fluorescence, reflecting increased rates of α-IPM processing, might be helpful in these scenarios. Furthermore, screening for random mutations in the genome could also lead to higher rates of false positives. Future research will determine how the biosensor operates in these specific settings.

This biosensor is applicable to several lines of research in biotechnology, basic science, and metabolic control. Their most immediate application will likely be to accelerate the development of strains for the production of isobutanol and isopentanol as promising advanced biofuels. However, because the biosensor is controlled by the activity of the BCAA regulator Leu3p, rather than directly sensing isobutanol or isopentanol concentrations, it may also be useful to develop strains for the production of valine, leucine, or other products derived from their metabolism[1–8]. An advantage of biosensors based on transcription factors is that they can be used to control the expression of any gene of interest. Therefore, Leu3p can be used to control the expression of not only reporter genes to develop high-throughput screens for strains with enhanced production (as demonstrated in this study), but also of essential or antibiotic resistance genes to develop high-throughput selection assays[54,62,65,66], or of key metabolic genes to develop autoregulatory mechanisms for dynamic control of product biosynthesis[18,67]. In contrast, the BCAA biosensor previously reported in mammalian cells[68,69] is based on fluorescence resonance energy transfer (FRET) and only measures the collective intracellular levels of valine, leucine, and isoleucine, which limits its applications.

Additionally, because BCAA biosynthesis initiates in mitochondria, our biosensor is potentially useful to study fundamental questions, not only in BCAA metabolism, but also in mitochondrial biology. While previously reported biosensors based on GFP-ligand-binding-protein chimeras, FRET, or its bioluminescence equivalent (BRET) have been developed to probe the mitochondrial metabolic state[70], our biosensor is capable of probing the metabolic activity of a mitochondrial biosynthetic pathway. Finally, the fact that the biosensor is functional in strains carrying optogenetic controls (Fig. 6) raises the intriguing possibility of simultaneously monitoring and controlling production of BCAAs and BCAA-derived products, which may open new research avenues in closed loop metabolic control and cybergenetics for metabolic engineering[71].

Methods

General molecular biology techniques. Genomic DNA extractions were carried out using the standard phenol chloroform procedure[72]. Genotyping PCRs were performed using GoTaq Green Master Mix (Promega, Madison, WI, USA). The oligonucleotides used in this study (Supplementary Table 9) were obtained from Integrated DNA Technologies (IDT, Coralville, IA, USA). *Escherichia coli* DH5α was used for routine transformations. All of the constructed plasmids were verified by DNA sequencing (GENEWIZ, South Plainfield, NJ, USA).

Growth media. Unless otherwise specified, yeast cells were grown at 30 °C on either YPD medium (10 g/L yeast extract, 20 g/L peptone, 0.15 g/L tryptophan and 20 g/L glucose) or synthetic complete (SC) drop out medium (20 g/L glucose, 1.5 g/L yeast nitrogen base without amino acids or ammonium sulfate, 5 g/L ammonium sulfate, 36 mg/L inositol, and 2 g/L amino acid drop out mixture) supplemented with 2% glucose, or non-fermentable carbon sources such as 2% galactose, or the mixture of 3% glycerol and 2.5% ethanol. 2% Bacto™-agar (BD, Franklin Lakes, NJ, USA) was added to make agar plates.

Assembly of DNA constructs. DNA construction was performed using standard restriction-enzyme digestion and ligation cloning and isothermal assembly (Gibson Assembly)[73]. Endogenous *S. cerevisiae* genes (*ILV6*, *LEU4*, and *AFT1*) were amplified from genomic DNA of CEN.PK2-1C by PCR using a forward primer containing an NheI restriction recognition site and a reverse primer containing an XhoI restriction recognition site (Supplementary Table 9). This enabled subcloning of PCR-amplified genes into pJLA vectors[29] and pJLA vector-compatible plasmids. Genes from other organisms, including *Bs_alsS*, *Ec_ilvC*$^{P2D1\text{-}A1}$ and *Ll_ilvD* were codon optimized for *S. cerevisiae* and synthesized by Bio Basic Inc. (Amherst, NY, USA). These genes were designed with flanking NheI and XhoI sites at the 5′ and 3′ ends, respectively. All plasmids constructed or used in this study are listed in Supplementary Table 2.

Constructing the isobutanol configuration of the biosensor. The reporter for the biosensor in its isobutanol configuration was constructed by placing the *S. cerevisiae LEU1* promoter (P_{LEU1}), in front of the yeast-enhanced green fluorescent protein (yEGFP) fused to a PEST tag. The *LEU1* promoter and yEGFP-PEST fragments amplified via PCR were inserted by Gibson assembly into the vector JLAb131 to make an intermediate plasmid (pYZ13) containing the fragment P_{LEU1}-yEGFP_PEST-T_{ADH1}, which was then subcloned into a *HIS3* locus integration (His3INT) vector pYZ12B[46], yielding the intermediate plasmid pYZ14. The truncated *LEU4*$^{1-410}$ was amplified from genomic DNA of CEN.PK2-1C and subcloned into plasmid JLAb23, which contains the constitutive promoter P_{TPI1} and terminator T_{PGK1}. The P_{TPI1}-*LEU4*$^{1-410}$-T_{PGK1} cassette from the resulting plasmid pYZ2 was then subcloned into pYZ14 using sequential gene insertion cloning[29] to form the plasmid pYZ16 (Supplementary Table 2).

Constructing the isopentanol configuration of the biosensor. To construct the biosensor in its isopentanol configuration, we removed the PEST-tag of the yEGFP reporter in plasmid pYZ14 by annealed oligo cloning. The two single-stranded overlapping oligonucleotides (Yfz_Oli59 and Yfz_Oli60) were annealed and cloned directly into the overhangs generated by restriction digest of pYZ14 at SalI and BsrGI sites. The resulting plasmid (pYZ24) contains cassette P_{LEU1}-yEGFP-T_{ADH1}. Next, we added a catalytically active and leucine-insensitive *LEU4* mutant (*LEU4*$^{\Delta S547}$, a deletion in Ser547)[28,37] to pYZ24 to form the isopentanol configuration of the biosensor, pYZ25. The deletion in Ser547 was achieved by site-directed mutagenesis using a plasmid containing wild-type *LEU4* (*LEU4*^{WT}). *LEU4*$^{\Delta S547}$ was then subcloned into JLAb23 to form plasmid pYZ1. The P_{TPI1}-*LEU4*$^{\Delta S547}$-T_{PGK1} cassette from pYZ1 was then subcloned into pYZ24 to form the plasmid pYZ25.

Constructing template plasmids for error-prone PCR. Plasmid pYZ125, used to prepare the random mutagenesis libraries, was constructed by subcloning the region of JLAb131 spanning from the *TDH3* promoter (P_{TDH3}) to the *ADH1* terminator (T_{ADH1}) into the CEN plasmid pRS416 to generate pYZ125[74]. *ILV6*, *LEU4*, and *Ll_ilvD* were subcloned into pYZ125, after linearization with NheI and XhoI, to create pYZ127, pYZ149, and pYZ126, respectively. The *ILV6*$^{V90D/L91F}$ mutant was generated using QuikChange site-directed mutagenesis and subcloned into pYZ125 to create pYZ148[35]. Leucine inhibition insensitive *LEU4* mutants *LEU4*$^{\Delta S547}$ and *LEU4*$^{1-410}$ were subcloned into pYZ125 to form pYZ154 and pYZ155, respectively (Supplementary Table 2).

Constructing δ-integration cassettes. We used a previously developed δ-integration (δ-INT) vector, pYZ23[46], to integrate multiple copies of gene cassettes into genomic YARCdelta5 δ-sites, the 337 bp long-terminal-repeat of *S. cerevisiae* Ty1 retrotransposons (YARCTy1-1, SGD ID: S000006792). The selection marker in pYZ23 is the shBleMX6 gene, which encodes a protein conferring resistance to zeocin and allows selection of different numbers of integration events by varying zeocin concentrations[75]. Resistance to higher concentrations of zeocin correlates with a higher number of gene cassettes integrated into δ-sites. To construct δ-integration plasmids pYZ33, pYZ113, and pYZ34, we used restriction site pairs XmaI/AscI (to extract gene cassettes) and MreI/AscI (to open pYZ23)[29,76]. Plasmid pYZ417 was constructed by sequentially inserting cassettes P_{TDH3}- *Ec_ilvC*$^{P2D1\text{-}A1}$-T_{CYC1} (from pYZ196), P_{TEF1}-*Ll_ilvD*^{I433V}-T_{TPS1} (from pYZ383), and $P_{Gal1\text{-}S}$-*Bs_alsS*-T_{ACT1} (from pYZ384) into the δ-integration plasmid EZ-L235[46], which contains the OptoEXP-*PDC1* cassette (P_{C120}-*PDC1*-T_{ACT1}). All of the δ-integration plasmids were linearized with PmeI prior to yeast transformation.

Error-prone PCR and random mutagenesis library construction. The random mutagenesis libraries of *ILV6*, *LEU4* and *Ll_ilvD* were generated by error-prone PCR using the GeneMorph II Random Mutagenesis Kit (Agilent Technologies, Santa Clara, CA, USA). The CEN plasmids harboring wild-type *ILV6* (pYZ127), *LEU4* (pYZ149), *Ll_ilvD* (pYZ126) or the *ILV6*$^{V90D/L91F}$ mutant (pYZ148) were used as templates for error-prone PCR. Various amounts of DNA template were used in the amplification reactions to obtain low (0–4.5 mutations/kb), medium (4.5–9 mutations/kb), and high (9–16 mutations/kb) mutation frequencies as described in the product manual. Primers Yfz_Oli198 and Yfz_Oli242, which contain NheI and XhoI restriction sites at their 5′ ends, respectively, were used to amplify and introduce random mutations into the region between the start codon and stop codon of each gene. The PCR fragments were incubated with DpnI for 2 h at 37 °C to degrade the template plasmids before purification with a the QIAquick PCR purification kit (Qiagen). The purified PCR fragments were digested overnight at 37 °C using NheI and XhoI, and ligated overnight at 16 °C with pYZ125. The same process was used to create an ep_library of the leucine regulatory domain of Leu4p, except the forward primer contained a BglII restriction site at its 5′ end, rather than an NheI site. The plasmid libraries that resulted were transformed into ultra-competent *E. coli* DH5α and plated onto LB-agar plates (five 150 mm petri dishes per library) containing 100 μg/ml of ampicillin. After incubating the plates overnight at 37 °C, the resulting lawns (with a library size of ~10^9) were scraped off the agar plates and the plasmid libraries were extracted using a QIAprep Spin Miniprep Kit (QIAGEN). The plasmid libraries were subsequently used for yeast transformation. Based on yeast transformation efficiency with these plasmid libraries, and the number of transformants collected for FACS, we estimate the size of our pre-sorted libraries to be ~10^6–10^7 variants.

Yeast strains and yeast transformations. *S. cerevisiae* strain CEN.PK2-1C (*MAT**a** ura3–52 trp1-289 leu2-3,112 his3-1 MAL2-8c SUC2*) and its derivatives were used in this study (Supplementary Table 1). Deletions of *BAT1*, *BAT2*, *ILV6*, *LEU4*, *LEU9*, *ILV3, TMA29, PDC1*, *PDC5*, *PDC6*, and *GAL80* were obtained using PCR-based homologous recombination. DNA fragments containing lox71- and lox66-flanked antibiotic resistance cassettes were amplified with PCR from plasmids containing an antibiotic resistance gene, using primers with 50–70 base pairs of homology to regions upstream and downstream of the ORF targeted for deletion[30]. Transformation of the gel-purified PCR fragments was performed using the lithium acetate method[77]. Cells transformed using antibiotic resistance markers, were first plated onto nonselective YPD plates for overnight growth, then replica plated onto YPD plates containing 300 μg/mL hygromycin (Invitrogen, Carlsbad, CA), 200 μg/mL nourseothricin (WERNER BioAgents, Jena, Germany), or 200 μg/mL Geneticin (G-418 sulfate, Gibco, Life Technologies, Grand Island, NY, USA). Chromosomal integrations and plasmid transformations were also performed using the lithium acetate method[77]. Cells transformed for δ-integration were first incubated in YPD liquid medium for six hours and then plated onto nonselective YPD agar plates for overnight growth. The next day, cells were replica plated onto YPD agar plates containing 300 μg/mL (for FACS) or higher concentrations (500, 800, 1200, and 1500 μg/mL for titrating higher copy numbers of integrations) of Zeocin (Invitrogen, Carlsbad, CA), and incubated at 30 °C until colonies appeared. Cells transformed with plasmid libraries or 2μ plasmids (used for FACS) were plated on three 150 mm petri plates per library. The resulting lawns (containing ~6.5×10^4 individual transformants in each plate, for a total of ~2×10^5 transformants) were scraped off the agar plates, small aliquots of the collected cells were then grown to exponential phase in fresh medium, and used for flow cytometry and FACS (see below). All strains with gene deletions or chromosomal integrations (expect δ-integrations) were genotyped with positive and negative controls to confirm the removal of the ORF of interest or the presence of integrated DNA cassette.

Strains with cytosolic isobutanol pathway. We first constructed a baseline strain for cytosolic isobutanol production (YZy449). We used constitutive promoters to express *Bs_alsS*, *Ec_ilvC*$^{P2D1\text{-}A1}$, and *AFT1*, and the galactose-inducible and glucose-repressible promoter P_{GAL10} to express *Ll_ilvD*. This approach allows us to use the same strain to screen for *Ec_ilvC*$^{P2D1\text{-}A1}$ and *Ll_ilvD* mutants using different carbon sources (galactose and glucose, respectively). We first deleted *ILV3* and *TMA29* in strain YZy121, which contains the isobutanol-configured biosensor, resulting in strain YZy443. We then transformed strain YZy443 with the *URA3* integration cassette from plasmid pYZ196 (loxP-*URA3*-loxP-P_{TDH3}-*AFT1*-T_{ADH1}-[P_{TEF1}-*Bs_alsS*-T_{ACT1}-P_{TDH3}-*Ec_ilvC*$^{P2D1\text{-}A1}$-T_{ADH1}]-P_{GAL10}-*Ll_ilvD*-T_{ACT1}), resulting in strain YZy447. Next, we recycled the *URA3* marker using the Cre-loxP site-specific recombination system[78] and counter selected on YPD plates with 1 mg/mL of 5-FOA (see below), resulting in the final strain YZy449. Both YZy447 and YZy449 make ~170 mg/L of isobutanol in fermentations using galactose as carbon source but are unable to make isobutanol from glucose (Supplementary Fig. 16).

Applying the biosensor in optogenetically controlled strains. To combine the biosensor (in its isobutanol configuration) with optogenetic controls of the cytosolic isobutanol pathway, we integrated OptoINVRT7[49] (using EZ-L439) into the *HIS3* locus of YZy90, a *gal80Δ*, triple *pdcΔ* (*pdc1Δ pdc5Δ pdc6Δ*) strain containing a constitutively expressed copy of *PDC1* in a 2μ plasmid, resulting in YZy480. We removed the 2μ-*PDC1* plasmid using 5-FOA (see below) to generate strain YZy481, which is able to grow in medium supplemented with glycerol and ethanol, but not in medium supplemented with glucose. We next introduced the biosensor in its isobutanol configuration into the *GAL80* locus of YZy481 to yield YZy487, and used GFP fluorescence intensity measurements and genotyping to confirm the biosensor was successfully integrated. A dark-inducible cytosolic isobutanol pathway and the light-inducible *PDC1* were then introduced to strain YZy487 via δ-integration. After two rounds of FACS, we analyzed the GFP fluorescence and isobutanol titers of ten colonies in dark fermentations with 2% glucose (see below). The colony with the highest GFP fluorescence intensity, corresponding to the highest isobutanol titer, was chosen as the host strain (YZy502) for further

enhancement of the cytosolic isobutanol production. To achieve a strain with even higher metabolic flux through the cytosolic isobutanol pathway, we introduced a 2μ plasmid pYZ350, containing partial cytosolic isobutanol pathway genes, and applied FACS to isolate high-producing transformants.

Flow cytometry/FACS. A BD LSRII Multi-Laser flow cytometer equipped with FACSDiva software V.8.0.2 (BD Biosciences, San Jose, CA) was used to quantify yEGFP fluorescence at an excitation wavelength of 488 nm and an emission wavelength of 510 nm (525/50 nm bandpass filter). Cells were gated on forward scatter (FSC) and side scatter (SSC) signals to discard debris and probable cell aggregates (Supplementary Fig. 17). The typical sample size was 50,000 events per measurement. A BD FACSAria Fusion flow cytometer with FACSDiva software was used for fluorescence activated cell sorting (FACS) with a 488 nm excitation wavelength and a bandpass filter of 530/30 for yEGFP detection. Cells exhibiting high levels of GFP fluorescence (top ~1%) were sorted. Sorted cells were collected into 1 mL of medium (see below), and 50 μL of each sample of collected sorted were streaked on a corresponding agar plate and incubated at 30 °C to obtain 24 random colonies. For each of the single colonies isolated, MFI and BCHA production were measured. The rest of the sorted cells (~950 μL) were incubated at 30 °C and at 200 rpm agitation to reach the stationary growth phase, followed by subculturing (1:100 dilution) in the same medium for the next round of sorting. FlowJo X software (BD Biosciences, San Jose, CA) was used to analyze the flow cytometry data.

Sample preparation for flow cytometry assays and FACS high-throughput screens. Fluorescence measurements and FACS were performed on samples in mid-exponential growth phase. Single colonies from agar plates or yeast transformation libraries diluted 1:100 were first cultured overnight until stationary phase in synthetic complete (SC), or synthetic complete minus uracil (SC-ura) medium, supplemented with 2% glucose or galactose (for screening the library of strains containing varying copies of *Ec_ilvC*$^{P2D1\text{-}A1}$). Overnight cultures were diluted 1:100 in the same fresh medium and grown to mid-exponential growth phase (12–13 h after inoculation). The growth media used for flow cytometry assays and FACS of *ILV6*-samples contain four times more valine (2.4 mM) than the synthetic defined medium described above. For strains with *PDC1* and *Bs_alsS* controlled by optogenetic circuits (*OptoEXP*[46] and *OptoINVRT7*[49], respectively), cultures were incubated for 8 h under constant blue light after inoculation with cells in stationary phase, followed by 10 h of incubation in the dark (see below) before flow cytometry or FACS. For all flow cytometry assays, cultures were diluted to an OD_{600} of approximately 0.1 with PBS. All samples used for FACS were diluted in fresh medium identical to their growth medium to OD_{600} of approximately 0.8.

Measurement of the response of the biosensor to α-IPM, α-KIV, and α-K3MV. Measurements of the responses of the biosensor to α-IPM, α-KIV and α-K3MV were carried out in a CEN.PK2-1C background strain, with the biosensor in its isobutanol configuration integrated at the *HIS3* locus (YZy121). A single colony from an agar plate was cultured overnight in SC medium supplemented with 2% glucose. The overnight culture was diluted 1:100 in fresh SC medium supplemented with 2% glucose, and 1 mL of the diluted culture was added to each well of a 24-well cell culture plate (Cat. 229524, CELLTREAT Scientific Products, Pepperell, MA, USA). Then, 10 μL of freshly made α-IPM (pH 7.0), α-KIV (pH 7.0), or α-K3MV (pH 7.0) solutions were added to each well to reach different final concentrations ranging from 0 μM to 75 μM. The 24-well plate was shaken for 12 h in an orbital shaker (Eppendorf, New Brunswick, USA) at 30 °C and at 200 rpm agitation. The GFP fluorescence of each sample in exponential phase (OD_{600} = 0.8–1.2) was measured using flow cytometry, with samples diluted in PBS in plates (50 μL of culture into 200 μL of buffer) for α-IPM and α-KIV, or in tubes (1 mL into 1 mL) for α-K3MV. The diluted samples were then kept on ice and until flow cytometry measurements were performed.

Yeast fermentations for isobutanol or isopentanol production. High-cell-density fermentations were carried out in sterile 24-well microtiter plates (Cat. 229524, CELLTREAT Scientific Products, Pepperell, MA, USA) in an orbital shaker (Eppendorf, New Brunswick, USA) at 30 °C and at 200 rpm agitation. Single colonies were grown overnight in 1 mL of synthetic complete (SC), or synthetic complete minus uracil (SC-ura) medium, supplemented with 2% glucose. The next day, 10 μL of the overnight culture were used to inoculate 1 mL of SC (or SC-ura) medium supplemented with 2% glucose in a new 24-well plate. After 20 h, the plates were centrifuged at 234 *g* for 5 min, the supernatant was discarded, and cells were resuspended in 1 mL of SC (or SC-ura) supplemented with 15% glucose (or galactose). The plates were covered with sterile adhesive SealPlate® films (Cat. # STR-SEAL-PLT; Excel Scientific, Victorville, CA) and incubated for 48 h at 30 °C with 200 rpm shaking. The SealPlate® films were used in all 24-well plate fermentations to maintain semi-aerobic conditions in each well, and to prevent evaporation and cross-contamination between wells. At the end of the fermentations, the OD_{600} of the culture in each well was measured in a TECAN infinite M200PRO plate reader (Tecan Group Ltd., Männedorf, Switzerland). Plates were then centrifuged for 5 min at 234 *g*, and the supernatant from each well was analyzed using HPLC as described below.

Fermentations of strains with optogenetic controls were also carried out in sterile 24-well microtiter plates, as described above, but with modifications as previously described[46] (see Supplementary Note 7). The parameter ρ, the cell density at which we switched cells from growing in blue light to dark and θ, the incubation time in the dark before fermentation used in the initial screening fermentations are an OD_{600} of 6 and 6 h, respectively, which were estimated based on the characterization and modeling of the optogenetic circuits OptoEXP[46] and INVRT7[49]. The optimal ρ (OD_{600} of 5) and θ (6 h) of the best isobutanol-producing strains (YZy502 and YZy505) were determined experimentally by measuring the isobutanol titers from fermentations using different ρ and θ values. To vary these parameters, a single colony of each strain was first grown to stationary phase in SC (for YZy502) or SC-ura (for YZy505) medium supplemented with 2% glucose under constant blue light at 30 °C. The overnight cultures were diluted to an OD_{600} of 0.1 in the same medium. We began incubations (at 30 °C and 200 rpm) of the diluted cultures at different times and under pulsed blue light to achieve cultures with different OD_{600} values, which correspond to variations in ρ, ranging from 1 to 9. After measuring the OD_{600} of each culture, we switched them from light to dark and incubated for 6 h at 30 °C and 200 rpm. After the dark incubation period, the cells were centrifuged and resuspended in 1 mL of the same medium supplemented with 2% glucose. The plates were covered with sterile adhesive SealPlate® films (Cat. # STR-SEAL-PLT; Excel Scientific, Victorville, CA) and incubated in the dark (wrapped in aluminum foil) for 48 h at 30 °C and 200 rpm. Subsequently, the cultures were prepared for HPLC analysis (see below). To determine the optimal θ, we diluted the overnight culture to an OD_{600} of 0.1 and incubated it at 30 °C and 200 rpm, and under pulsed blue light to reach an OD_{600} of 5, which was the optimal ρ determined in the previous experiment. Next, we incubated the cells in the dark (30 °C and 200 rpm) for different numbers of hours, ranging from 1 to 10, which correspond to variations in θ. After the dark incubation period, cells were centrifuged and resuspended in 1 mL of the same medium supplemented with 2% glucose, followed by 48 h of incubation in the dark (30 °C and 200 rpm) and HPLC analysis as described below.

Analysis of biosensor fluorescence, intracellular α-IPM, and BCHA production throughout low-cell density fermentations. Low and high-isobutanol (YZy121, YZy235) or isopentanol producers (SHy187, SHy159) were grown overnight in 1 mL of SC (or SC-ura) medium supplemented with 2% glucose in 24-well plates at 30 °C. 100 μL of overnight culture was used to inoculate 100 mL of SC (or SC-ura) medium supplemented with 15% glucose at 30 °C, and agitated at 200 rpm in an orbital shaker for a time course of 30 h. Timepoints were taken at 5 h, 12 h, and 30 h. For each time point, samples were collected for analysis of either cellular florescence, intracellular α-IPM, or extracellular BCHA concentration. Cellular florescence was measured via flow cytometry as described above. Intracellular α-IPM concentration was measured with Thermo Fisher Q Exactive HPLC-Orbitrap MS equipment. The protocol for metabolite extraction from cells was based on previously described methods[60] with minor modifications. At each time point, an extraction solution containing 40:40:20 (v/v/v) methanol:acetonitrile:ddH_2O with 0.5% formic acid stored at −20 °C, was used to extract metabolites from a volume of cells equivalent to 15 mL of culture at an OD_{600} of 1. Although volumes collected for each time point differ, equal cell masses were pelleted by centrifuging at 2107 *g* for 10 min at 4 °C. The cell pellet was vortexed with 1 mL of extraction solution and incubated for 1 min at room temperature. A total of 88 μL of 15.8% (w/v) NH_4HCO_3 was added immediately after, and mixed by vortex to neutralize the extraction solution. The resulting mixture was incubated at −20 °C for 15 min and centrifuged at 17,000 *g* for 8 min at 4 °C. A total of 150 μL of supernatant was dried via vacufuge for 2 h. The dried metabolites were resuspended in 50 μL of ddH_2O and analyzed using an Atlantis T3 3 μm 2.1 × 150 mm reversed-phase column (Waters, Part No. 186003719, Milford, MA, USA). Gas chromatography (GC/MS) was used to measure extracellular product concentration of isobutanol or isopentanol. A total of 800 μL of the fermentation broth was centrifuged at 17,000 *g* for 40 min at 4 °C to remove cells and residual debris. The supernatant was subjected to an alcohol extraction with hexane, in which hexane and supernatant were mixed at a 1:1 ratio, vortexed for 15 min, and then centrifuged at 17,000 *g* for 10 min at 4 °C. The organic phase was analyzed using a DB-WAX UI 0.5 μm gas chromatography column (Agilent, Part No. 122-7033UI, Santa Clara, CA, USA).

Digital droplet PCR to estimate library and sorted strain genotypes. The Digital Droplet PCR (ddPCR) experiment was performed on a Bio-Rad QX200 Droplet Digital PCR system with an Automated Droplet Generator using QX200 ddPCR Evagreen Supermix according to the manufacturer's instructions. Four PCR primers were used (Supplementary Table 9) to amplify a genomic single copy reference, *ILV2*, *ARO10*, and the Zeocin resistance cassette on genomic DNA templates from the pre-sorted library (PSL) as well as from the high-producers isolated from the second round of FACS in Fig. 2 (Y436-439, Y442 and Y443). The copy numbers of each amplification target were normalized to the counts of the single copy genome reference. As the upstream (A) and downstream pathway (B) share homology with the complete pathway (C), the following linear equations were solved to determine the number of integrations of each cassette, where X is the copy number of the zeocin resistance cassette, Y is the copy number of *ILV2*,

and Z is the copy number of *ARO10*:

$$A + B + C = X \quad (1)$$

$$A + C = Y \quad (2)$$

$$B + C + 1 = Z \quad (3)$$

As *ARO10* has a single integration in wild-type yeast, 1 copy is added to Eq. (3). The copies of unique strains are rounded to the nearest integer, while copies in PSL, are reported as the number of average integrations normalized per genome in the diverse library population.

Removal of plasmids from *Saccharomyces cerevisiae*. *URA3* plasmids in yeast strains were removed by 5-fluoroorotic acid (5-FOA) selection[79]. Cells were first grown in YPD overnight and then streaked on SC agar plates containing 1 mg/mL 5-FOA (Zymo Research, Orange, CA, USA). A single colony from an SC/5-FOA agar plate was streaked again on a new SC/5-FOA agar plate. To confirm that strains were cured of the *URA3*-containing plasmid, they were inoculated into SC-ura medium supplemented with 2% glucose; strains lacking the *URA3*-containing plasmid were not able to grow in SC-ura medium.

Yeast plasmid isolation. Plasmid isolation from yeast was performed according to a user-developed protocol from Michael Jones (protocol PR04, Isolation of plasmid DNA from yeast, QIAGEN) using a QIAprep Spin Miniprep kit (QIAGEN, Valencia, CA, USA)[80]. The isolated plasmids were retransformed into *E. coli* DH5α to produce plasmids at higher titer for subsequent sequencing and retransformation into the parental yeast strain.

Analysis of BCHA production. The concentrations of isobutanol, and isopentanol were determined with high-performance liquid chromatography (HPLC) using an Agilent 1260 Infinity instrument (Agilent Technologies, Santa Clara, CA, USA). Samples were centrifuged at 17,000 *g* for 40 min at 4 °C to remove residual cells and other solid debris, and analyzed using an Aminex HPX-87H ion-exchange column (Bio-Rad, Hercules, CA USA). The column was eluted with a mobile phase of 5 mM sulfuric acid at 55 °C and with a flow rate of 0.6 mL/min for 50 min. The chemical concentrations were monitored with a refractive index detector (RID) and quantified by comparing the peak areas to those of standards with known concentrations.

Statistical analysis. Two-sided Student's *t* tests were performed using GraphPad Prism (version 8.0 for Mac OS, GraphPad Software, San Diego, California USA, www.graphpad.com) to determine the statistical significance of differences observed in product titers between strains. Probabilities (*P*-values) less than (or equal to) 0.05 are considered sufficient to reject the null hypothesis (that the means of the two samples are the same) and accept the alternative hypothesis (that the means of the two samples are different).

Reporting summary. Further information on research design is available in the Nature Research Reporting Summary linked to this article.

Data availability

The authors declare that all data supporting the findings of this study are available within the paper (and its Supplementary Information files). The source data underlying Figs. 1–6, Supplementary Figs. S2–7, S9, S10, S12, S13, S15, S16, and Supplementary Table 3 are provided in the Source Data File.

Received: 17 June 2020; Accepted: 15 December 2021;
Published online: 12 January 2022

References

1. Yu, A. Q., Juwono, N. K. P., Foo, J. L., Leong, S. S. J. & Chang, M. W. Metabolic engineering of Saccharomyces cerevisiae for the overproduction of short branched-chain fatty acids. *Metab. Eng.* **34**, 36–43 (2016).
2. Stirrett, K., Denoya, C. & Westpheling, J. Branched-chain amino acid catabolism provides precursors for the Type II polyketide antibiotic, actinorhodin, via pathways that are nutrient dependent. *J. Ind. Microbiol Biot.* **36**, 129–137 (2009).
3. Surger, M. J., Angelov, A., Stier, P., Ubelacker, M. & Liebl, W. Impact of branched-chain amino acid catabolism on fatty acid and alkene biosynthesis in micrococcus luteus. *Front Microbiol* **9**, 374 (2018).
4. Jambunathan, P. & Zhang, K. Novel pathways and products from 2-keto acids. *Curr. Opin. Biotechnol.* **29**, 1–7 (2014).
5. Generoso, W. C., Schadeweg, V., Oreb, M. & Boles, E. Metabolic engineering of Saccharomyces cerevisiae for production of butanol isomers. *Curr. Opin. Biotechnol.* **33**, 1–7 (2015).
6. Choi, Y. J., Lee, J., Jang, Y. S. & Lee, S. Y. Metabolic engineering of microorganisms for the production of higher alcohols. *Mbio* **5**, e01524–01514 (2014).
7. Yuan, J., Mishra, P. & Ching, C. B. Metabolically engineered Saccharomyces cerevisiae for branched-chain ester productions. *J. Biotechnol.* **239**, 90–97 (2016).
8. Park, J. H. & Lee, S. Y. Fermentative production of branched chain amino acids: a focus on metabolic engineering. *Appl. Microbiol. Biotechnol.* **85**, 491–506 (2010).
9. Nevoigt, E. Progress in metabolic engineering of Saccharomyces cerevisiae. *Microbiol. Mol. Biol. Rev.* **72**, 379–412 (2008).
10. Rogers, J. K. & Church, G. M. Multiplexed engineering in biology. *Trends Biotechnol.* **34**, 198–206 (2016).
11. Schallmey, M., Frunzke, J., Eggeling, L. & Marienhagen, J. Looking for the pick of the bunch: high-throughput screening of producing microorganisms with biosensors. *Curr. Opin. Biotechnol.* **26**, 148–154 (2014).
12. Mahr, R. & Frunzke, J. Transcription factor-based biosensors in biotechnology: current state and future prospects. *Appl. Microbiol. Biot.* **100**, 79–90 (2016).
13. Lin, J. L., Wagner, J. M. & Alper, H. S. Enabling tools for high-throughput detection of metabolites: Metabolic engineering and directed evolution applications. *Biotechnol. Adv.* **35**, 950–970 (2017).
14. Eggeling, L., Bott, M. & Marienhagen, J. Novel screening methods—biosensors. *Curr. Opin. Biotechnol.* **35**, 30–36 (2015).
15. Chae, T. U., Choi, S. Y., Kim, J. W., Ko, Y. S. & Lee, S. Y. Recent advances in systems metabolic engineering tools and strategies. *Curr. Opin. Biotechnol.* **47**, 67–82 (2017).
16. Kohlhaw, G. B. Leucine biosynthesis in fungi: entering metabolism through the back door. *Microbiol. Mol. Biol. Rev.* **67**, 1–15 (2003).
17. Hutson, S. M., Sweatt, A. J. & LaNoue, K. F. Branched-chain amino acid metabolism: Implications for establishing safe intakes (vol 135, pg 1557S, 2005). *J. Nutr.* **135**, 2009–2009 (2005).
18. Zhang, F. Z., Carothers, J. M. & Keasling, J. D. Design of a dynamic sensor-regulator system for production of chemicals and fuels derived from fatty acids. *Nat. Biotechnol.* **30**, 354–U166 (2012).
19. Koch, M., Pandi, A., Borkowski, O., Batista, A. C. & Faulon, J. L. Custom-made transcriptional biosensors for metabolic engineering. *Curr. Opin. Biotechnol.* **59**, 78–84 (2019).
20. Sze, J. Y., Remboutsika, E. & Kohlhaw, G. B. Transcriptional regulator Leu3 of Saccharomyces cerevisiae: separation of activator and repressor functions. *Mol. Cell Biol.* **13**, 5702–5709 (1993).
21. Sze, J. Y., Woontner, M., Jaehning, J. A. & Kohlhaw, G. B. In vitro transcriptional activation by a metabolic intermediate: activation by Leu3 depends on alpha-isopropylmalate. *Science* **258**, 1143–1145 (1992).
22. Zhou, K. M., Bai, Y. L. & Kohlhaw, G. B. Yeast regulatory protein LEU3: a structure-function analysis. *Nucleic Acids Res.* **18**, 291–298 (1990).
23. Farrell, J., Holladay, J., Wagner, R. Fuel *Blendstocks with the Potential to Optimize Future Gasoline Engine Performance: Identification of Five Chemical Families for Detailed Evaluation* (U.S. Department of Energy, 2018).
24. U.S. Department of Energy Office of Energy Efficiency and Renewable Energy. *Co-Optimization of Fuels & Engines: Scientific Innovation for Efficient, Clean, and Affordable Transportation* (U.S. Department of Energy Office of Energy Efficiency and Renewable Energy, 2019).
25. Geleynse, S., Brandt, K., Garcia-Perez, M., Wolcott, M. & Zhang, X. The alcohol-to-jet conversion pathway for drop-in biofuels: techno-economic evaluation. *ChemSusChem* **11**, 3728–3741 (2018).
26. Hazelwood, L. A., Daran, J. M., van Maris, A. J. A., Pronk, J. T. & Dickinson, J. R. The ehrlich pathway for fusel alcohol production: a century of research on Saccharomyces cerevisiae metabolism. *Appl Environ. Microbiol.* **74**, 2259–2266 (2008).
27. Rogers, S., Wells, R. & Rechsteiner, M. Amino acid sequences common to rapidly degraded proteins: the PEST hypothesis. *Science* **234**, 364–368 (1986).
28. Cavalieri, D. et al. Trifluoroleucine resistance and regulation of alpha-isopropyl malate synthase in Saccharomyces cerevisiae. *Mol. Gen. Genet.* **261**, 152–160 (1999).
29. Avalos, J. L., Fink, G. R. & Stephanopoulos, G. Compartmentalization of metabolic pathways in yeast mitochondria improves the production of branched-chain alcohols. *Nat. Biotechnol.* **31**, 335–341 (2013).
30. Zhang, Y. et al. Xylose utilization stimulates mitochondrial production of isobutanol and 2-methyl-1-butanol in Saccharomyces cerevisiae. *Biotechnol. Biofuels* **12**, 223 (2019).
31. Cullin, C., Baudin-Baillieu, A., Guillemet, E. & Ozier-Kalogeropoulos, O. Functional analysis of YCL09C: evidence for a role as the regulatory subunit of acetolactate synthase. *Yeast* **12**, 1511–1518 (1996).

32. Pang, S. S. & Duggleby, R. G. Expression, purification, characterization, and reconstitution of the large and small subunits of yeast acetohydroxyacid synthase. *Biochemistry* **38**, 5222–5231 (1999).
33. Kopecky, J., Janata, J., Pospisil, S., Felsberg, J. & Spizek, J. Mutations in two distinct regions of acetolactate synthase regulatory subunit from Streptomyces cinnamonensis result in the lack of sensitivity to end-product inhibition. *Biochem. Biophys. Res. Commun.* **266**, 162–166 (1999).
34. Ofuonye, E., Kutin, K. & Stuart, D. T. Engineering Saccharomyces cerevisiae fermentative pathways for the production of isobutanol. *Biofuels* **4**, 185–201 (2013).
35. Hammer, S. K. & Avalos, J. L. Uncovering the role of branched-chain amino acid transaminases in Saccharomyces cerevisiae isobutanol biosynthesis. *Metab. Eng.* **44**, 302–312 (2017).
36. Zhang, Z. L. et al. Subdomain II of alpha-isopropylmalate synthase is essential for qctivity: inferring a mechanism of feedback inhibition. *J. Biol. Chem.* **289**, 27966–27978 (2014).
37. Hammer, S. K., Zhang, Y. & Avalos, J. L. Mitochondrial compartmentalization confers specificity to the 2-ketoacid recursive pathway: increasing isopentanol production in Saccharomyces cerevisiae. *ACS Synth. Biol.* **9**, 546–555 (2020).
38. Brat, D., Weber, C., Lorenzen, W., Bode, H. B. & Boles, E. Cytosolic re-localization and optimization of valine synthesis and catabolism enables increased isobutanol production with the yeast Saccharomyces cerevisiae. *Biotechnol. Biofuels* **5**, https://doi.org/10.1186/1754-6834-5-65 (2012).
39. Park, S. H. & Hahn, J. S. Development of an efficient cytosolic isobutanol production pathway in Saccharomyces cerevisiae by optimizing copy numbers and expression of the pathway genes based on the toxic effect of alpha-acetolactate. *Sci. Rep.* **9**, 3996 (2019).
40. Wess, J., Brinek, M. & Boles, E. Improving isobutanol production with the yeast Saccharomyces cerevisiae by successively blocking competing metabolic pathways as well as ethanol and glycerol formation. *Biotechnol. Biofuels* **12**, 173 (2019).
41. Matsuda, F. et al. Construction of an artificial pathway for isobutanol biosynthesis in the cytosol of Saccharomyces cerevisiae. *Biosci. Biotechnol. Biochem* **76**, 2139–2141 (2012).
42. Hawkins, A. et al. Reduced by-product accumulation for improved production of isobutanol. US20110236942A1 (2012).
43. Atsumi, S., Hanai, T. & Liao, J. C. Non-fermentative pathways for synthesis of branched-chain higher alcohols as biofuels. *Nature* **451**, 86–89 (2008).
44. Brinkmann-Chen, S. et al. General approach to reversing ketol-acid reductoisomerase cofactor dependence from NADPH to NADH. *Proc. Natl Acad. Sci. USA* **110**, 10946–10951 (2013).
45. Dundon, C. A., Aristidou, A., Hawkins, A., Lies, D. & Albert, L. Methods of increasing dihydroxy acid dehydratase activity to improve production of fuels, chemicals, and amino acids. US8273565B2 (2011).
46. Zhao, E. M. et al. Optogenetic regulation of engineered cellular metabolism for microbial chemical production. *Nature* **555**, 683–687 (2018).
47. Oud, B. et al. An internal deletion in MTH1 enables growth on glucose of pyruvate-decarboxylase negative, non-fermentative Saccharomyces cerevisiae. *Micro. Cell Fact.* **11**, 131 (2012).
48. van Maris, A. J. et al. Directed evolution of pyruvate decarboxylase-negative Saccharomyces cerevisiae, yielding a C2-independent, glucose-tolerant, and pyruvate-hyperproducing yeast. *Appl Environ. Microbiol* **70**, 159–166 (2004).
49. Zhao, E. M. et al. Design and characterization of rapid optogenetic circuits for dynamic control in yeast metabolic engineering. *ACS Synth. Biol.* **9**, 3254–3266 (2021).
50. Bastian, S. et al. Engineered ketol-acid reductoisomerase and alcohol dehydrogenase enable anaerobic 2-methylpropan-1-ol production at theoretical yield in Escherichia coli. *Metab. Eng.* **13**, 345–352 (2011).
51. Skjoedt, M. L. et al. Engineering prokaryotic transcriptional activators as metabolite biosensors in yeast. *Nat. Chem. Biol.* **12**, 951−+ (2016).
52. Liu, C., Zhang, B., Liu, Y. M., Yang, K. Q. & Liu, S. J. New intracellular shikimic acid biosensor for monitoring shikimate synthesis in corynebacterium glutamicum. *ACS Synth. Biol.* **7**, 591–601 (2018).
53. Li, H., Chen, W., Jin, R. N., Jin, J. M. & Tang, S. Y. Biosensor-aided high-throughput screening of hyper-producing cells for malonyl-CoA-derived products. *Microbial Cell Fact.* **16**, https://doi.org/10.1186/s12934-017-0794-6 (2017).
54. Leavitt, J. M. et al. Biosensor-enabled directed evolution to improve muconic acid production in Saccharomyces cerevisiae. *Biotechnol. J.* **12**, https://doi.org/10.1002/biot.201600687 (2017).
55. Liang, W. F. et al. Biosensor-assisted transcriptional regulator engineering for Methylobacterium extorquens AM1 to improve mevalonate synthesis by increasing the acetyl-CoA supply. *Metab. Eng.* **39**, 159–168 (2017).
56. Li, S. J., Si, T., Wang, M. & Zhao, H. M. Development of a synthetic Malonyl-CoA Sensor in Saccharomyces cerevisiae for intracellular metabolite monitoring and genetic screening. *Acs Synth. Biol.* **4**, 1308–1315 (2015).
57. DeLoache, W. C. et al. An enzyme-coupled biosensor enables (S)-reticuline production in yeast from glucose. *Nat. Chem. Biol.* **11**, 465−+ (2015).
58. Liu, Y. et al. Biosensor-based evolution and elucidation of a biosynthetic pathway in Escherichia coli. *ACS Synth. Biol.* **6**, 837–848 (2017).
59. Monteiro, F. et al. Measuring glycolytic flux in single yeast cells with an orthogonal synthetic biosensor. *Mol. Syst. Biol.* **15**, e9071 (2019).
60. Yuan, J., Bennett, B. D. & Rabinowitz, J. D. Kinetic flux profiling for quantitation of cellular metabolic fluxes. *Nat. Protoc.* **3**, 1328–1340 (2008).
61. Yu, H. et al. Establishment of BmoR-based biosensor to screen isobutanol overproducer. *Micro. Cell Fact.* **18**, 30 (2019).
62. Dietrich, J. A., Shis, D. L., Alikhani, A. & Keasling, J. D. Transcription factor-based screens and synthetic selections for microbial small-molecule biosynthesis. *ACS Synth. Biol.* **2**, 47–58 (2013).
63. Shi, S., Choi, Y. W., Zhao, H., Tan, M. H. & Ang, E. L. Discovery and engineering of a 1-butanol biosensor in Saccharomyces cerevisiae. *Bioresour. Technol.* **245**, 1343–1351 (2017).
64. Park, S. H., Kim, S. & Hahn, J. S. Metabolic engineering of Saccharomyces cerevisiae for the production of isobutanol and 3-methyl-1-butanol. *Appl. Microbiol. Biot.* **98**, 9139–9147 (2014).
65. D'Ambrosio, V. & Jensen, M. K. Lighting up yeast cell factories by transcription factor-based biosensors. *FEMS Yeast Res.* **17**, https://doi.org/10.1093/femsyr/fox076 (2017).
66. Snoek, T. et al. An orthogonal and pH-tunable sensor-selector for muconic acid biosynthesis in yeast. *ACS Synth. Biol.* **7**, 995–1003 (2018).
67. Lalwani, M. A., Zhao, E. M. & Avalos, J. L. Current and future modalities of dynamic control in metabolic engineering. *Curr. Opin. Biotechnol.* **52**, 56–65 (2018).
68. Yoshida, T., Nakajima, H., Takahashi, S., Kakizuka, A. & Imamura, H. OLIVe: a genetically encoded fluorescent biosensor for quantitative imaging of branched-chain amino acid levels inside single living cells. *ACS Sens.* **4**, 3333–3342 (2019).
69. Mustafi, N., Grunberger, A., Kohlheyer, D., Bott, M. & Frunzke, J. The development and application of a single-cell biosensor for the detection of l-methionine and branched-chain amino acids. *Metab. Eng.* **14**, 449–457 (2012).
70. Zhang, Y. & Avalos, J. L. Traditional and novel tools to probe the mitochondrial metabolism in health and disease. *Wiley Interdiscip. Rev. Syst. Biol. Med.* **9**, https://doi.org/10.1002/wsbm.1373 (2017).
71. Carrasco-Lopez, C., Garcia-Echauri, S. A., Kichuk, T. & Avalos, J. L. Optogenetics and biosensors set the stage for metabolic cybergenetics. *Curr. Opin. Biotechnol.* **65**, 296–309 (2020).
72. Sambrook, J. & Russell, D. W. Purification of nucleic acids by extraction with phenol:chloroform. *CSH Protoc* **2006**, https://doi.org/10.1101/pdb.prot4455 (2006).
73. Gibson, D. G. et al. Enzymatic assembly of DNA molecules up to several hundred kilobases. *Nat. Methods* **6**, 343–U341 (2009).
74. Sikorski, R. S. & Hieter, P. A system of shuttle vectors and yeast host strains designed for efficient manipulation of DNA in Saccharomyces cerevisiae. *Genetics* **122**, 19–27 (1989).
75. Zhao, E. M. et al. Light-based control of metabolic flux through assembly of synthetic organelles. *Nat. Chem. Biol.* **15**, 589–597 (2019).
76. Yuan, J. & Ching, C. B. Combinatorial assembly of large biochemical pathways into yeast chromosomes for improved production of value-added compounds. *ACS Synth. Biol.* **4**, 23–31 (2015).
77. Gietz, R. D. & Woods, R. A. Transformation of yeast by lithium acetate/single-stranded carrier DNA/polyethylene glycol method. *Methods Enzymol.* **350**, 87–96 (2002).
78. Gueldener, U., Heinisch, J., Koehler, G. J., Voss, D. & Hegemann, J. H. A second set of loxP marker cassettes for Cre-mediated multiple gene knockouts in budding yeast. *Nucleic Acids Res.* **30**, e23 (2002).
79. Boeke, J. D., Trueheart, J., Natsoulis, G. & Fink, G. R. 5-Fluoroorotic acid as a selective agent in yeast molecular-genetics. *Methods Enzymol.* **154**, 164–175 (1987).
80. Hong, S. B., Rashid, M. B. & Santiago-Vázquez, L. Z. *Methods in Biotechnology* (Wiley, 2016).

Acknowledgements

The authors thank Christina DeCoste and Katherine Rittenbach, who assisted with all flow cytometry instrumentation. We also thank Wenyun Lu and Joshua D. Rabinowitz, who generously provided equipment and assistance in measuring intracellular α-IPM metabolite concentrations. This work was supported by the U.S. Department of Energy, Office of Science, Office of Biological and Environmental Research, Genomic Science Program under award number DE-SC0019363, as well as by the National Science Foundation, and NSF CAREER Award CBET-1751840 (to J.L.A.). This work was also supported by the NSF Graduate Research Fellowship Program grant DGE-1656466, the P.E.O. Scholar Award, and the Harold W. Dodds Fellowship from Princeton University (to S.K.H.), as well as by the NIGMS of the National Institutes of Health under grant number T32GM007388 (to J.D.C.). The content of this article is solely the responsibility of the authors and does not necessarily represent the official views of the National Institutes of Health. J.L.A. is also supported by The Pew Charitable Trusts, The Camille Dreyfus Teacher-Scholar Award, The Eric and Wendy Schmidt Transformative Technology Fund, and grants from Princeton University and the Andlinger Center for Energy and the Environment.

Author contributions

Conceptualization and methodology: Y.Z., J.D.C., S.K.H., and J.L.A.; investigation: Y.Z., J.D.C., S.K.H., C.C.L., S.A.G.E., J.B.W., W.W., and J.L.A.; writing of original draft: Y.Z., S.K.H., and J.L.A.; review and editing: all authors; funding acquisition: J.L.A.; supervision: J.L.A.

Competing interests

J.L.A. and the Whitehead Instituted/MIT have submitted a patent application to the US patent office pertaining some elements of the biosensor design described in this study (US20160326535A1). The remaining authors declare no competing interests.

Additional information

Supplementary information The online version contains supplementary material available at https://doi.org/10.1038/s41467-021-27852-x.

Correspondence and requests for materials should be addressed to José L. Avalos.

Peer review information *Nature Communications* thanks the anonymous reviewer(s) for their contribution to the peer review of this work. Peer reviewer reports are available.

Reprints and permission information is available at http://www.nature.com/reprints

Publisher's note Springer Nature remains neutral with regard to jurisdictional claims in published maps and institutional affiliations.

Supplementary Information for:

Biosensor for branched-chain amino acid metabolism in yeast and applications in isobutanol and isopentanol production

Yanfei Zhang [1], Jeremy D. Cortez [# 2], Sarah K. Hammer [# 1], César Carrasco-López [1], Sergio Á. García Echauri [1], Jessica B. Wiggins [3], Wei Wang [3] and José L. Avalos * [1, 2, 4, 5]

[1] Department of Chemical and Biological Engineering; [2] Department of Molecular Biology; [3] Genomics Core Facility, Lewis-Sigler Institute for Integrative Genomics; [4] Andlinger Center for Energy and the Environment, [5] High Meadows Environmental Institute, Princeton University, Princeton, NJ

# These authors made equal contribution

*Corresponding author: José L. Avalos

Department of Chemical and Biological Engineering,

Princeton University,

101 Hoyt Laboratory, William Street, Princeton, NJ 08544, USA

Phone office: +1 (609) 258-9881

Phone lab: +1 (609) 258-0542

Fax: +1 (609) 258-1247

Email: javalos@princeton.edu

Supplementary Notes:

Supplementary Note 1: Additional details on the development and evaluation of different biosensor constructs. The BCHA biosensor is based on the transcriptional regulator Leu3p which activates genes involved in BCAA biosynthesis when bound to α-IPM and represses them when unbound[1,2]. Because the *LEU1* promoter (P_{LEU1}) is regulated by Leu3p, a yEGFP reporter downstream of P_{LEU1} can be used to monitor α-IPM intracellular levels, and thus BCAA biosynthetic activity. The enzyme responsible for α-IPM synthesis (Leu4p), however, is feedback inhibited by leucine which would block the biosynthetic pathway and thus the effector metabolite of the biosensor. Therefore, we tested three different *LEU4* mutants insensitive to leucine inhibition ($LEU4^{\Delta S547}$, $LEU4^{1\text{-}410}$, and $LEU4^{1\text{-}474}$), plus the wild type as control, expressed constitutively using the TPI1 promoter (P_{TPI1}). Because Leu4p is active as a dimer, it is possible that heterodimers of the endogenous wild type copy and mutant variants are formed ($Leu4^{WT}/Leu4^{variant}$), explaining some of the difference in performance we observed. When the BCHA biosynthesis pathway (plasmid pJA182) is overexpressed in *leu2*Δ strains harboring different biosensor constructs, the $LEU4^{1\text{-}410}$ variant lacking the leucine regulatory domain, produces the largest increase in fluorescence especially when a PEST tag is fused to yEGFP (Supplementary Fig. 2a). While *LEU2* deletion favors isobutanol production, the pathway bottleneck introduced by this deletion increases the accumulation of α-IPM, which explains why constructs with stable (untagged) yEGFP have higher background than those with a PEST tag and why destabilizing yEGFP helps lower the background and increase the apparent dynamic range (Fig. 1a, Supplementary Fig. 2a). The reason we chose to delete *LEU2* and not *LEU1* is twofold. First, the parent strain already contains a *LEU2* deletion as an auxotrophic marker so it is not necessary to also delete *LEU1* to prevent flux towards leucine biosynthesis. Additionally, we

hypothesize that the reversible activity of Leu1p could help reduce the biosensor background by dampening the accumulation of α-IPM. *LEU2* deletion also causes leucine auxotrophy, requiring supplementation of this amino acid in the growth medium; however the *LEU4*$^{1\text{-}410}$ leucine-insensitive mutant keeps the biosensor operational.

In contrast, for isopentanol production it is necessary to express *LEU2* (Supplementary Fig. 1). Therefore, to obtain a biosensor configuration suitable for isopentanol sensing, we tested the same constructs above but in a *LEU2* strain (Supplementary Fig. 2b). Because α-IPM is an intermediate metabolite of isopentanol biosynthesis (Supplementary Fig. 1), intracellular concentrations of α-IPM are expected to be substantially lower in strains engineered to make isopentanol than in *leu2Δ* strains that produce isobutanol, in which α-IPM can be considered to be a byproduct (Supplementary Fig. 1). Thus, using a PEST-tagged yEGFP in *LEU2* strains is counterproductive, and an untagged yEGFP enhances the biosensor sensitivity and apparent dynamic range (Supplementary Fig. 2b). In addition, we found that deleting the endogenous genes encoding for α-IPM synthases (*LEU4* and *LEU9*) reduces the biosensor background in *LEU2* strains. However, this requires replacing Leu4$^{1\text{-}410}$, which depends on heterodimerization with endogenous *LEU4* for activity, with another leucine-insensitive Leu4p mutant. The Leu4p harboring a Ser547 deletion (Leu4$^{\Delta S547}$)[3] is a leucine-insensitive mutant that is active as homodimers in the absence of wild type *LEU4*[4] , which in *LEU2* strains gives the largest apparent dynamic range (Supplementary Fig. 2b).

It is important to note that previous studies[5-8] have shown that small protein fusions cause no measurable effect on GFP quantum yield or brightness, including the PEST-Cln2 tag used in this study[5], which does not seem to impede biosensor functionality.

Supplementary Note 2: Biosensor dynamic range estimation.

Because the biosensor is based on the ability of Leu3p to respond to intracellular levels of α-IPM, it is difficult to measure its dynamic range. Feeding α-IPM or α-KIV in the media at relatively low concentrations (< 80 μM) helps confirm the biosensor response to elevated levels of α-IPM and its precursor (Supplementary Fig. 3a,b). However, the biosensor response saturates when feeding α-IPM above ~80 μM, or α-KIV above ~300 μM (Supplementary Fig. 3c,d). Since the stoichiometric ratio between these metabolites in the biosynthetic pathway is one to one, and the biosensor response is linear with respect to both metabolites up to ~ 80 μM, the saturation at different concentrations suggests there may be differences in the rates of cellular uptake of these metabolites, which likely become limiting at different concentrations. Similarly, differences in their metabolic conversion rates could greatly affect the biosensor response when feeding metabolites to the media. Therefore, caution should be taken when interpreting these results, which are unlikely to reflect the true dynamic range of the biosensor when these metabolites are instead produced in the BCAA biosynthetic pathway. Measuring the biosensor response using strains engineered to produce different levels of isobutanol or isopentanol (and thus produce different levels of α-IPM and α-KIV) is a more direct approach to studying the operational range of the biosensor as it is used in real applications (Fig. 1b,d); however, this method is still limited by the maximal productivity achieved in our best engineered strains. Therefore, these experiments provide at best a conservative estimate of the true dynamic range of the biosensor.

Supplementary Note 3: Mechanistic insights from intracellular α-IPM concentrations.

The relationship between biosensor readout, BCHA production, and intracellular α-IPM concentration is consistent with previous reports of Leu3p activation by this metabolite[1,2], and

reveals mechanistic differences between the isobutanol and isopentanol configurations of the biosensor. We observed a significant difference in α-IPM concentrations between an isobutanol-producing strain and a negative control, starting from the exponential phase (12h), which further increases through to the stationary phase (30h), (Supplementary Figure 4a,b). However, even though the α-IPM difference is larger in the stationary phase, the difference in biosensor output is larger during the exponential phase, which is consistent with our initial observation that data from the exponential phase is more reliable and reproducible. The rapid drop in biosensor output during the stationary phase is likely due to increased GFP degradation rate, exacerbated by the PEST tag, although other factors that may contribute by repressing Leu3p or P_{LEU1} activity in the stationary phase cannot be ruled out. These observations contrast with isopentanol-producing strains and the isopentanol-configured biosensor, in which the difference in α-IPM concentration between an isopentanol-producing strain and a negative control is not significant until the stationary phase measurement, yet the difference in biosensor output during the stationary phase is substantially larger than what is observed in the isobutanol-producing strain with the isobutanol-configured biosensor (Supplementary Figure 4d,e). This is consistent with the fact that *LEU2* is deleted in the isobutanol-producing strains but not in the isopentanol-producing strains, which would be expected to cause α-IPM accumulation in the former but not the later strains. It is also consistent with the fact that the GFP reporter in the isopentanol-configured biosensor does not have a PEST tag, which makes its response more sensitive to low α-IPM concentrations and longer-lasting into the stationary phase. Interestingly, the isopentanol-configured biosensor is more sensitive to small differences in α-IPM concentrations in the lag and exponential phases of fermentation than our method using U-HPLC-orbitrap MS to measure intracellular α-IPM concentrations from cell cultures. The large difference in intracellular concentrations of α-IPM between the isobutanol and

isopentanol strains, due to the different *LEU2* backgrounds, explains why the isobutanol-configured biosensor functions optimally with a PEST tag fused to the GFP reporter (to avoid high background and possibly early GFP saturation due to the higher α-IPM concentration), while the isopentanol-configured biosensor demonstrates increased sensitivity to lower α-IPM concentrations without a PEST tag.

These results also explain why biosensor measurements taken during the exponential phase are most predictive of BCHA production even though those differences are better observed in measurements taken during the stationary phase (Supplementary Figure 4a,b,d,e). During the exponential phase, both biosensor configurations display the highest sensitivity to small differences in α-IPM concentrations (as discussed above and shown in Supplementary Figure 4a,b,d,e). Conversely, while BCHA production increases dramatically by the time the fermentation reaches stationary phase, both biosensor configurations are less sensitive to even large variations in α-IPM concentrations between strains at this late stage of the fermentation (possibly due, at least in part, to increased GFP degradation and extraneous Leu3p or P_{LEU1} regulation). BCHA concentrations at early to mid-exponential phase of fermentation (when biosensor readout is most predictive), are nonetheless lower (and thus more difficult to measure) than in stationary phase, likely due, at least in part, to lower cell concentrations and shorter time given to convert glucose to products in these early phases. This is especially true when comparing low cell density fermentations in 2% glucose (used in FACS to isolate high-producing strains and in the experiments shown in new Supplementary Figure 4) to high cell density fermentations in higher glucose concentrations (used in BCHAs production fermentations in most of the study). Nevertheless, biosensor outputs measured during the exponential phase can clearly predict

differences in the accumulated BCHA production after 24-48 hours of fermentation, including in high cell density fermentations. Therefore, we used biosensor measurements in the exponential phase of low cell density fermentations to isolate higher-producing strains, whose enhanced productivity we then confirmed in high cell density 48h fermentations, notably obtaining very low rates of false-positives (Supplementary Figure 15).

Supplementary Note 4: Additional structural analysis of *ILV6* mutants that enhance isobutanol production isolated with the biosensor. Val110, which when mutated to glutamate results in the most active variant, is located inside the putative valine binding site, interacting with the L91 residue mutated in $ILV6^{V90D/L91F}$ (Supplementary Fig. 8b). Several other mutations that increase Ilv2p activity, found multiple times in several isolated *ILV6* variants, are also located inside the valine binding pocket (N86, V90, L91, and N104), consistent with other mutations previously reported to make Ilv2p or its homologues insensitive to valine inhibition[9-13].

Supplementary Note 5: Additional structural analysis of *LEU4* mutants that enhance isopentanol production isolated with the biosensor. Mutating residue H541 has been previously reported to make Leu4p resistant to Zn^{2+}-mediated inactivation by CoA[3]. The residues corresponding to mutations Y538N, V584E, and T590I are located inside the leucine binding site, and Y485N in its vicinity suggesting that they result in decreased sensitivity to leucine inhibition. Seven residues (K51, Q439, F497, N515, V584, D578, and T590) are substituted in more than one variant and at least one of them is mutagenized in 14 of the 19 variants containing two or more mutations (Supplementary Tables 5 and 6). Residues Q439, F497, N515, V584, D578, and T590 are located in the regulatory domain (Supplementary Fig. 11), making it likely that they are also

involved in reducing regulatory inhibition of Leu4p. Most of them are located inside or in the vicinity of the regulatory leucine binding site. Remarkably, N515, located inside the leucine binding site, is substituted in five of the 24 variants we identified, including *LEU4* mutant #6, which is the variant that produces most isopentanol. On the other hand, Q439 is far from the leucine binding site but close to H541, suggesting it might be involved in Zn^{2+}-mediated CoA inactivation of Leu4p (Supplementary Fig. 11).

Supplementary Note 6: **Additional structural analysis of *Ll-ilvD* mutants that enhance cytosolic isobutanol production isolated with the biosensor.** The lobes that define the putative substrate entrance to the active site are known to undergo a significant conformational change[14]. In one conformation, the lobes seal the active site away from the solvent surrounding the enzyme (Supplementary Fig. 14c), presumably to protect the 2Fe-2S cluster in the active site from oxidation. In the other conformation, the lobes move apart from each other to open the entrance to the active site, probably to allow substrates and products to enter and exit (Supplementary Fig. 14d). This mechanism suggests that there is a balance between protecting the catalytic 2Fe-2S cluster from oxidation and allowing substrate and product exchange in the active site. Therefore, it is an intriguing possibility that mutations I433V and S189P improve enzyme activity by shifting this balance to one more optimal for the conditions in the yeast cytosol. Finally, mutation V12A, is located near the N-terminus of the enzyme, in a region involved in packing the tetramer and stabilizing the C-terminal H579, which coordinates the catalytic Mg^{2+} in the active site (Supplementary Fig. 14e). It is possible that this mutation increases the stability of these structural features to enhance enzymatic activity.

Supplementary Note 7: Supplementary methods for optogenetic experiments. Blue LED panels (HQRP New Square 12" Grow Light Blue LED 14W, Amazon) were placed above the 24-well microtiter plates to stimulate cell growth with blue light at an intensity range of 70-90 μmol m^{-2} s^{-1} and duty cycles of 15 s on and 65 s off. The vertical distance between the LED panel and the top of the 24-well plates was adjusted based on the light intensity of each LED panel, measured with a spectrum quantum meter (Cat. MQ-510, Apogee Instruments, Inc., UT, USA). The light duty cycles were achieved by regulating the LED panels using a Nearpow Multifunctional Infinite Loop Programmable Plug-in Digital Timer Switch (purchased from Amazon). Single colonies were grown overnight in 1 mL of SC or SC-ura medium supplemented with 2% glucose in individual wells of the 24-well microtiter plates under constant blue light in an orbital shaker (Eppendorf, New Brunswick, USA) at 30°C and at 200 rpm agitation. The next day, each overnight culture was used to inoculate 1 mL of the same medium to reach an initial OD_{600} of 0.1 and grown at 30°C, 200 rpm, and under pulsed blue light (15 s on and 65 s off). We incubated the cultures in the light until they reached different cell densities (ρ), at which we switched them from light to dark. The 24-well plates were kept in the dark by wrapping them with aluminum-foil (and continuing to incubate at 30 °C, 200 rpm) for θ hours (the incubation time in the dark). After the dark incubation period, the cells were centrifuged and re-suspended in 1 mL of fresh SC-ura medium supplemented with 2% glucose. The plates were covered with sterile adhesive SealPlate® films (Cat. # STR-SEAL-PLT; Excel Scientific, Victorville, CA) and incubated in the dark (wrapped in aluminum foil) for 48 h at 30°C and 200 rpm shaking. Subsequently, the cultures were centrifuged for 5 min at 1000 rpm, and the supernatants were collected and used for HPLC analysis.

Supplementary Tables

Supplementary Table 1. Yeast strains used in this study.

Strain	Description	Genotype (Plasmid contents in parenthesis)	Source
CEN.PK2-1C	Wild-type *Saccharomyces cerevisiae*	*MAT**a** ura3-52 trp1-289 leu2-3,112 his3-1 MAL2-8^{c} SUC2*	[15]
YZy81	*bat1Δ*, isobutanol-configured biosensor (cassette from pYZ16)	CEN.PK2-1C, *his3*::*HIS3*-P_{LEU1}-yEGFP-PEST-T_{ADH1}-P_{TPI1}-*LEU4*$^{1-410}$-T_{PGK1}, *bat1Δ*::hphMX	This study
YZy90	*pdc1Δ, pdc5Δ, pdc6Δ*, *gal80Δ*, pJLA121-*PDC1*^{0202}	CEN. PK2-1C, *pdc1Δ, pdc5Δ, pdc6Δ, gal80Δ*::lox71-kanMX-lox66, 2μ *URA3* plasmid (P_{TFE1}-*PDC1*-T_{ACT1})	This study
YZy91	*bat1Δ, bat2Δ, ilv6Δ*, isobutanol-configured biosensor (cassette from pYZ16)	CEN.PK2-1C, *his3*::*HIS3*-P_{LEU1}-yEGFP-PEST-T_{ADH1}-P_{TPI1}-*LEU4*$^{1-410}$-T_{PGK1}, *bat1Δ*::hphMX *bat2Δ*::lox71-kanMX-lox66 *ilv6Δ*::lox71-natMX-lox66	This study
YZy121	CEN.PK2-1C, isobutanol-configured biosensor (cassette from pYZ16)	CEN.PK2-1C, *his3*::*HIS3*-P_{LEU1}-yEGFP-PEST-T_{ADH1}-P_{TPI1}-*LEU4*$^{1-410}$-T_{PGK1}	This study
YZy140	*bat1Δ, leu4Δ, leu9Δ, LEU2* restored	CEN.PK2-1C, *bat1Δ*::hphMX *leu4Δ*::lox71-kanMX-lox66 *leu9Δ*::lox71-natMX-lox66 *leu2::LEU2*	This study
YZy148	*bat1Δ, leu4Δ, leu9Δ, LEU2* restored, modified isopentanol-configured biosensor (cassette from pYZ24)	CEN. PK2-1C, *his3*::*HIS3*-P_{LEU1}-yEGFP-T_{ADH1} *bat1Δ*::hphMX *leu4Δ*::lox71-kanMX-lox66 *leu9Δ*::lox71-natMX-lox66 *leu2*::*LEU2*	This study
YZy230	YZy121, cassette from pYZ33 (Strain 1)	YZy121, δ-integration-P_{TDH3}-*ILV2*_cHATag-T_{ADH1}, P_{PGK1}-*ILV3*_cHisTag-T_{CYC1}, P_{TEF1}-*ILV5*_cMycTag-T_{ACT1}	This study
YZy231	YZy121, cassette from pYZ33 (Strain 2)	YZy121, δ-integration-P_{TDH3}-*ILV2*_cHATag-T_{ADH1}, P_{PGK1}-*ILV3*_cHisTag-T_{CYC1}, P_{TEF1}-*ILV5*_cMycTag-T_{ACT1}	This study

Strain	Description	Genotype (Plasmid contents in parenthesis)	Source
YZy232	YZy121, cassette from pYZ33 (Strain 3)	YZy121, δ-integration-P_{TDH3}-*ILV2*-cHATag-T_{ADH1}-P_{PGK1}-*ILV3*-cHisTag-T_{CYC1}-P_{TEF1}-*ILV5*-cMycTag-T_{ACT1}	This study
YZy233	YZy81, cassette from pYZ33 (Strain 1)	YZy81, δ-integration-P_{TDH3}-*ILV2*-cHATag-T_{ADH1}-P_{PGK1}-*ILV3*-cHisTag-T_{CYC1}-P_{TEF1}-*ILV5*-cMycTag-T_{ACT1}	This study
YZy234	YZy81, cassette from pYZ33 (Strain 2)	YZy81, δ-integration-P_{TDH3}-*ILV2*-cHATag-T_{ADH1}-P_{PGK1}-*ILV3*-cHisTag-T_{CYC1}-P_{TEF1}-*ILV5*-cMycTag-T_{ACT1}	This study
YZy235	YZy81, cassette from pYZ34 (Strain 1)	YZy81, δ-integration-P_{TDH3}-*ILV2*-cHATag-T_{ADH1}-P_{PGK1}-*ILV3*-cHisTag-T_{CYC1}-P_{TEF1}-$CoxIV_{MLS}$-*Ll_adhA*^{RE1}-cMycTag-T_{ACT1}-[P_{TDH3}-$CoxIV_{MLS}$-*ARO10*-cHATag-T_{ADH1}-P_{TEF1}-*ILV5*-cMycTag-T_{ACT1}]	This study
YZy236	YZy81, cassette from pYZ34 (Strain 2)	YZy81, δ-integration-P_{TDH3}-*ILV2*-cHATag-T_{ADH1}-P_{PGK1}-*ILV3*-cHisTag-T_{CYC1}-P_{TEF1}-$CoxIV_{MLS}$-*Ll_adhA*^{RE1}-cMycTag-T_{ACT1}-[P_{TDH3}-$CoxIV_{MLS}$-*ARO10*-cHATag-T_{ADH1}-P_{TEF1}-*ILV5*-cMycTag-T_{ACT1}]	This study
YZy311	YZy91, pYZ127	YZy91, CEN *URA3* plasmid (P_{TDH3}-*ILV6*-T_{ADH1})	This study
YZy312	YZy91, pYZ228	YZy91, CEN *URA3* plasmid (P_{TDH3}-*ILV6*^{V110E}-T_{ADH1})	This study
YZy313	YZy363, pYZ127	YZy363, CEN *URA3* plasmid (P_{TDH3}-*ILV6*-T_{ADH1})	This study
YZy314	YZy363, pYZ228	YZy363, CEN *URA3* plasmid (P_{TDH3}-*ILV6*^{V110E}-T_{ADH1})	This study
YZy363	YZy81, overexpressing the mitochondrial isobutanol pathway via δ-integration using cassette from pYZ34	YZy81, δ-integration-P_{TDH3}-*ILV2*-cHATag-T_{ADH1}-P_{PGK1}-*ILV3*-cHisTag-T_{CYC1}-P_{TEF1}-$CoxIV_{MLS}$-*Ll_adhA*^{RE1}-cMycTag-T_{ACT1}-[P_{TDH3}-$CoxIV_{MLS}$-*ARO10*-cHATag-T_{ADH1}-P_{TEF1}-*ILV5*-cMycTag-T_{ACT1}]	This study
YZy418	*ilv3Δ,* isobutanol-configured biosensor (cassette from pYZ16)	CEN.PK2-1C, *his3*::*HIS3*-P_{LEU1}-yEGFP-PEST-T_{ADH1}-P_{TPI1}-*LEU4*$^{1-410}$-T_{PGK1}, *ilv3Δ*:: lox71-hphMX-lox66	This study
YZy443	YZy418, *tma29Δ*	YZy418, *tma29Δ*::lox71-kanMX-lox66	This study

Strain	Description	Genotype (Plasmid contents in parenthesis)	Source
YZy447	YZy443, cytosolic isobutanol pathway (cassette from pYZ196)	YZy443, *ura3Δ*::loxP-*URA3*-loxP-P_{TDH3}-*AFT1*-T_{ADH1}-[P_{TEF1}-*Bs_alsS*-T_{ACT1}-P_{TDH3}-*Ec_ilvC*$^{P2D1\text{-}A1}$-T_{ADH1}]-P_{GAL10}-*Ll_ilvD*-T_{ACT1}	This study
YZy449	YZy447, *ura3Δ* marker restored	YZy447, *ura3*Δ	This study
YZy452	YZy449, (cassette from pYZ206)	YZy449, δ-integration-P_{TDH3}-*Ec_ilvC*$^{P2D1\text{-}A1}$-T_{ADH1}-[P_{TEF1}- *Ec_ilvC*$^{P2D1\text{-}A1}$-T_{ACT1}]	This study
YZy453	YZy452, pYZ125	YZy452, empty CEN *URA3* plasmid	This study
YZy454	YZy452, pYZ126	YZy452, CEN *URA3* plasmid (P_{TDH3}-*Ll_ilvD*-T_{ADH1})	This study
YZy468	YZy452, pYZ341	YZy452, 2μ *URA3* plasmid (P_{TDH3}-*Ll_ilvD*-T_{ADH1})	This study
YZy469	YZy452, pYZ353	YZy452, CEN *URA3* plasmid (P_{TDH3}-*Ll_ilvD*^{I433V}-T_{ADH1})	This study
YZy470	YZy452, pYZ342	YZy452, 2μ *URA3* plasmid (P_{TDH3}-*Ll_ilvD*^{I433V}-T_{ADH1})	This study
YZy480	YZy90, OptoINVRT7, 2μ plasmid pJLA121- *PDC1*^{0202}	YZy90, *his3*::*HIS3*-P_{TEF1}-EL222-T_{CYC1}-P_{C120}-*GAL80*-ODC^{mut}-T_{ACT1}-[P_{C120}-*GAL80*-ODC^{mut}-T_{ACT1}]-P_{PGK1}-*GAL4*-PSD^{V19L}-T_{ADH1}, 2μ *URA3* plasmid (P_{TEF1}-*PDC1*-T_{ACT1})	This study
YZy481	YZy90, OptoINVRT7, 2μ plasmid pJLA121- *PDC1*^{0202} removed	YZy90, *his3*::*HIS3*-P_{TEF1}-EL222-T_{CYC1}-P_{C120}-*GAL80*-ODC^{mut}-T_{ACT1}-[P_{C120}-*GAL80*-ODC^{mut}-T_{ACT1}]-P_{PGK1}-*GAL4*-PSD^{V19L}-T_{ADH1}	This study
YZy487	YZy481, isobutanol-configured biosensor integrated to *GAL80* locus (using the cassette from pYZ414)	YZy481, *gal80*::Lox71-natMX6-Lox66-P_{LEU1}-yEGFP-PEST-T_{ADH1}-P_{TPI1}-*LEU4*$^{1\text{-}410}$-T_{PGK1}	This study
YZy502	YZy487, OptoEXP *PDC1* and OptoINVRT7 cytosolic isobutanol pathway	YZy487, δ-integration-P_{C120}-*PDC1*-T_{ACT1}-P_{TDH3}-*Ec_ilvC*$^{P2D1\text{-}A1}$-T_{CYC1}-P_{TEF1}-*Ll_ilvD*^{I433V}-T_{TPS1}-$P_{GAL1\text{-}S}$-*Bs_alsS*-T_{ACT1}	This study

Strain	Description	Genotype (Plasmid contents in parenthesis)	Source
YZy505	YZy502, partial cytosolic isobutanol pathway lacking *Bs_alsS* (pYZ350)	YZy502, 2μ *URA3* plasmid (P_{TDH3}-*Ec_ilvC*$^{P2D1\text{-}A1}$-T_{CYC1}-[P_{TEF1}-*Ec_ilvC*$^{P2D1\text{-}A1}$-T_{ACT1}-P_{TDH3}-*Ll_ilvD*^{I433V}-T_{ADH1}]-P_{PGK1}-*ARO10*-cHATag-T_{CYC1}-P_{TEF1}-*Ll_adhA*^{RE1}-cMycTag-T_{ACT1})	This study
SHy1	*bat1Δ*	CEN.PK2-1C, *bat1Δ*::hphMX	[13]
SHy134	*bat1Δ, leu4Δ, leu9Δ, LEU2* restored, isopentanol-configured biosensor (cassette from pYZ25)	CEN.PK2-1C, *his3*::*HIS3*-P_{LEU1}-yEGFP-T_{ADH1}-P_{TPI1}-*LEU4*$^{\Delta S547}$-T_{PGK1} *bat1Δ*::hphMX *leu4Δ*::lox71-kanMX-lox66 *leu9Δ*::lox71-natMX-lox66 *leu2::LEU2*	This study
SHy158	SHy134, pYZ125	SHy134, empty CEN *URA3* plasmid	This study
SHy159	SHy134, JLAb691	SHy134, CEN *URA3* plasmid (P_{TDH3}-*ILV2*_cHATag-T_{ADH1}, P_{PGK1}-*ILV3*_cHisTag-T_{CYC1}, P_{TEF1}-*ILV5*_cMycTag-T_{ACT1})	This study
SHy176	SHy134, JLAb705	SHy134, CEN *URA3* plasmid (P_{TDH3}-*ILV1*_cHATag-T_{ADH1})	This study
SHy181	*leu4Δ, leu9Δ, LEU2* restored, *BAT1* restored, isopentanol-configured biosensor (cassette from pYZ25)	CEN. PK2-1C, *his3*::*HIS3*-P_{LEU1}-yEGFP-T_{ADH1}-P_{TPI1}-*LEU4*$^{\Delta S547}$-T_{PGK1} *leu4Δ*::lox71-kanMX-lox66 *leu9Δ*::lox71-natMX-lox66 *leu2*::*LEU2 trp1*::*TRP1*-P_{BAT1}-*BAT1*-T_{BAT1}	This study
SHy187	SHy181, pYZ125	SHy181, empty CEN *URA3* plasmid	This study
SHy188	SHy181, JLAb691	SHy181, CEN *URA3* plasmid (P_{TDH3}-*ILV2*_cHATag-T_{ADH1}, P_{PGK1}-*ILV3*_cHisTag-T_{CYC1}, P_{TEF1}-*ILV5*_cMycTag-T_{ACT1})	This study
SHy192	SHy181, JLAb705	SHy181, CEN *URA3* plasmid (P_{TDH3}-*ILV1*_cHATag-T_{ADH1})	This study

Supplementary Table 2. Plasmids used in this study.

Plasmid	Description [Brackets indicate inverted orientation]	Source
pRS416	Amp^R, CEN, URA3	[16]
pRS426	Amp^R, 2μ, URA3	[17]
pYZ1	Amp^R, 2μ, TRP1, P_{TPI1}-*LEU4*$^{\Delta S547}$_FLAG-T_{PGK1}	This study
pYZ2	Amp^R, 2μ, TRP1, P_{TPI1}-*LEU4*$^{1-410}$_FLAG-T_{PGK1}	This study
pYZ12B	Amp^R, *HIS3* locus integration vector (His3INT)	[18]
pYZ13	Amp^R, 2μ, URA3, P_{LEU1}-yEGFP_PEST-T_{ADH1}	This study
pYZ14	Amp^R, His3INT, P_{LEU1}-yEGFP_PEST-T_{ADH1}	This study
pYZ15	Amp^R, His3INT, P_{LEU1}-yEGFP_PEST-T_{ADH1}, P_{TPI1}-*LEU4*$^{\Delta S547}$_FLAG-T_{PGK1}	This study
pYZ16	(Isobutanol-configured biosensor) Amp^R, His3INT, P_{LEU1}-yEGFP_PEST-T_{ADH1}-P_{TPI1}-*LEU4*$^{1-410}$_FLAG-T_{PGK1}	This study
pYZ17	Amp^R, Lox71-kanMX-Lox66 gene-disruption cassette	[19]
pYZ23	Amp^R, δ-integration vector, Lox71-bleMX6-Lox66	[18]
pYZ24	(Modified isobutanol-configured biosensor without leucine-insensitive Leu4p mutant) Amp^R, His3INT, P_{LEU1}-yEGFP-T_{ADH1}	This study
pYZ25	(Isopentanol-configured biosensor) Amp^R, His3INT, P_{LEU1}-yEGFP-T_{ADH1}-P_{TPI1}-*LEU4*$^{\Delta S547}$_FLAG-T_{PGK1}	This study
pYZ26	Amp^R, His3INT, P_{LEU1}-yEGFP-T_{ADH1}-P_{TPI1}-*LEU4*$^{1-410}$_FLAG-T_{PGK1}	This study

pYZ33	(δ-integration-*ILV*s) Amp^R, δ-integration-Lox71-ShBle-Lox66-P_{TDH3}-*ILV2*-cHATag-T_{ADH1}-P_{PGK1}-*ILV3*-cHisTag-T_{CYC1}-P_{TEF1}-*ILV5*-cMycTag-T_{ACT1}	[4]
pYZ34	(δ-integration-ILVs, $CoxIV_{MLS}$-*ARO10*, $CoxIV_{MLS}$-*Ll_adhA*^{RE1}) Amp^R, δ-integration-Lox71-ShBle-Lox66-P_{TDH3}-*ILV2*-cHATag-T_{ADH1}-P_{PGK1}-*ILV3*-cHisTag-T_{CYC1}-P_{TEF1}-$CoxIV_{MLS}$-*Ll_adhA*^{RE1}-cMycTag-T_{ACT1}-[P_{TDH3}-$CoxIV_{MLS}$-*ARO10*-cHATag-T_{ADH1}-P_{TEF1}-*ILV5*-cMycTag-T_{ACT1}]	[19]
pYZ55	Amp^R, Lox71-hphMX-Lox66 gene-disruption cassette	[19]
pYZ57	Amp^R, His3INT, P_{LEU1}-yEGFP-T_{ADH1}-P_{TPI1}-*LEU4*$^{1-474}$_FLAG-T_{PGK1}	This study
pYZ61	Amp^R, His3INT, P_{LEU1}-yEGFP_PEST-T_{ADH1}, P_{TPI1}-*LEU4*$^{1-474}$_FLAG-T_{PGK1}	This study
pYZ84	Amp^R, Lox71-natMX-Lox66 gene-disruption cassette	[19]
pYZ113	(δ-integration-$CoxIV_{MLS}$-*ARO10*, $CoxIV_{MLS}$-*Ll_adhA*^{RE1}) Amp^R, δ-integration-Lox71-ShBle-Lox66-P_{TDH3}-$CoxIV_{MLS}$-*ARO10*-cHATag-T_{ADH1}-[P_{TEF1}-$CoxIV_{MLS}$-*Ll_adhA*^{RE1}-cMycTag-T_{ACT1}]	This study
pYZ125	Amp^R, CEN, URA3, P_{TDH3}-MCS-T_{ADH1}	This study
pYZ126	Amp^R, CEN, URA3, P_{TDH3}-*Ll_ilvD*-T_{ADH1}	This study
pYZ127	Amp^R, CEN, URA3, P_{TDH3}-*ILV6*-T_{ADH1}	This study
pYZ148	Amp^R, CEN, URA3, P_{TDH3}-*ILV6*$^{V90D/L91F}$-T_{ADH1}	This study
pYZ149	Amp^R, CEN, URA3, P_{TDH3}-*LEU4*-T_{ADH1}	This study
pYZ154	Amp^R, CEN, URA3, P_{TDH3}-*LEU4*$^{\Delta S547}$-T_{ADH1}	This study
pYZ155	Amp^R, CEN, URA3, P_{TDH3}-*LEU4*$^{1-410}$-T_{ADH1}	This study
pYZ196	(Cytosolic isobutanol pathway containing P_{GAL10}-*Ll_ilvD*)	This study

	Amp^{R}, Ura3 Locus integration-LoxP-*URA3*-LoxP- P_{TDH3}-*AFT1*-T_{ADH1}-[P_{TEF1}-*Bs_alsS*-T_{ACT1}-P_{TDH3}-*Ec_ilvC*$^{P2D1\text{-}A1}$-T_{ADH1}]-P_{GAL10}-*Ll_ilvD*-T_{ACT1}	
pYZ206	(δ-integration-two copies of *Ec_ilvC*$^{P2D1\text{-}A1}$)	This study
	Amp^{R}, δ-integration-Lox71-ShBle-Lox66-P_{TDH3}-*Ec_ilvC*$^{P2D1\text{-}A1}$-T_{ADH1}-[P_{TEF1}-*Ec_ilvC*$^{P2D1\text{-}A1}$-T_{ACT1}]	
pYZ223	Amp^{R}, Lox71-natMX6-Lox66, *GAL80* Locus Integration vector (Gal80INT-Lox71-natMX6-Lox66)	This study
pYZ228	Amp^{R}, CEN, URA3, P_{TDH3}-*ILV6*^{V110E}-T_{ADH1}	This study
pYZ341	Amp^{R}, 2μ, URA3, P_{TDH3}-*Ll_ilvD*-T_{ADH1}	This study
pYZ342	Amp^{R}, 2μ, URA3, P_{TDH3}-*Ll_ilvD*^{I433V}-T_{ADH1}	This study
pYZ350	(Partial cytosolic isobutanol pathway containing *ARO10, Ll_adhA*^{RE1}, *Ll_ilvD*^{I433V}, and extra copies of *Ec_ilvC*$^{P2D1\text{-}A1}$; lacking *Bs_alsS*)	This study
	Amp^{R}, 2μ, URA3, P_{TDH3}-*Ec_ilvC*$^{P2D1\text{-}A1}$-T_{CYC1}-[P_{TEF1}-*Ec_ilvC*$^{P2D1\text{-}A1}$-T_{ACT1}]-[P_{TDH3}-*Ll_ilvD*^{I433V}-T_{ADH1}]-P_{PGK1}-*ARO10*-cHATag-T_{CYC1}-P_{TEF1}-*Ll_adhA*^{RE1}-cMycTag-T_{ACT1}	
pYZ353	Amp^{R}, CEN, URA3, P_{TDH3}-*Ll_ilvD* ^{I433V}-T_{ADH1}	This study
pYZ383	Amp^{R}, 2μ, URA3, P_{TEF1}-*Ll_ilvD*^{I433V}-T_{TPS1}	This study
pYZ384	Amp^{R}, 2μ, URA3, $P_{Gal1\text{-}S}$-*Bs_alsS*-T_{ACT1}	This study
pYZ414	Amp^{R}, Gal80INT-Lox71-natMX6-Lox66-Isobutanol-configured biosensor (P_{LEU1}-yEGFP_PEST-T_{ADH1}-P_{TPI1}-*LEU4*$^{1\text{-}410}$_FLAG-T_{PGK1})	This study
pYZ417	(δ-integration-OptoEXP-*PDC1*-OptoINVRT7-cytosolic isobutanol pathway)	This study
	Amp^{R}, δ-integration-Lox71-ShBle-Lox66-OptoEXP-*PDC1* (P_{C120}-*PDC1*-T_{ACT1})-OptoINVRT7-cytosolic isobutanol pathway (P_{TDH3}- *Ec_ilvC*$^{P2D1\text{-}A1}$-T_{CYC1}-P_{TEF1}-*Ll_ilvD*^{I433V}-T_{TPS1}-$P_{Gal1\text{-}S}$-*Bs_alsS*-T_{ACT1})	
EZ-L235	(δ-integration-OptoEXP-*PDC1*)	[18]
	Amp^{R}, δ-integration-Lox71-ShBle-Lox66-OptoEXP-*PDC1* (P_{C120}-*PDC1*-T_{ACT1})	

EZ-L439	(OptoINVRT7) Amp^R, His3INT-P_{TEF1}-EL222-T_{CYC1}-P_{C120}-*GAL80*-ODC^{mut}-T_{ACT1}-[P_{C120}-*GAL80*-ODC^{mut}-T_{ACT1}]-P_{PGK1}-*GAL4*-PSD^{V19L} -T_{ADH1}	[20]
pAG26	Amp^R, Plasmid containing hphMX gene-disruption cassette	[21]
pJA123	Amp^R, 2µ, URA3, P_{TDH3}-*ILV2*-cHATag-T_{ADH1}-P_{PGK1}-*ILV3*-cHisTag-T_{CYC1}-P_{TEF1}-*ILV5*-cMycTag-T_{ACT1}	[22]
pJA182	Amp^R, 2µ, URA3, P_{TDH3}-*ILV2*-HA-T_{ADH1}-P_{PGK1}-*ILV3*-cHisTag-T_{CYC1}-P_{TEF1}-$CoxIV_{MLS}$-*Ll_adhA*^{RE1}-cMycTag-T_{ACT1}-[P_{TDH3}-$CoxIV_{MLS}$-*ARO10*-cHATag-T_{ADH1}-P_{TEF1}-*ILV5*-cMycTag-T_{ACT1}]	[22]
pJA248	Amp^R, Plasmid containing yEGFP and PEST protein degradation tag	This study
pJLA121-*PDC1*^{0202}	Amp^R, 2µ, URA3, P_{TFE1}-*PDC1*-T_{ACT1}	[18]
JLAb23	Amp^R, 2µ, URA3, pRS426-P_{TPI1}-MCS_FLAG-T_{PGK1}	This study
JLAb131	Amp^R, 2µ, URA3, pJLA121^{0103}- P_{TDH3}-MCS-T_{ADH1}	This study
JLAb581	Amp^R, 2µ, URA3, P_{TDH3}-$CoxIV_{MLS}$-*ARO10*-cHATag-T_{ADH1}-[P_{TEF1}- $CoxIV_{MLS}$-*Ll_adhA*^{RE1}-cMycTag-T_{ACT1}]	[13]
JLAb691	Amp^R, CEN, URA3, P_{TDH3}-*ILV2*_cHATag-T_{ADH1}-P_{PGK1}-*ILV3*_cHisTag-T_{CYC1}-P_{TEF1}-*ILV5*_cMycTag-T_{ACT1}	This study
JLAb705	Amp^R, CEN, URA3, P_{TDH3}-*ILV1*_cHATag-T_{ADH1}	This study
pSH63	Amp^R, CEN, TRP1, P_{GAL1}_Cre_T_{CYC1}	[23]

Supplementary Table 3. Digital droplet PCR to identify the average cassette integration genotype of the pre-sorted library (PSL) and genotypes of the six colonies producing ~700 mg/L of isobutanol or above (Y436-Y443), isolated after two rounds of FACS. Source data are provided as a Source Data file.

	Positive counts				Cassette Integrations		
GDNA	**A + C**	**B + C**	**A + B + C**	**R**	**A**	**B**	**C**
CEN.PK2	0	362	0	448	n.a	n.a	n.a
PSL	436	440	544	494	0.21	0.22	0.67
Y436	1160	532	1236	690	2	0	0
Y437	1150	598	1252	768	2	0	0
Y438	1008	544	1112	570	2	0	0
Y439	1026	484	1072	576	2	0	0
Y442	632	1146	1298	672	1	1	0
Y443	524	1064	1030	538	1	1	0

A = Upstream pathway cassette (*ILV2, ILV5, ILV3*)
B = Downstream pathway cassette (*ARO10, Ll_adhA*^{RE1})
C = Complete pathway cassette (*ILV2, ILV5, ILV3, ARO10, Ll_adhA*^{RE1})
R = Single copy genome reference
n.a. = Not applicable

Cassette integrations were obtained by solving the following system of equations, where X is the copy number of the zeocin resistance cassette, Y is the copy number of *ILV2*, and Z is the copy number of *ARO10* measured by ddPCR (see methods):

$$A + B + C = X \quad \text{(Eq. 1)}$$
$$A + C = Y \quad \text{(Eq. 2)}$$
$$B + C + 1 = Z \quad \text{(Eq. 3)}$$

Supplementary Table 4. Amino acid mutations found in the sequenced Ilv6p variants.

Mutants	Mutations
Derived from wild-type *ILV6* random mutagenesis library	
ILV6_mutant_1	N104S
ILV6_mutant_2	S71P_N86T
ILV6_mutant_3	N86T
ILV6_mutant_4	V90A
ILV6_mutant_5	M21I_Y34C_N223Y
ILV6_mutant_6	V110E
ILV6_mutant_7	N86Y
ILV6_mutant_8	L91S
ILV6_mutant_9	N104S_E133V_S184F_G233E
ILV6_mutant_10	M21I_N57S_V79D_E133G_L161Q_T185A_N186S_D224Y_K284E_E288K
Derived from *ILV6*$^{V90D/L91F}$ random mutagenesis library	
ILV6_mutant_11	V90D_L91F_D292N
ILV6_mutant_12	V90D_L91F_H219L
ILV6_mutant_13	V90D_L91F_N112S
ILV6_mutant_14	V90D_L91F_T185A
ILV6_mutant_15	N86D_V90D_L91F
ILV6_mutant_16	N86S_V90D_L91F_K202M
ILV6_mutant_17	V90D_L91F_F174S
ILV6_mutant_18	V90D_L91F_N153Y_E198G
ILV6_mutant_19	P47T_Q85R_V90D_L91F_H180R
ILV6_mutant_20	V90D_L91F_V267A
ILV6_mutant_21	V90D_L91F_Q126L_S286R
ILV6_mutant_22	V90D_L91F_H180Y_I239V
ILV6_mutant_23	R11H_V84M_V90D_L91F_F174I
ILV6_mutant_24	V90D_L91F_Q193R

Supplementary Table 5. Amino acid mutations found in the sequenced Leu4p variants.

Mutants	Mutations
Derived from mutagenesis library of full-length *LEU4*	
LEU4_mutant_1	Y203F_V425D_N515I
LEU4_mutant_2	K25N_A60T_T316N_L330M_D433G_K467R_F497L_D509G_N515D_L529M_A552V_I602L
LEU4_mutant_3	N72S_K97R_S126G_R344H_R495G_N515D
LEU4_mutant_4	V446A_G544C_N593Y
LEU4_mutant_5	H541R
LEU4_mutant_6	E86D_K191N_K374R_A445T_S481R_N515I_A568V_S601A
LEU4_mutant_7	T287A_P400L_N515H_N537T
LEU4_mutant_8	A144T_N240S_D578N
LEU4_mutant_9	K90M_Q439R_S542P
LEU4_mutant_10	R428G_N486D
LEU4_mutant_11	K51R_E233K_F377I_L427S_K458E_F497I_E577D
LEU4_mutant_12	R392G_S459L_V584A
LEU4_mutant_13	K51R_A182V_V198T_A551V
Derived from mutagenesis library of regulatory domain	
LEU4_mutant_14	Y485N
LEU4_mutant_15	A450S_D451G_D578E
LEU4_mutant_16	T590I_P603S
LEU4_mutant_17	K489E_V573A
LEU4_mutant_18	Y538N
LEU4_mutant_19	Q447R_Q478H_G516D
LEU4_mutant_20	V584E
LEU4_mutant_21	Q439H_D581G
LEU4_mutant_22	R436K_S443Y
LEU4_mutant_23	D564E_T590I
LEU4_mutant_24	T590I

Supplementary Table 6. Occurrence and description of the most relevant mutations found in the Leu4p variants.

Position	Number of occurrences	Variants	Single or multiple mutant variant#	Number of substitutions	Type of substitutions
N515	5	1, 2, 3, 6, 7	Multiple	3	I, D, H
T590	3	16, 23, 24	Single and Multiple	1	I
K51	2	11, 13	Multiple	1	R
Q439	2	9, 21	Multiple	2	R, H
F497	2	2, 11	Multiple	2	L, I
D578	2	8, 15	Multiple	2	N, E
V584	2	12, 20	Single and Multiple	2	A, E
Y485	1	14	Single	1	N
Y538	1	18	Single	1	N
H541	1	5	Single	1	R

Mutations observed in variants with only one mutation (Single), as one of the mutations in variants with multiple mutations (Multiple), or in both types of variants (Single and Multiple).

Supplementary Table 7. Published kinetic parameters of *Bs*_AlsS, *Ec*_IlvC$^{P2D1\text{-}A1}$, and *Ll*_IlvD.

Enzymes	Specific activity (U/mg)	K_m (mM)	k_{cat} (s^{-1})	k_{cat}/K_m	Assay conditions	References
*Bs*_AlsS	8.28	13.6 ± 0.8	121 ± 13	8.9 + 1.1	pH 7.0, 37°C	[24]
*Ec*_IlvC$^{P2D1\text{-}A1}$	n.a.	n.a.	4.3 ± 0.3		pH 7.0, n.a.	[25]
*Ll*_IlvD	0.62 ±0.01*	n.a.	n.a.		n.a.	[26]

* The highest value reported. n.a.: not available

Supplementary Table 8. Amino acid mutations found in the sequenced *Ll*_IlvD variants.

Mutants	Mutations
*Ll*_ilvD_mutant_1	I433V
*Ll*_ilvD_mutant_2	V12A, S189P, H439R
*Ll*_ilvD_mutant_3	K535R
*Ll*_ilvD_mutant_4	K16R
*Ll*_ilvD_mutant_5	E13G, K345M, I514N
*Ll*_ilvD_mutant_6	I154V, I312T

Supplementary Table 9. Oligonucleotides used in this study.

Oligo Name	Sequence	Description
Yfz_Oli31	GCTGGAGCTCACCGGTATACCCGGGAATATGAACCACAGTACATCATATTAAGACGTAGT	P_{LEU1}_Gibson_primer_F
Yfz_Oli32	GAATAATTCTTCACCTTTAGACATGATTTAAAACAGCAAATAATAAAAATCGATAGCGAC	P_{LEU1}_Gibson_primer_R
Yfz_Oli33	CGATTTTTATTATTTGCTGTTTTAAATCATGTCTAAAGGTGAAGAATTATTCACTGGTG	yEGFP_PEST-Gibson_Primer_F
Yfz_Oli34	TCGCTGATCATTACTCGAGGTCGACCTATATTACTTGGGTATTGCCCATACC	yEGFP_PEST-Gibson_Primer_R
Yfz_Oli35	CATGGCTAGCGTTAAAGAGAGTATTATTGC	NheI-ScLEU4$^{1-410}$ Primer-F
Yfz_Oli36	ATAATCCTCGAGGACAGCTTCGTAATCACGGC	XhoI-ScLEU4$^{1-410}$ Primer-R
Yfz_Oli37	CTGAGCGGCCGCTAAAATCATGGCTAGCGTTAAAGAGAGTATTATTGC	NotI-KOZAK-NheI-ScLEU4^{WT} Primer-F
Yfz_Oli38	ATAATCCTCGAGTGCAGAGCCAGATGCCGCAGCATTCTTA	XhoI-ScLEU4^{WT} Primer-R
Yfz_Oli59	TCGACACGCGTTTATTT	Annealed oligo cloning linker SalI_MluI_BsrGI_F
Yfz_Oli60	GTACAAATAAACGCGTG	Annealed oligo cloning linker SalI_MluI_BsrGI_R

Yfz_Oli198	CCGCTAAAATCATGGCTAGC	Error-prone PCR universal_Primer_F for full ORF subcloned into pYZ125
Yfz_Oli242	CATAAATCATAAGAAATTCGCTGATCATTACTCGAG	Error-prone PCR universal_Primer_R for full ORF subcloned into pYZ12s
Yfz_Oli243	GCCGCTTGGGTTATTTTGAGATCT	Error-prone PCR Primer_F for Leu-regulatory domain (Leu430-Ala618, BglII_ScLEU4_XhoI) of ScLEU4
Yfz_Oli345	ATCATGGCTAGCGAATTTAAGTACAACGGTAAGGTC	NheI_*Ll_ilvD*_F
Yfz_Oli346	ATACATCTCGAGTCATTACAAGTCGGTAACACAACCTTCAG	XhoI_*Ll_ilvD*_R
Jla_oli234	GATCGCTAGCCTGAGATCGTTATTGCAAAGC	NheI_ScILV6_F
Jla_oli235	AATTCTCGAGACCAGGTGGTAGTTGGGAAATG	XhoI_ScILV6 _R
Jla_oli276	GAATCGCTAGCGTTAAAGAGAGTATTATTGCTCTTGCTGAGC	NheI_ScLEU4_F
Jla_oli276R	TCATTACTCGAGTGCAGAGCCAGATGCCGCAGCATTCTTA	XhoI_ScLEU4_R
Jla_oli280	CAGAGCATTCTCTAGGTTCTGGTTCTACGCAAGCTGCTTCTTACATCC	LEU4$^{\Delta S547}$_site-directed mutagenesis Primer-F
Jla_oli281	GGATGTAAGAAGCAGCTTGCGTAGAACCAGAACCTAGAGAATGCTCTG	LEU4$^{\Delta S547}$_site-directed mutagenesis Primer-R

Yfz_KO71	CCAGCGTATACAATCTCGATAGTTGGTTTCCCGTTCTTTCCACTCCCGTCtacgctgcaggtcgacaacc	ScGAL80_KO_F
Yfz_KO72	GTTTTTATAACGTTCGCTGCACTGGGGGCCAAGCACAGGGCAAGATGCTTccactagtggatctgatatcacc	ScGAL80_KO_R
Yfz_KO187	AGAAAAAAAAGGATTCTCACACTAGAAGTTTACTGTAGACTTTTTCCTTACAAAAAGACAAGGAACAATCtacgctgcaggtcgacaacc	ScLEU4_KO_F
Yfz_KO188	AGGAAAGGAAGTAAATAAATAAGTATAGAAATAAATAGAAGCGAATAAGTCCTGAAATACAGAAAAGTTCctagtggatctgatatcacc	ScLEU4_KO_R
Yfz_KO189	ACTACATGTTTTCGTTAGAATAAATCACCCTATAAACGCAAAATCAGCTAGAACCTTAGCATACTAAAACtacgctgcaggtcgacaacc	ScBAT1_KO_F
Yfz_KO190	AACAGATCCTCTGAGAGGAATTCTCGTTTTTTTTTTTGGGGGGGGAGGGGATGTTTACCTTCATTATCActagtggatctgatatcacc	ScBAT1_KO_R
Yfz_KO229	TGTTTTCGGCTTATAAGGGTCTTCTCCTTAGGATAATACTATCGGCACATTATCATTTAGCCGCGTAGCCtacgctgcaggtcgacaacc	ScLEU9_KO_F
Yfz_KO230	TTTTCTGTGCCATTTATAAATAAAAATACATATATATATAACATGAGTAATCATAAGCTACTCCTTTCTActagtggatctgatatcacc	ScLEU9_KO_R
Yfz_KO266	ATTGTAGCGCCTGTAATCTTTAGTAACGGATTCTTGTATTTTTTTGTAAACAGCCAAGAAAAAAGTAGAGtacgctgcaggtcgacaacc	ScILV3_KO_F

Yfz_KO267	TGCGAACAAAAAAGATGATGGAAAAGG AGAATCTCTATATATATATTCATCGATTG GGGCCTATAATGCActagtggatctgatatcacc	ScILV3_KO_R
Yfz_KO278	AAGCTCACTAGTAAAGGCGGGAAATAGA ACATTGAGAACGTATTTTGATAtacgctgcagg tcgacaacc	ScTMA29_KO_F
Yfz_KO279	AAAGTCTTACATGTATAAAAAGTATACA GATTTACTTAGTTTAGCTAGGTctagtggatctg atatcacc	ScTMA29_KO_R
Jla_KO1	TATTTTCTACTCATAACCTCACGCAAAAT AACACAGTCAAATCAATCAAAtacgctgcaggt cgacaacc	ScPDC1_KO_F
Jla_KO2	TACATAAAAATGCTTATAAAACTTTAACT AATAATTAGAGATTAAATCGCcactagtggat ctgatatcacc	ScPDC1_KO_R
Jla_KO3	CATAATCAATCTCAAAGAGAACAACACA ATACAATAACAAGAAGAACAAAtacgctgca ggtcgacaacc	ScPDC5_KO_F
Jla_KO4	AAAGTAAAAAAATACACAAACGTTGAAT CATGAGTTTTATGTTAATTAGCcactagtggat ctgatatcacc	ScPDC5_KO_R
Jla_KO5	AGTATAAATAAAAAACCCACGTAATATA GCAAAAACATATTGCCAACAAAtacgctgcag gtcgacaacc	ScPDC6_KO_F
Jla_KO6	TAAGTTTATTTATTTGCAACAATAATTCG TTTGAGTACACTACTAATGGCcactagtggatc tgatatcacc	ScPDC6_KO_R

Jla_KO22	AAAATTTTAGAAATTTAAGGGAAAGCATCTCCACGAGTTTTAAGAACGATtacgctgcaggtcgacaacc	ScBAT2_KO
Jla_KO23	AGTTTTATTCTTTTTAACTTTTAATTACTTTACGTAGCAATAGCGATACTccactagtggatctgatatcacc	ScBAT2_KO
Sag_333	CACCAGAACTTAGTTTCGACGG	TEF-ScILV2_ddPCR_F
Sag_334	GGCAGGTGTGTTGCGG	TEF-ScILV2_ddPCR_R
Sag_341	CCACTCGGCGTACAGCTC	ZeoR_ddPCR_F
Sag_342	GACTTCGTGGAGGACGACTT	ZeoR_ddPCR_R
Sag_347	ATCCTGCGCGTTGACATAA	chrXIV:222kb_ddPCR_F[(Ref.27)]
Sag_348	AGATTCCGTTGCTGGCTATC	chrXIV:222kb_ddPCR_R[(Ref.27)]
Sag_393	GATGTGAGCGTTTGAGTGGTCTTGC	Aro10_ddPCR_F
Sag_394	AACCCTGGTGATGTTGTCGTTTGTG	Aro10_ddPCR_R

Supplementary Figure 1

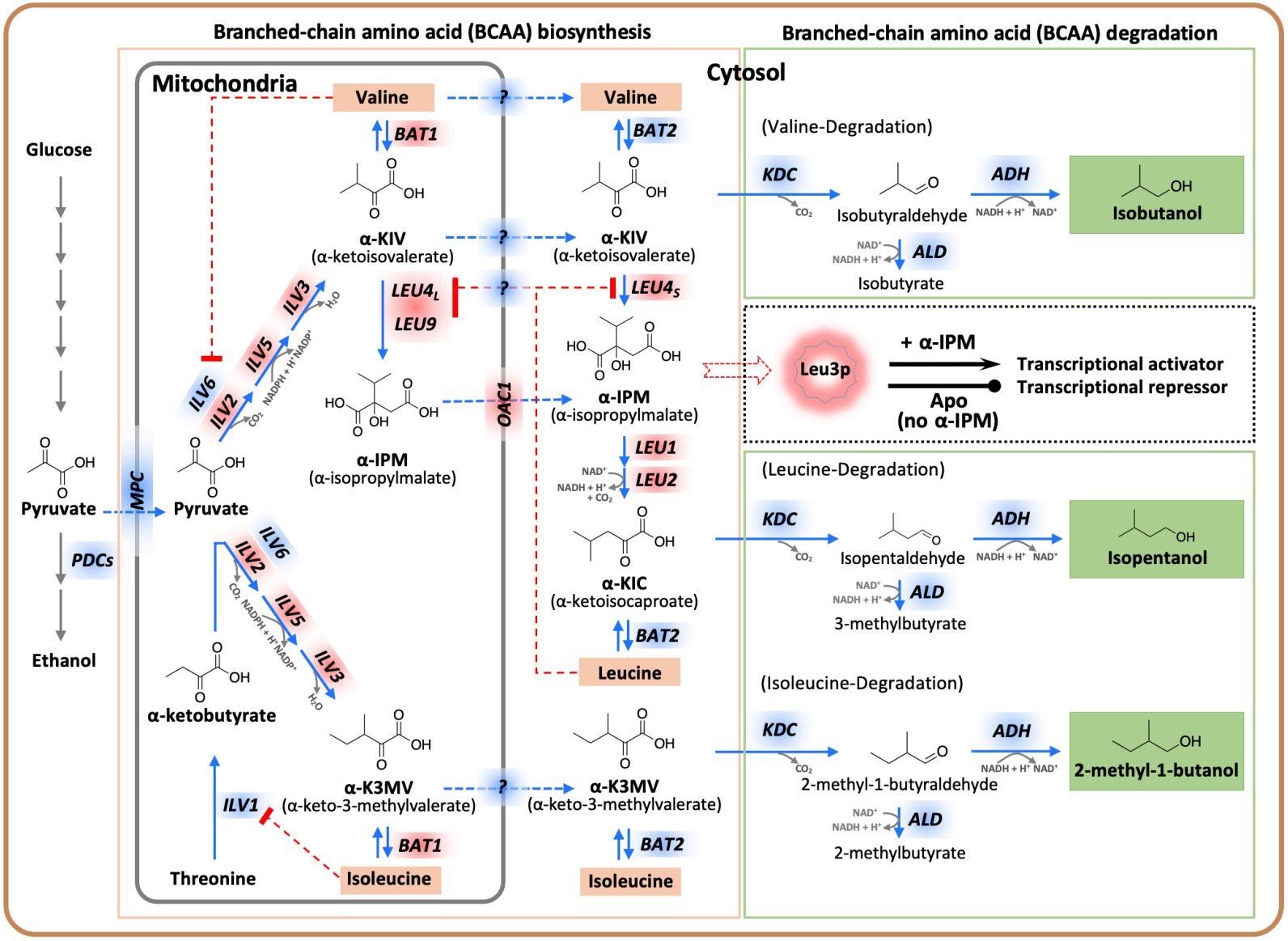

Supplementary Figure 1. Pathways for branched-chain amino acid (BCAA) and branched-chain higher alcohol (BCHA) biosynthesis in *Saccharomyces cerevisiae*. Isobutanol, isopentanol, and 2-methyl-1-butanol biosynthesis are derived from the biosynthesis and degradation of valine, leucine, and isoleucine, respectively. The upstream pathway for isobutanol production (valine biosynthesis) consists of three enzymes natively localized in mitochondria (orange rectangle): acetolactate synthase (ALS, encoded by *ILV2*), ketol-acid reductoisomerase (KARI, encoded by *ILV5*), and dehydroxyacid dehydratase (DHAD, encoded by *ILV3*)[28]. Ilv2p, Ilv3p, and Ilv5p convert two molecules of pyruvate to the valine precursor α-ketoisovalerate (α-KIV), which is exported to the cytosol by one or more unknown α-KIV carrier(s). The native localization of the Ehrlich valine degradation occurs in the cytosol, where α-KIV is converted to isobutanol through the Ehrlich BCAA degradation pathway[29] (green rectangle), comprised of α-ketoacid decarboxylases (α-KDCs) and alcohol dehydrogenases (ADHs). The conversion between α-KIV and valine is catalyzed by mitochondrial and cytosolic branched-chain amino acid aminotransferases (encoded by *BAT1* and *BAT2,* respectively). In the upstream pathway for isopentanol production (leucine biosynthesis), α-KIV is converted to α-isopropylmalate (α-IPM) by α-IPM synthases located in mitochondria (encoded by the short $LEU4_S$ and *LEU9*) and the cytosol (encoded by the long $LEU4_L$). Subsequently, α-IPM is converted in the cytosol to β-IPM by isopropylmalate isomerase (encoded by *LEU1*) and then to α-ketoisocaproate (α-KIC) by β-IPM dehydrogenase (encoded by *LEU2*). This α-KIC precursor is then converted to leucine by Bat2p. Alternatively, α-KIC is converted to isopentanol in the cytosol via the BCAA Ehrlich degradation pathway[29]. The upstream pathway for 2-methyl-1-butanol (isoleucine biosynthesis) consists of the same mitochondrial enzymes involved in valine and leucine biosynthesis, Ilv2p, Ilv5p, and Ilv3p; except that for isoleucine biosynthesis, Ilv2p catalyzes the condensation of one pyruvate and one α-ketobutyrate, produced by threonine deaminase (encoded by *ILV1*), instead of two pyruvate molecules as in the biosynthesis of valine and leucine. The subsequent reactions catalyzed by Ilv5p and Ilv3p result in the production of the isoleucine precursor α-keto-3-methylvalerate (α-K3MV), which is transaminated to isoleucine in the mitochondria and the cytosol by Bat1p and Bat2p, respectively. Alternatively, α-K3MV is converted to 2-methyl-1-butanol through the Ehrlich BCAA degradation pathway (green rectangle) in the cytosol. The enzymatic activities of Ilv6p, Leu4p/Leu9p, and Ilv1p are negatively regulated by valine, leucine, and isoleucine, respectively, as indicated with red dashed lines. Leu3p, a dual-function transcriptional regulator, regulates genes (highlighted in red) involved in BCAA biosynthesis. It acts as a transcriptional activator in the presence of α-isopropylmalate (α-IPM) and a repressor in its absence. Genes not known to be regulated by Leu3p are labeled in blue. The blue rectangle denotes the cell plasma membrane. *PDC*s: pyruvate decarboxylase isozymes; *MPC*: mitochondrial pyruvate carriers; *OAC1*: mitochondrial α-IPM transporter; *ALD*: aldehyde dehydrogenase.

Supplementary Figure 2

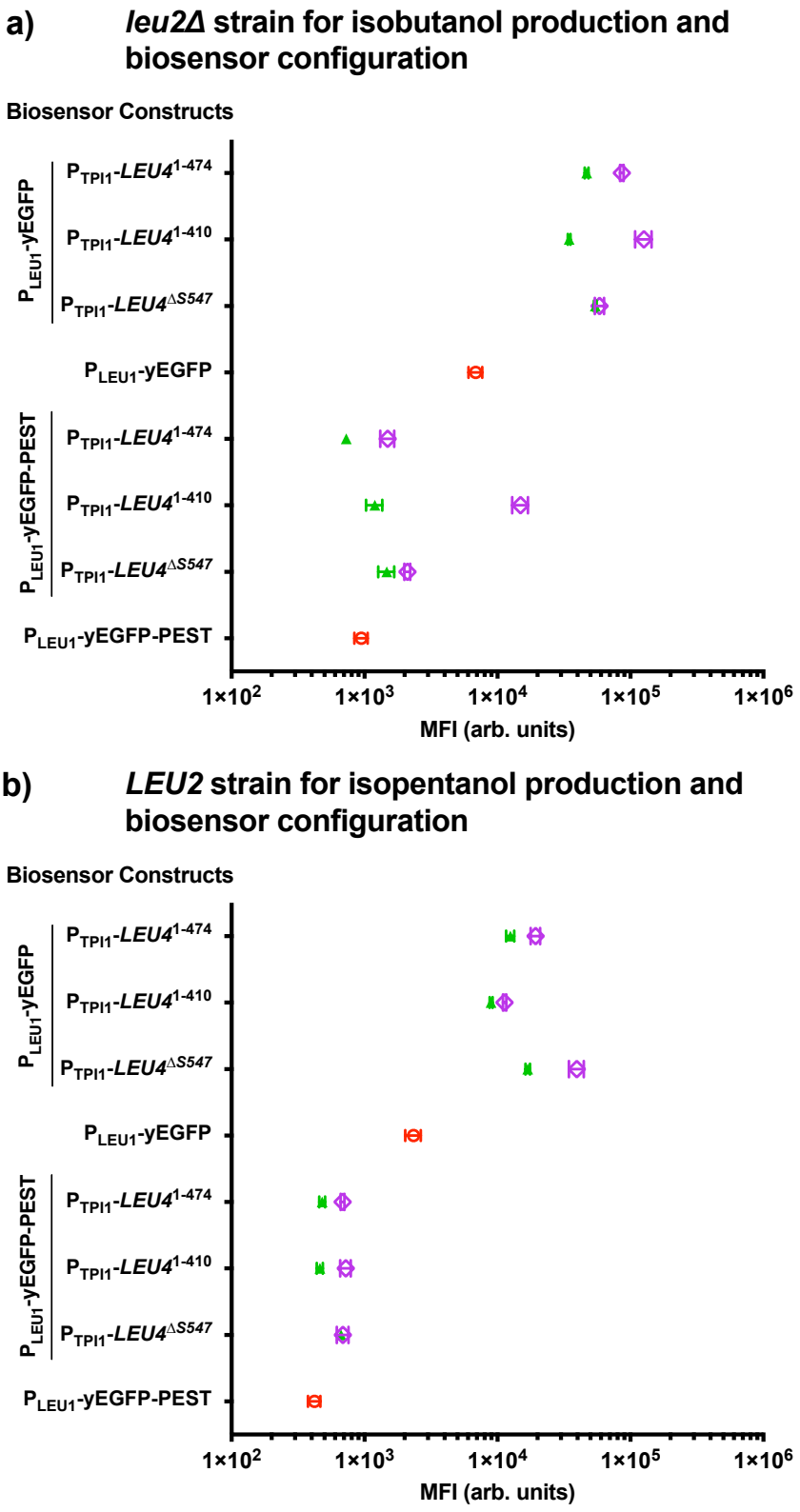

Supplementary Figure 2. GFP median fluorescence intensity (MFI) of different biosensor constructs. Biosensor MFI was measured in a *leu2*Δ strain (a) to develop a biosensor configuration specific to isobutanol and in a *LEU2* strain (b) to develop a biosensor configuration specific to isopentanol. The BCHA biosensor is off (red circles) when only P_{LEU1}-yEGFP-PEST-T_{ADH1} or P_{LEU1}-yEGFP-T_{ADH1} are introduced because the endogenous α-IPM synthase (Leu4p) is inhibited by leucine. The BCHA biosensor constructs can be turned on (green triangles) when a leucine-insensitive Leu4 variant (*LEU4*$^{\Delta S547}$, *LEU4*$^{1\text{-}410}$, or *LEU4*$^{1\text{-}474}$) is additionally introduced. For each Leu4p mutant, the MFI is reported for constructs with and without a PEST tag fused to yEGFP. The MFI increases when the BCHA biosynthesis pathway (*ILV2, ILV3, ILV5*, KDC, and ADH) is overexpressed in strains harboring different biosensor constructs (purple diamonds). MFI are represented in arbitrary units (arb. units). All data are shown as mean values. Error bars represent the standard deviation of at least three biological replicates. Source data are provided as a Source Data file.

Supplementary Figure 3

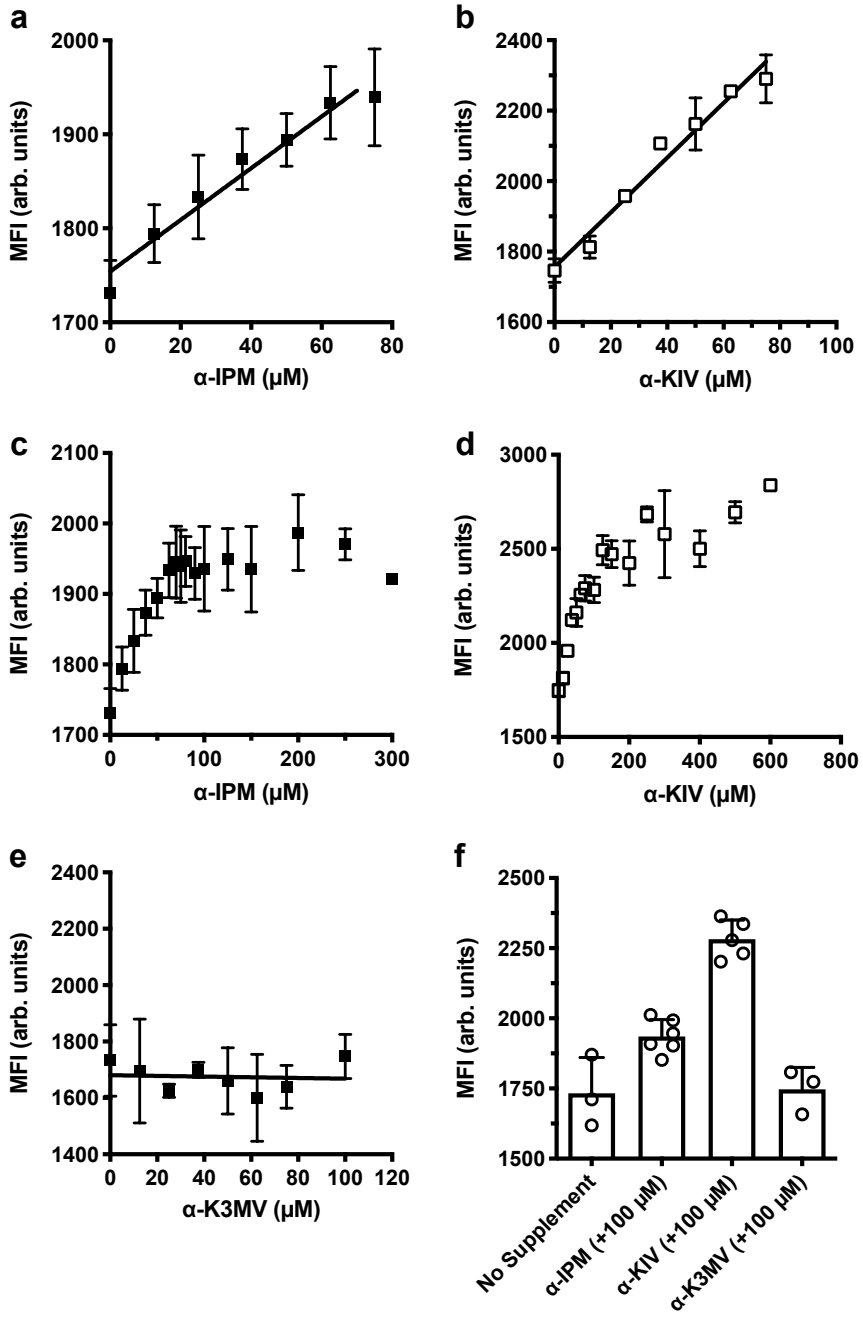

Supplementary Figure 3. Response of the biosensor in its isobutanol configuration to isopropylmalate (α-IPM), α-ketoisovalerate (α-KIV), and α-keto-3-methylvalerate (α-K3MV). The biosensor responds linearly to increasing concentrations of α-IPM (**a**) and α-KIV (**b**) supplemented in the media up to 80 μM. Biosensor response to higher concentrations of **(c)** α-IPM, **(d)** α-KIV, or **(e)** α-K3MV supplemented in the media. **f)** Side-by-side comparison of the biosensor response to 100 μM of α-IPM, α-KIV, and α-K3MV supplemented in the media. Median fluorescence intensity (MFI) are represented in arbitrary units (arb. units). All data are shown as mean values. Error bars represent the standard deviation of at least three biological replicates. Source data are provided as a Source Data file.

Supplementary Figure 4

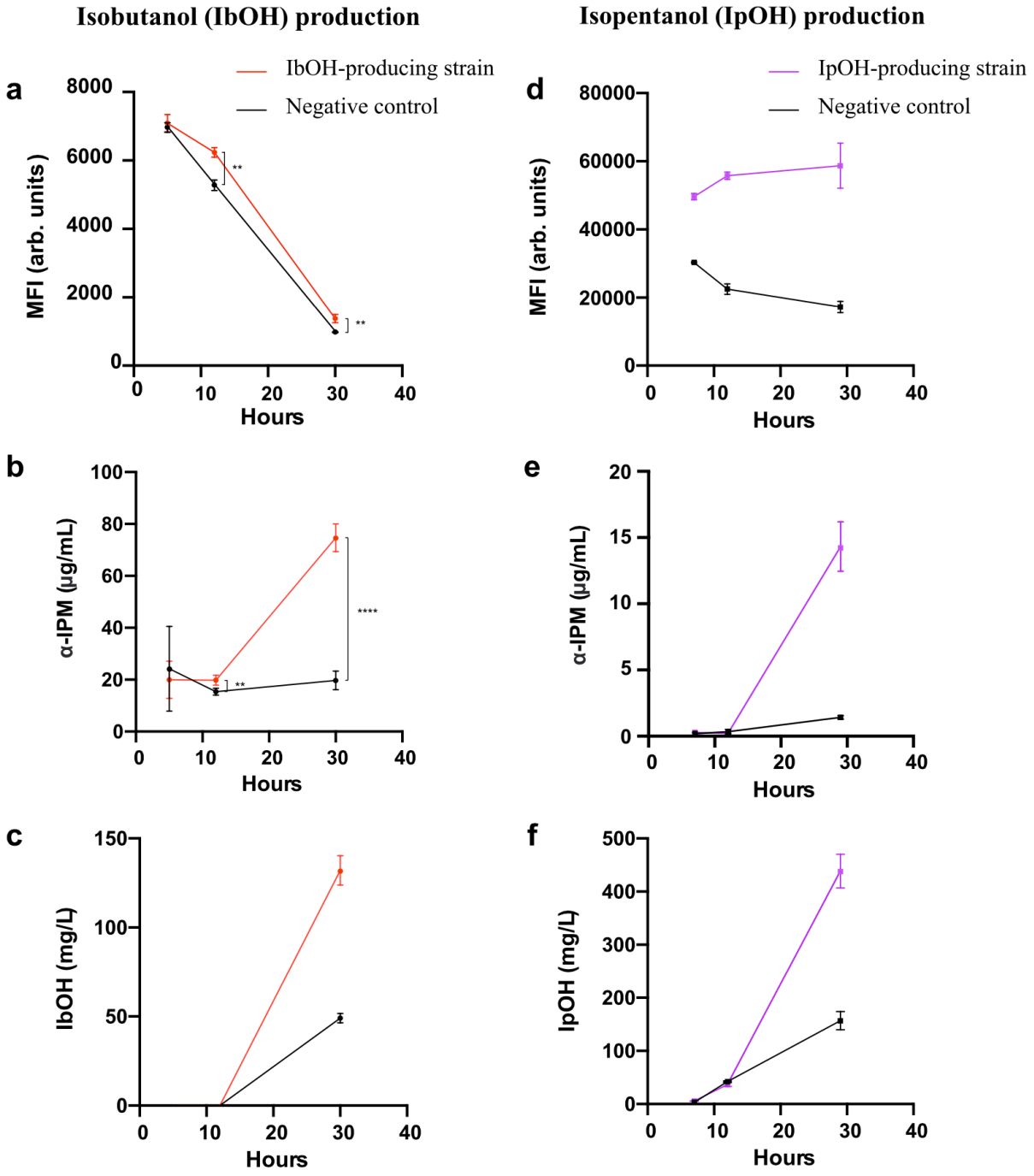

Supplementary Figure 4. Correlations of biosensor response to intracellular alpha-isopropylmalate (α-IPM) concentrations, and BCHA production in low-cell density fermentations. (a) Median fluorescent intensity (MFI) measured throughout a low-cell density fermentation with an isobutanol-producing strain (red, YZy235) and a negative control strain (black, YZy121), both carrying the isobutanol-configured biosensor. **(b)** Intracellular α-IPM

concentrations measured during the low-cell-density fermentations for both the isobutanol producer and control strains. A two-sided *t*-test was used to determine the statistical significance of the differences in MFI measurements and α-IPM concentrations in the low- and high-producers; From left to right in Supplementary Figure 4a: P=0.0014, P=0.0046; From left to right in Supplementary Figure 4b: P=0.001, P<0.000001; ** $P \leq 0.01$ **** $P \leq 0.0001$. **(c)** Isobutanol production of the isobutanol-producer and control strains. No detectable measurements at 5h and 12h. **(d)** MFI measured throughout a low-cell-density isopentanol fermentation in an isopentanol-producing strain (purple, SHy159) and a negative control strain (black, SHy187), both containing the isopentanol-configured biosensor. **(e)** Intracellular α-IPM concentrations measured during the low-cell-density fermentations for both the isopentanol producer and control strains. **(f)** Isopentanol production of isopentanol-producer and control strains. MFI are represented in arbitrary units (arb. units). All data are shown as mean values. Error bars represent the standard deviation of at least three biological replicates. Source data are provided as a Source Data file.

Supplementary Figure 5

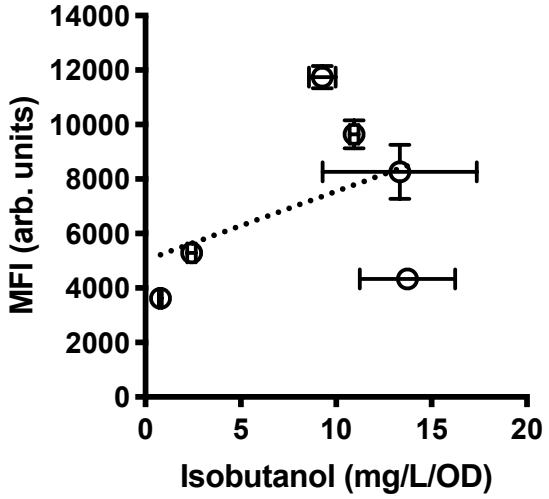

Supplementary Figure 5. Correlation between specific isobutanol titers and GFP fluorescence signals from the isopentanol configuration of the biosensor in the *LEU2* strains engineered for isopentanol production. Strains used from left to right: SHy187, SHy192, SHy158, SHy176, SHy159, and SHy188 (Supplementary Table 1). The median fluorescence intensity (MFI) for each strain was measured after 13h of growth and plotted with the corresponding specific isobutanol titers obtained after 48h high-cell-density fermentations. The dotted line shows a poor linear regression fit with an R^2 of 0.19. MFI are represented in arbitrary units (arb. units). All data are shown as mean values. Error bars represent the standard deviation of at least three biological replicates. Source data are provided as a Source Data file.

Supplementary Figure 6

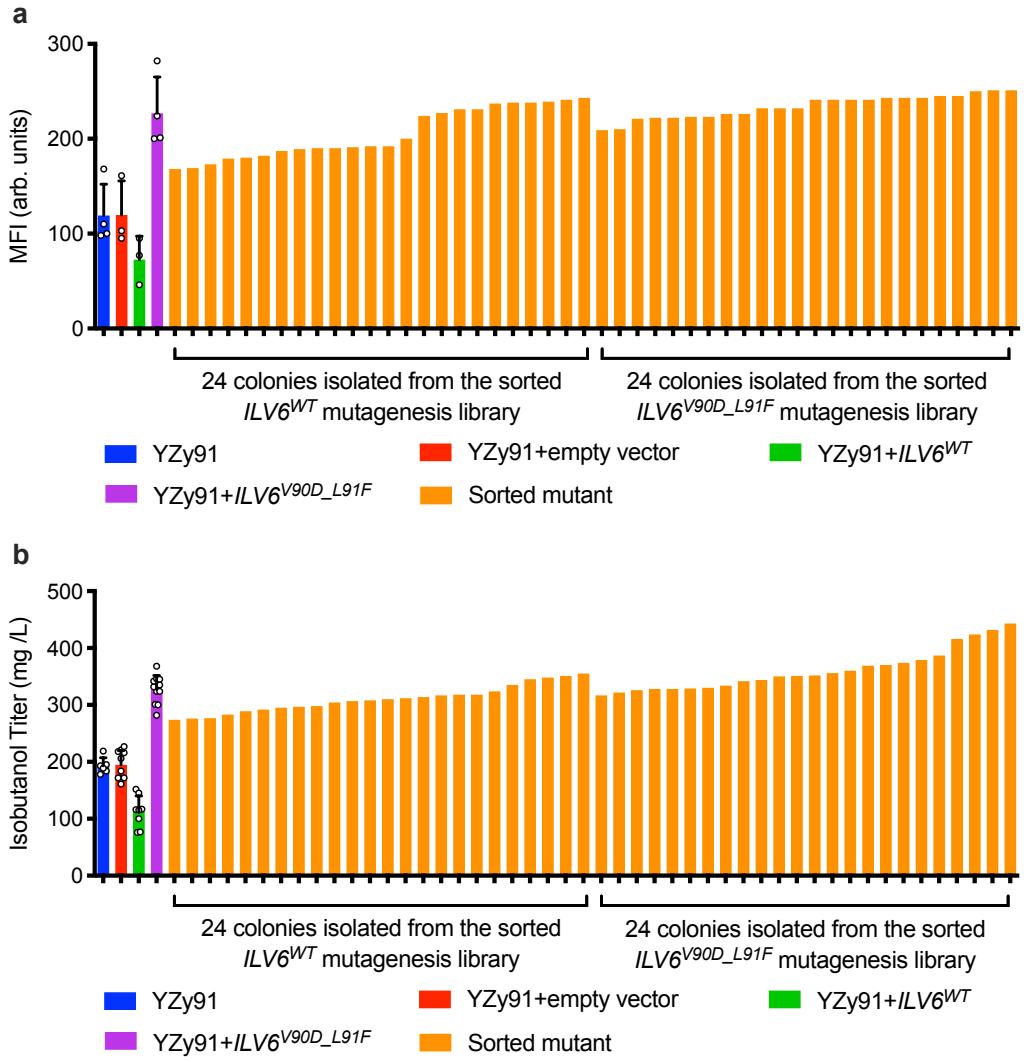

Supplementary Figure 6. Screen of 48 random colonies sorted from mutagenesis libraries of the wild-type *ILV6* and valine-insensitive *ILV6^{V90D_L91F}* mutant. (**a**) Flow cytometry measurements of the GFP median fluorescence intensity (MFI) of 48 sorted strains (orange) measured after 13h of growth in media containing four times more valine (2.4 mM) than the usual synthetic defined medium (24 colonies were isolated from the sorted wild-type *ILV6* mutagenesis library, and 24 colonies were isolated from the sorted *ILV6^{V90D_L91F}* mutagenesis library). MFI of the basal strain YZy91 (*ilv6Δ bat1Δ bat2Δ*) with (red) or without (blue) an empty vector, or transformed with plasmids containing *ILV6^{WT}* (green) or *ILV6^{V90D_L91F}* (purple), are shown as controls. (**b**) Isobutanol titers after 48h fermentations with the same 48 sorted strains (orange) and controls (red, blue, purple, and green) shown in (**a**). MFI are represented in arbitrary units (arb. units). All data except the data of sorted mutant are shown as mean values. Open circles represent individual data points. Error bars of the control strains represent the standard deviation of at least three biological replicates. Source data are provided as a Source Data file.

Supplementary Figure 7

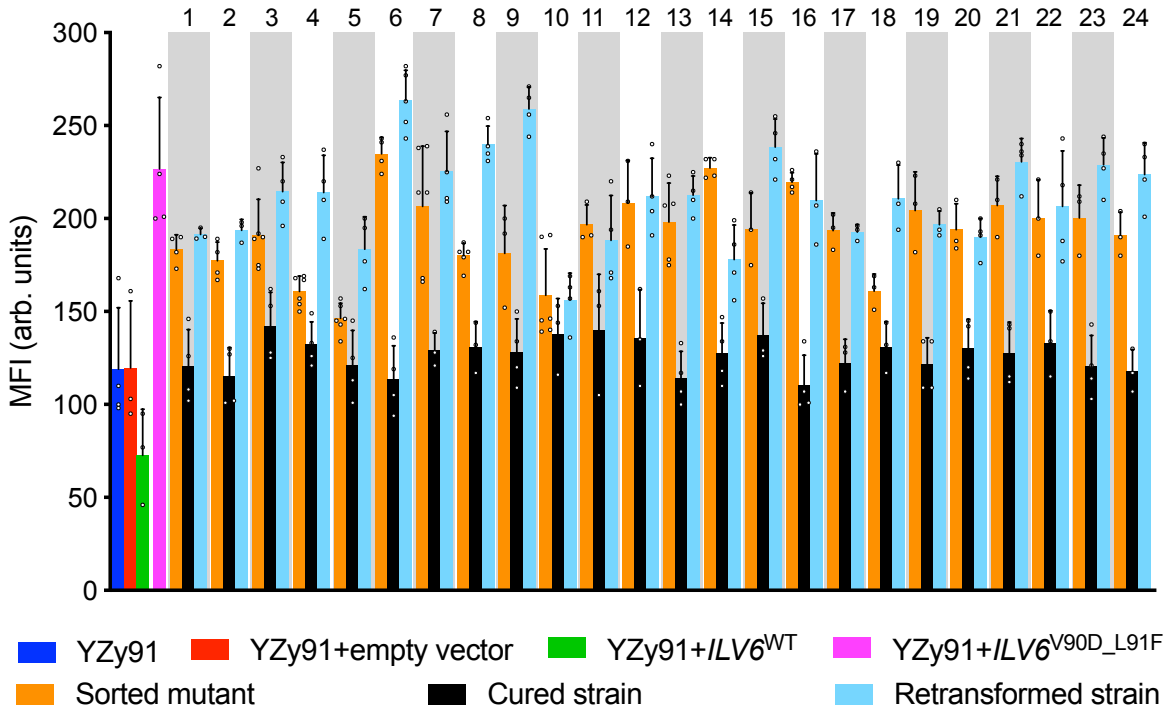

Supplementary Figure 7. Confirmation that isolated *ILV6* variants with unique sequences enhance GFP fluorescence signal from the isobutanol-configured biosensor. Flow cytometry measurements of the GFP median fluorescence intensity (MFI) of sorted strains with unique *ILV6* sequences (orange), plasmid-cured derivatives (black), and strains obtained from retransforming YZy91 with each unique plasmid isolated from the corresponding sorted strains (cyan), measured after 13h of growth in media containing four times more valine (2.4 mM) than the usual synthetic defined medium. GFP fluorescence measured with the basal strain YZy91 (*ilv6Δ bat1Δ bat2Δ*) with (red) or without (blue) an empty vector, or transformed with plasmids containing wild-type *ILV6* (*ILV6*^{WT}, green), or *ILV6*$^{V90D\_L91F}$ (magenta), are shown as controls. The numbers on the upper x-axis identify each of the strains harboring screened mutants with unique *ILV6* sequences. *ILV6* mutants 1 – 10 were isolated from the sorted *ILV6*^{WT} mutagenesis library. *ILV6* mutants 11 – 24 were isolated from the sorted *ILV6*$^{V90D\_L91F}$ mutagenesis library. MFI are represented in arbitrary units (arb. units). All data are shown as mean values. Open circles represent individual data points. Error bars represent the standard deviation of three biological replicates. Source data are provided as a Source Data file.

Supplementary Figure 8

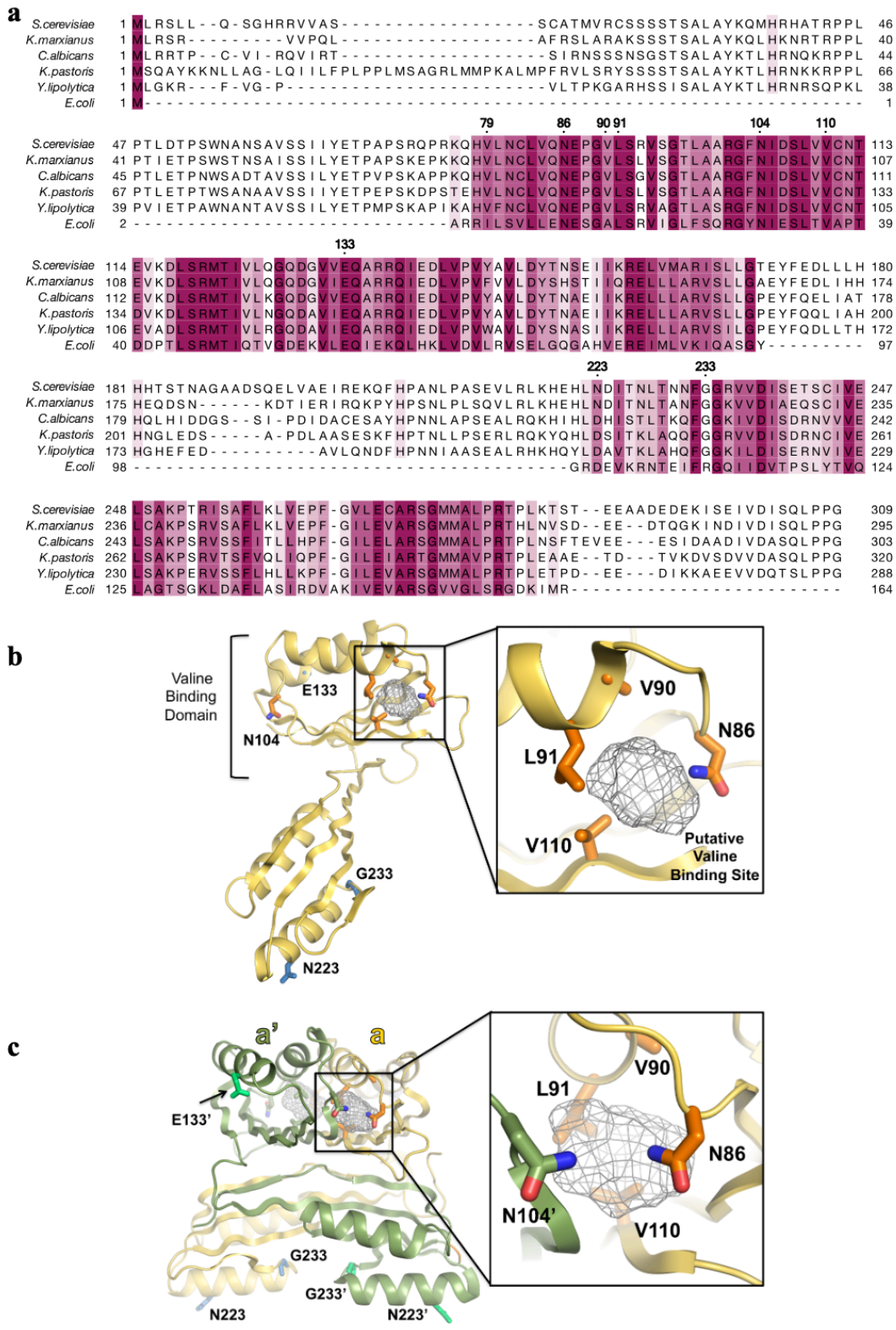

Supplementary Figure 8. Sequence and structural analysis of yeast Ilv6p and its isolated mutants. (**a**) Alignment of the amino acid sequence of *E.coli* IlvH (acetohydroxyacid synthase regulatory subunit) with Ilv6p sequences from *Saccharomyces cerevisiae*, *Kluyveromyces marxianus*, *Candida albicans*, *Komagataella pastoris*, and *Yarrowia lipolytica*. The color intensity reflects the level of conservation of each residue. Key residues mutated in *ILV6*, derived from the *ILV6* wild-type mutagenesis library (Supplementary Table 3), that enhance isobutanol production and whose positions are present in *E.coli* IlvH (N86, V90, L91, N104, V110, N223, E133, and G233) are labeled on the top of the alignment (most of them are highly conserved except G233). (**b, c**) Key substituted residues above mapped onto the crystal structure of the regulatory subunit of acetohydroxyacid synthase, IlvH, from *E. coli* (pdb code: 2f1f), shown on the structure of the monomer (**b**), and from a different angle on the structure of the dimer (**c**). Close-up views of the putative valine-binding sites (gray mesh) and the key residues that make them are shown in the side-boxes.

Supplementary Figure 9

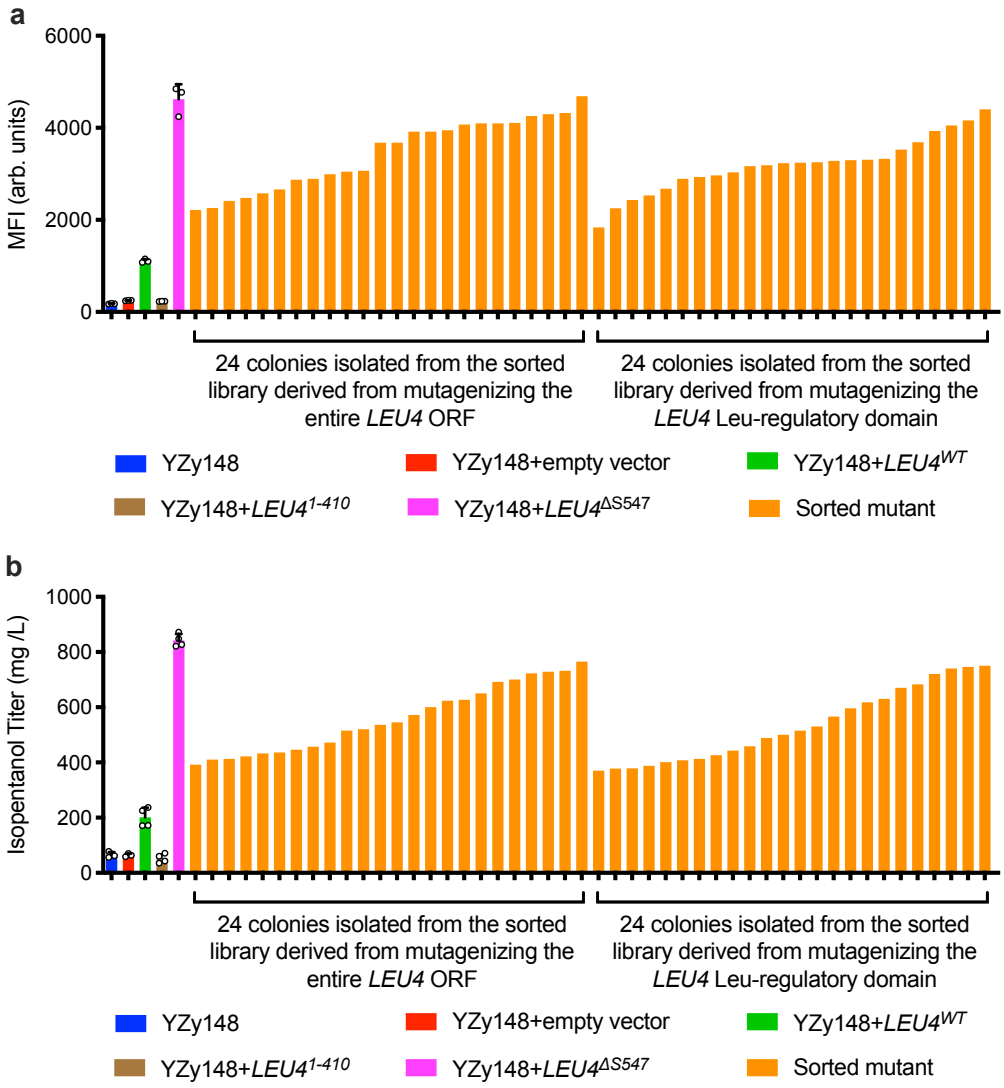

Supplementary Figure 9. Screen of 48 random colonies sorted from libraries derived from mutagenizing the entire *LEU4* ORF or the *LEU4* regulatory domain. (**a**) Flow cytometry measurements of the GFP median fluorescence intensity (MFI) of 48 sorted strains (orange) measured after 13 h of growth in SC-Ura media supplemented with 2% glucose (24 colonies are isolated from the sorted library derived from mutagenizing the entire *LEU4* ORF, and 24 colonies are isolated from the sorted library derived from mutagenizing the *LEU4* regulatory domain). MFI of the basal strain YZy148 (*leu4Δ leu9Δ bat1Δ LEU2*) with (red) or without (blue) an empty vector, or transformed with plasmids containing wild-type *LEU4* ($LEU4^{WT}$, green), $LEU4^{1\text{-}410}$ (brown), or $LEU4^{\Delta S547}$ (magenta), are shown as controls. (**b**) Isopentanol titers after 48h fermentations with the same 48 sorted strains (orange) and controls (red, blue, green, brown, and magenta) shown in (**a**). MFI are represented in arbitrary units (arb. units). All data except the data of sorted mutant are shown as mean values. Open circles represent individual data points. Error bars of the control strains represent the standard deviation of at least three biological replicates. Source data are provided as a Source Data file.

Supplementary Figure 10

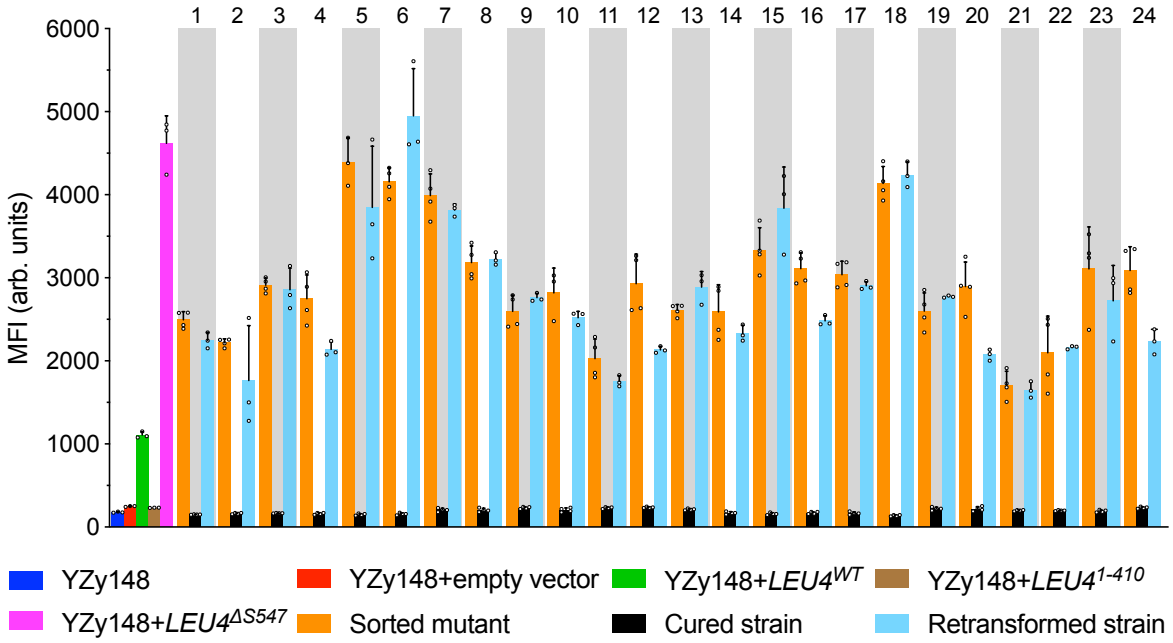

Supplementary Figure 10. Confirmation that isolated *LEU4* variants with unique sequences enhance GFP fluorescence signal from the isopentanol-configured biosensor. Flow cytometry measurements of the GFP median fluorescence intensity (MFI) of sorted strains with unique *LEU4* sequences (orange), plasmid-cured derivatives (black), and strains obtained from retransforming YZy148 with each unique plasmid isolated from the corresponding sorted strains (cyan), measured after 13 h of growth in SC-Ura media supplemented with 2% glucose. GFP fluorescence intensity of the basal strain YZy148 (*leu4Δ leu9Δ bat1Δ LEU2*) with (red) or without (blue) an empty vector, or transformed with plasmids containing wild-type *LEU4* ($LEU4^{WT}$, green), $LEU4^{1\text{-}410}$ (brown), or $LEU4^{\Delta S547}$ (magenta), are shown as controls. The numbers on the upper x-axis identify each of the strains harboring screened mutants with unique *LEU4* sequences. *LEU4* mutants 1–13 were isolated from the sorted library derived from mutagenizing the entire *LEU4* ORF. *LEU4* mutants 14–24 were isolated from the sorted library derived from mutagenizing the *LEU4* leucine regulatory domain. MFI are represented in arbitrary units (arb. units). All data are shown as mean values. Open circles represent individual data points. Error bars represent the standard deviation of three biological replicates. Source data are provided as a Source Data file.

Supplementary Figure 11

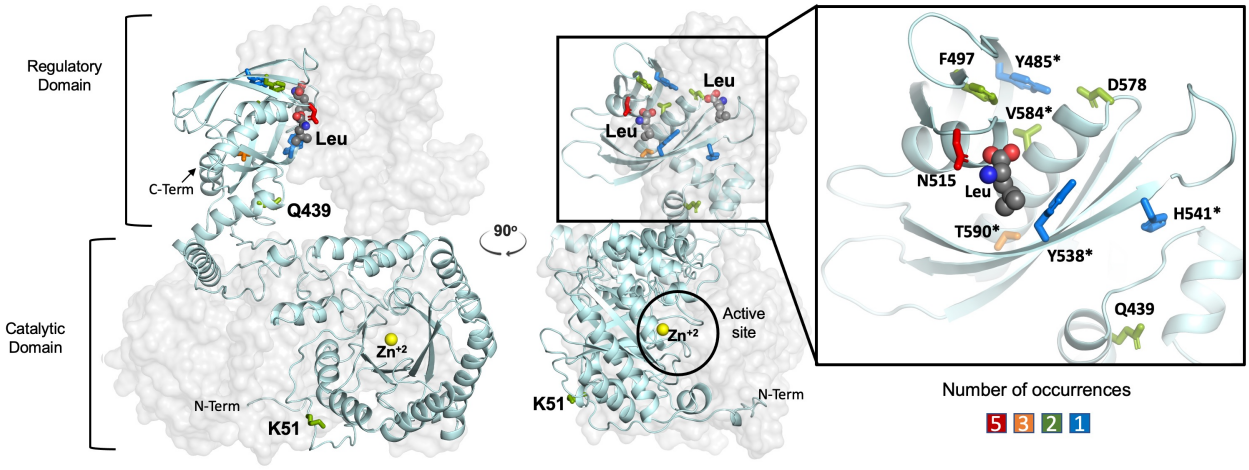

Supplementary Figure 11. Structural analysis of key residues mutated in isolated Leu4p variants. Key residues found to be mutated in Leu4p variants that enhance isopentanol production mapped onto the crystal structure of LeuA from *Mycobacterium tuberculosis* (pdb code: 3fig). The catalytic and regulatory domains of the LeuA dimer are depicted (left panel). One of the two monomers is represented as a cartoon (light blue) and the other one as a surface (gray). A close-up view of the occupied leucine binding site of the regulatory domain (right panel box) shows the orientation of key residues (shown in sticks) found to be mutated in isolated *LEU4* variants that enhance isopentanol production. Residues labeled with an asterisk (*) are those mutated in variants containing only one mutation (see Supplementary Table 5). The number of unique sequences in which each residue is found mutated is depicted by a color scale shown in the bottom right corner (see Supplementary Tables 4, 5). Leucine bound to the regulatory binding site and a zinc ion are show in spheres.

Supplementary Figure 12

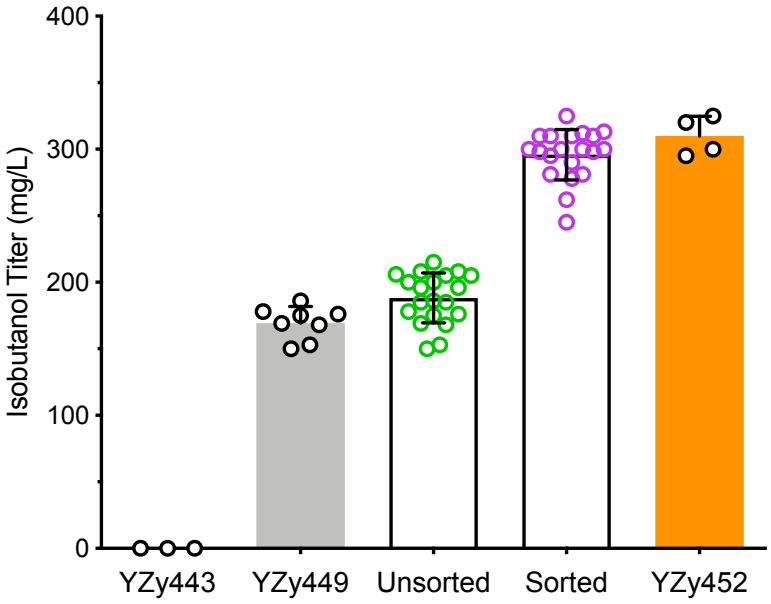

Supplementary Figure 12. High-throughput screens, enabled by the isobutanol configuration of the biosensor, to identify strains carrying extra copies of *Ec_ilvC*$^{P2D1\text{-}A1}$ with enhanced isobutanol production from galactose. Isobutanol production of the parent strain (YZy443), the baseline strain containing a single copy of a genomically integrated galactose-inducible isobutanol cytosolic pathway (YZy449), 20 random colonies from each the unsorted population (unsorted) and sorted population (sorted) of YZy449 transformed with extra copies of *Ec_ilvC*$^{P2D1\text{-}A1}$ randomly integrated into δ-sites, and the best sorted strain (YZy452). Measurements were made after 48h fermentations in 15% galactose. All data are shown as mean values. Open circles represent individual data points. Error bars represent the standard deviation of at least three biological replicates (for YZy443, YZy449 and YZy452) or 20 random colonies (from unsorted and sorted populations). Source data are provided as a Source Data file.

Supplementary Figure 13

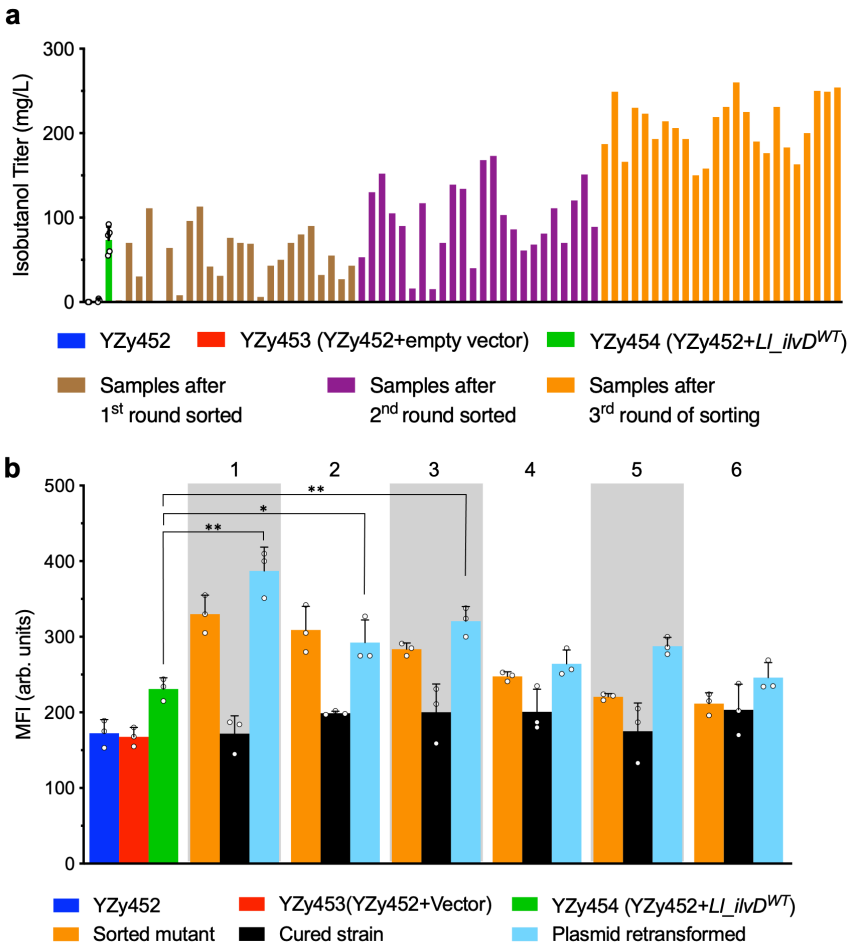

Supplementary Figure 13. High-throughput screens for *Ll_ilvD* variants with enhanced cytosolic isobutanol production from glucose using the isobutanol configuration of the biosensor. (**a**) Isobutanol titers of 24 colonies randomly picked after each round of FACS. Titers obtained with the basal strain YZy452 (containing the cytosolic isobutanol pathway with extra copies of *Ec_ilvC*$^{P2D1\text{-}A1}$ and galactose-inducible *Ll_ilvD*) with (red) or without (blue) an empty vector, or transformed with a plasmid containing wild-type *Ll_ilvD* (*Ll_ilvD*^{WT}, green) are shown as controls. (**b**) Confirmation that isolated *Ll_ilvD* variants with unique sequences enhance GFP fluorescence signal from the isobutanol-configured biosensor. Flow cytometry measurements of the GFP median fluorescence intensity (MFI), taken after 13h of growth in 2% glucose, for sorted strains (orange), plasmid-cured derivatives (black), and basal strain (YZy452) retransformed with each unique plasmid isolated from the corresponding sorted strains (cyan). Fluorescence of the basal strain YZy452 with (red) or without (blue) an empty vector, or transformed with a plasmid containing *Ll_ilvD*^{WT} (green) are shown as controls. The numbers on the upper x-axis identify each of the strains harboring unique *Ll_ilvD* variants. MFI are represented in arbitrary units (arb. units). Except the data of 24 colonies randomly picked after each round of FACS, all data are shown as mean values. Open circles represent individual data points. Error bars represent the standard deviation of three biological replicates. A two-sided *t*-test was used to determine the statistical significance of the difference between MFI of YZy452 transformed with a plasmid containing

Ll_ilvD^{WT} (green), or *Ll_ilvD* mutant #1 (*Ll_ilvD*^{I433V}), or mutant #2 (*Ll_ilvD*$^{V12A, S189P, H439R}$), or mutant #3 (*Ll_ilvD*^{K535R}). From left to right: P=0.0015, P=0.0336, P=0.003; * $P \leq 0.05$, ** $P \leq 0.01$. Source data are provided as a Source Data file.

Supplementary Figure 14

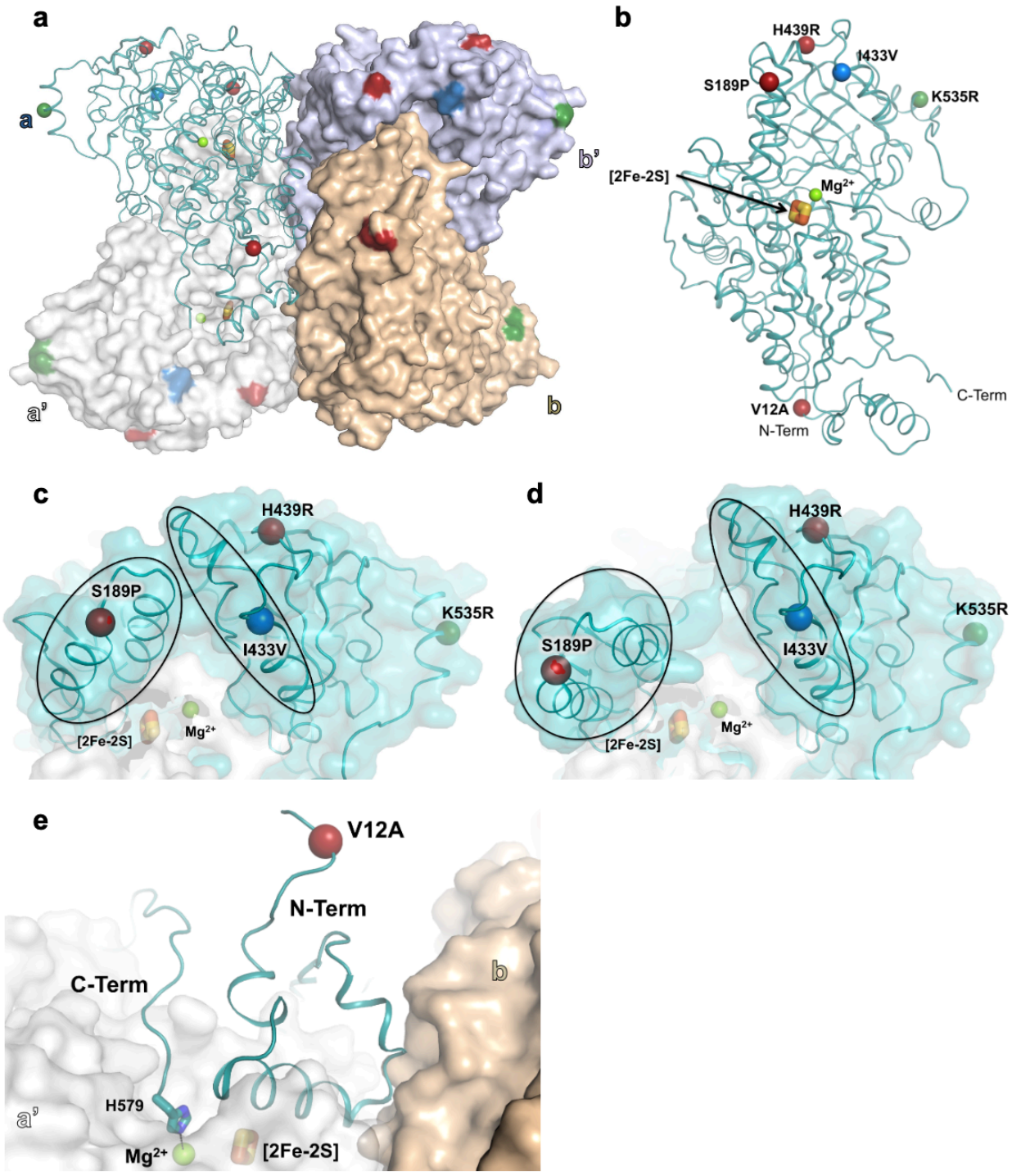

Supplementary Figure 14. Structural analysis of key residues mutated in isolated IlvD variants. Key residues found to be mutated in *Ll*_IlvD variants that enhance cytosolic isobutanol production mapped onto the crystal structure of its homolog l-arabinonate dehydratase from *Rhizobium leguminosarum bv. trifolii* (pdb code: 5j84). The colored spheres indicate the locations

of the mutated residues found in *Ll*_IlvD mutants #1 (blue), #2 (red) and #3 (green), (see Supplementary Table 8) (**a**) Tetramer of l-arabinonate dehydratase, a homolog of *Ll*_IlvD with 31.56% sequence identity and 36% sequence similarity. Residues substituted in *Ll*_IlvD mutants #1 (blue), #2 (red), and #3 (green) are shown as spheres on one of the four monomers represented as a ribbon (light blue), and colored on the surface representations (light blue, wheat, gray) of the other three monomers. (**b**) Ribbon representation of an *Ll*_IlvD monomer showing the positions of mutated residues (spheres) found in *Ll*_IlvD mutants #1 (blue), #2 (red), and #3 (green), relative to the 2Fe-2S cluster (orange and yellow sticks) and the Mg^{2+} ion (bright green sphere) bound to the active site. (**c, d**) Close-up views of the closed (**c**) and open (**d**) conformations of the enzyme (pdb code: 5j84 and pdb code: 5j85, respectively). Residues S189 (substituted in mutant #2) and I433 (substituted in mutant #1), are located in the lobes (circled in black) that open and close to grant access or protect to the active site. (**e**) A close-up view shows the packing between the N- and C-termini of a monomer, which potentially contributes to the positioning of the His-579 that coordinates the Mg^{2+} in the active site (found in a different monomer).

Supplementary Figure 15

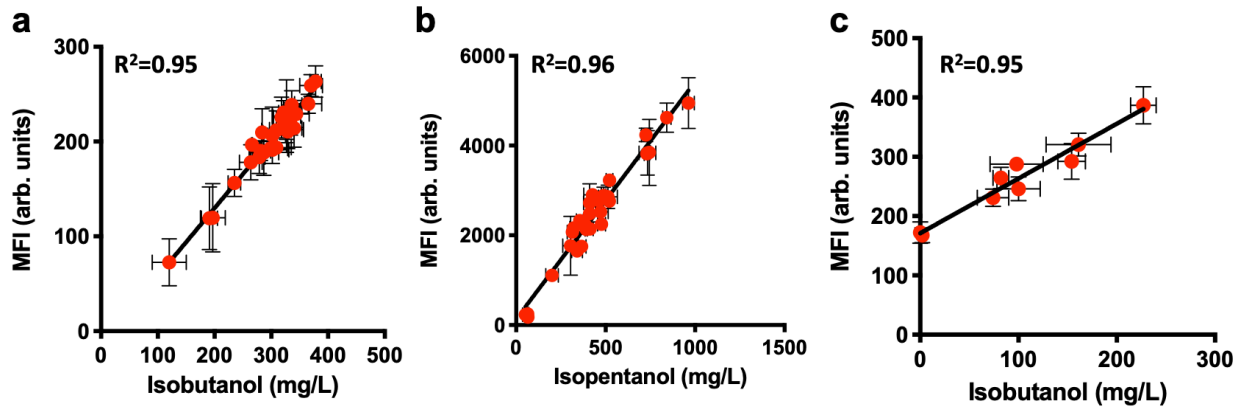

Supplementary Figure 15. Correlation between BCHAs titers and GFP fluorescence signals from the isobutanol or isopentanol configurations of the biosensor in strains screened during three applications. (a) The strains obtained by retransforming YZy91 with an empty vector, or plasmids containing $ILV6^{WT}$, $ILV6^{V90D\_L91F}$, or each unique *ILV6* variant isolated from three rounds of FACS of *ILV6* mutagenized libraries **(**Fig. 3b**)** using the butanol configuration of the biosensor**. (b)** The strains obtained by retransforming YZy148 with an empty vector, or plasmids containing $LEU4^{WT}$ or each unique *LEU4* variant isolated from three rounds of FACS of *LEU4* mutagenized libraries **(**Fig. 4c**)** using the isopentanol configuration of the biosensor. **(c)** The strains obtained by retransforming YZy452 with an empty vector, or plasmids containing Ll_ilvD^{WT}, or each unique *Ll_ilvD* variant isolated from three rounds of FACS of *Ll_ilvD* mutagenized libraries (Fig. 5b**)** using the butanol configuration of the biosensor. The GFP median fluorescence intensity (MFI) for each strain was measured after 13h of growth and plotted with the corresponding BCHA titers obtained after 48h high-cell-density fermentations. The solid lines show strong linear regression fits with R^2 values of 0.95, 0.96, 0.95 in figures (a), (b) and (c), respectively. MFI are represented in arbitrary units (arb. units). All data are shown as mean values. Error bars represent the standard deviation of at least three biological replicates. Source data are provided as a Source Data file.

Supplementary Figure 16

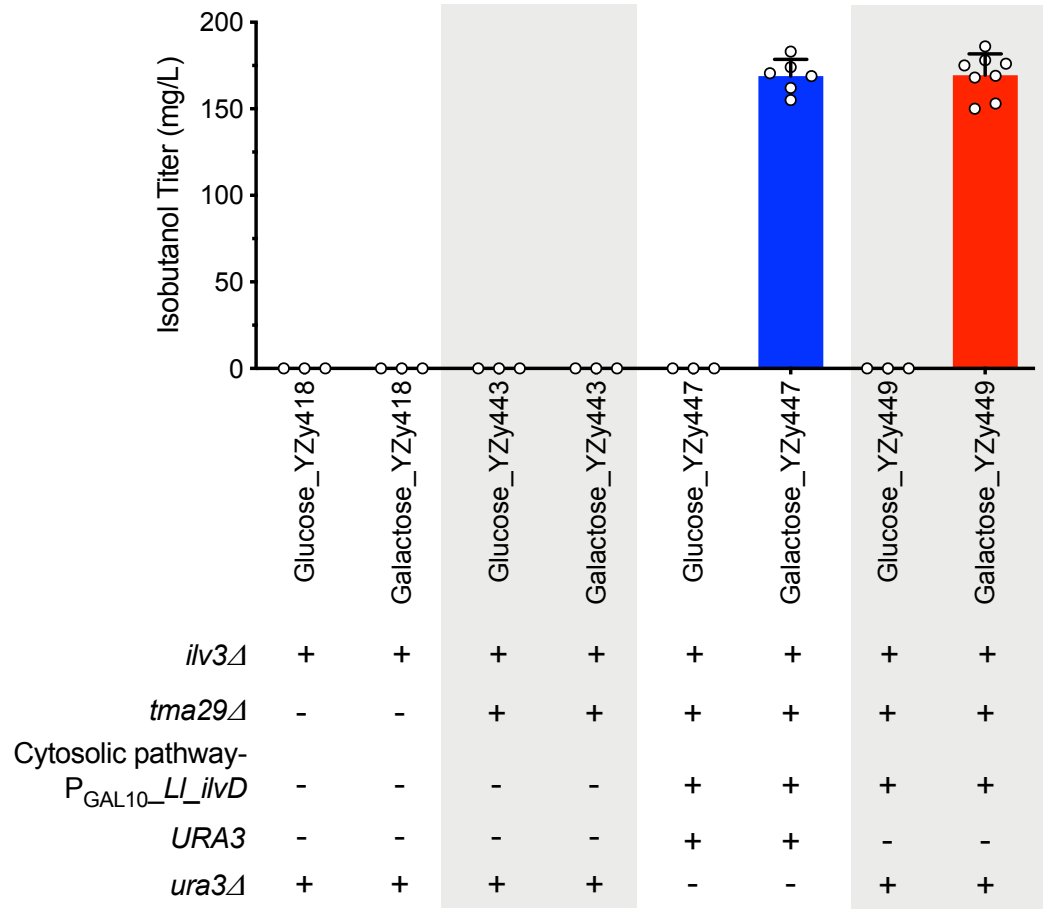

Supplementary Figure 16. Isobutanol production from glucose and galactose in engineered strains with or without galactose-inducible *Ll_ilvD*. Strains were fermented for 48h using 15% glucose or galactose as the carbon source. YZy418 and YZy443 produced no detectable isobutanol from either carbon source. All data are shown as mean values. Open circles represent individual data points. Error bars represent the standard deviation of at least three biological replicates. Source data are provided as a Source Data file.

Supplementary Figure 17

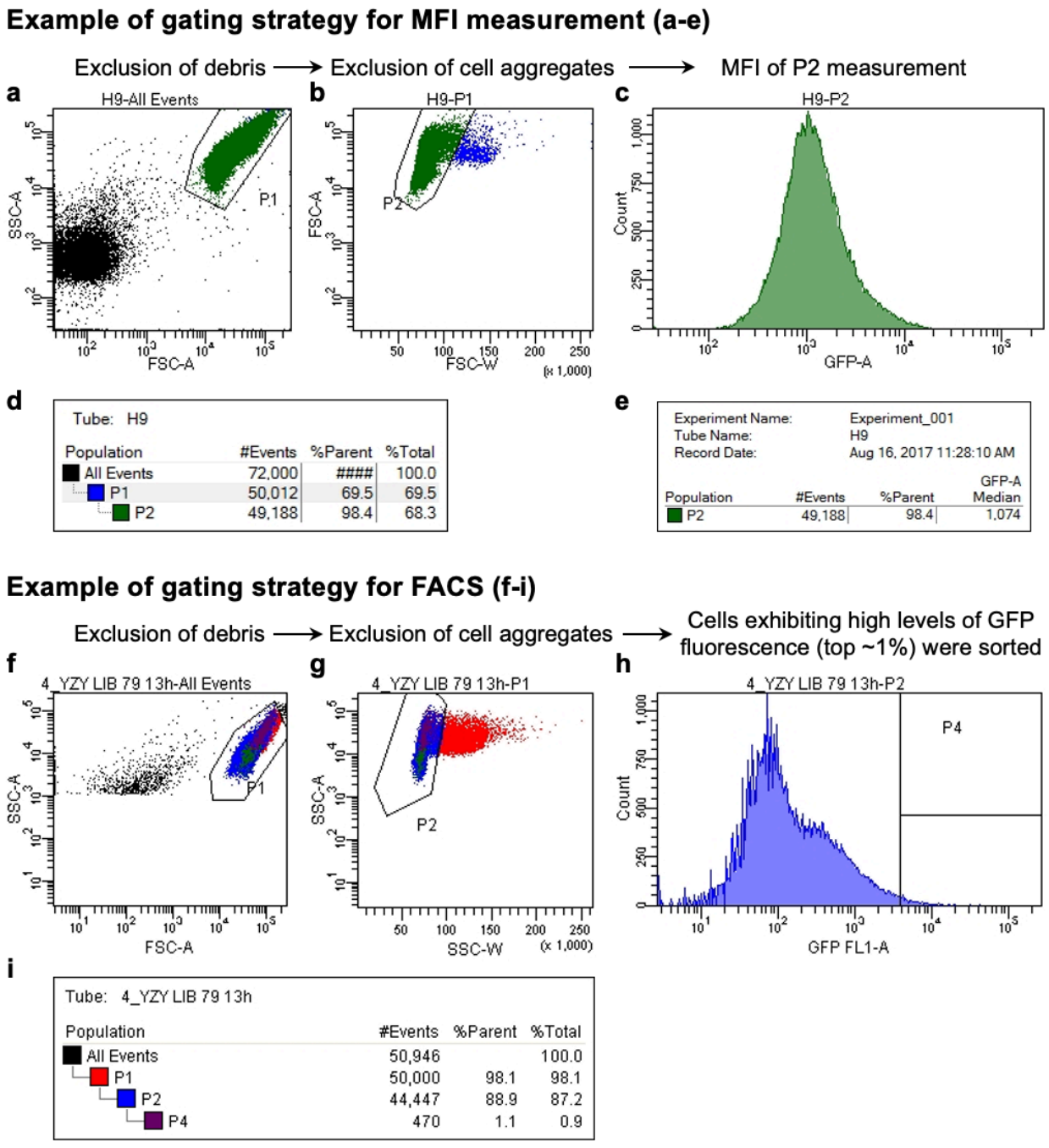

Supplementary Figure 17. Flow cytometry gating strategies for GFP median fluorescence intensity (MFI) measurement (a-e) and fluorescence activated cell sorting (FACS) (f-i). Cells were gated on forward scatter (FSC) and side scatter (SSC) signals to discard debris (**a** and **f**). We next plotted the FSC-width (FSC-W) against the FSC-area (FSC-A) (alternatively, SSC-W vs. SSC-A can also be used) to exclude the doublets and multiplets (**b** and **g).** After eliminating debris and cell aggregates, we measured the MFI of P2 (**c**). Cells exhibiting high levels of GFP fluorescence (top ~1%, P4) were sorted (**h**). The statistical tables are show in **d**, **e**, and **i**.

Supplementary References

1 Sze, J. Y., Woontner, M., Jaehning, J. A. & Kohlhaw, G. B. In vitro transcriptional activation by a metabolic intermediate: activation by Leu3 depends on alpha-isopropylmalate. *Science* **258**, 1143-1145, doi:10.1126/science.1439822 (1992).

2 Zhou, K. M., Bai, Y. L. & Kohlhaw, G. B. Yeast regulatory protein LEU3: a structure-function analysis. *Nucleic Acids Res* **18**, 291-298, doi:10.1093/nar/18.2.291 (1990).

3 Cavalieri, D. *et al.* Trifluoroleucine resistance and regulation of alpha-isopropyl malate synthase in Saccharomyces cerevisiae. *Mol Gen Genet* **261**, 152-160, doi:10.1007/s004380050952 (1999).

4 Hammer, S. K., Zhang, Y. & Avalos, J. L. Mitochondrial compartmentalization confers specificity to the 2-ketoacid recursive pathway: increasing isopentanol production in Saccharomyces cerevisiae. *ACS Synth Biol* **9**, 546-555, doi:10.1021/acssynbio.9b00420 (2020).

5 Mateus, C. & Avery, S. V. Destabilized green fluorescent protein for monitoring dynamic changes in yeast gene expression with flow cytometry. *Yeast* **16**, 1313-1323, doi:10.1002/1097-0061(200010)16:14<1313::AID-YEA626>3.0.CO;2-O (2000).

6 Weber-Ban, E. U., Reid, B. G., Miranker, A. D. & Horwich, A. L. Global unfolding of a substrate protein by the Hsp100 chaperone ClpA. *Nature* **401**, 90-93, doi:10.1038/43481 (1999).

7 Defenbaugh, D. A. & Nakai, H. A context-dependent ClpX recognition determinant located at the C terminus of phage Mu repressor. *J Biol Chem* **278**, 52333-52339, doi:10.1074/jbc.M308724200 (2003).

8 Martinez, V. *et al.* CRISPR/Cas9-based genome editing for simultaneous interference with gene expression and protein stability. *Nucleic Acids Res* **45**, e171, doi:10.1093/nar/gkx797 (2017).

9 Takpho, N., Watanabe, D. & Takagi, H. High-level production of valine by expression of the feedback inhibition-insensitive acetohydroxyacid synthase in Saccharomyces cerevisiae. *Metab Eng* **46**, 60-67, doi:10.1016/j.ymben.2018.02.011 (2018).

10 Ofuonye, E., Kutin, K. & Stuart, D. T. Engineering Saccharomyces cerevisiae fermentative pathways for the production of isobutanol. *Biofuels* **4**, 185-201, doi:10.4155/bfs.12.85 (2013).

11 Kopecky, J., Janata, J., Pospisil, S., Felsberg, J. & Spizek, J. Mutations in two distinct regions of acetolactate synthase regulatory subunit from Streptomyces cinnamonensis result in the lack of sensitivity to end-product inhibition. *Biochem Biophys Res Commun* **266**, 162-166, doi:10.1006/bbrc.1999.1792 (1999).

12 Kaplun, A. *et al.* Structure of the regulatory subunit of acetohydroxyacid synthase isozyme III from Escherichia coli. *J Mol Biol* **357**, 951-963, doi:10.1016/j.jmb.2005.12.077 (2006).

13 Hammer, S. K. & Avalos, J. L. Uncovering the role of branched-chain amino acid transaminases in Saccharomyces cerevisiae isobutanol biosynthesis. *Metab. Eng.* **44**, 302-312, doi:https://doi.org/10.1016/j.ymben.2017.10.001 (2017).

14 Rahman, M. M. *et al.* The Crystal Structure of a Bacterial l-Arabinonate Dehydratase Contains a [2Fe-2S] Cluster. *ACS Chem Biol* **12**, 1919-1927, doi:10.1021/acschembio.7b00304 (2017).

15 Entian, K.-D. & Kötter, P. 25 yeast genetic strain and plasmid collections. *Methods in microbiology* **36**, 629-666 (2007).
16 Sikorski, R. S. & Hieter, P. A system of shuttle vectors and yeast host strains designed for efficient manipulation of DNA in Saccharomyces cerevisiae. *Genetics* **122**, 19 (1989).
17 Christianson, T. W., Sikorski, R. S., Dante, M., Shero, J. H. & Hieter, P. Multifunctional yeast high-copy-number shuttle vectors. *Gene* **110**, 119-122 (1992).
18 Zhao, E. M. *et al.* Optogenetic regulation of engineered cellular metabolism for microbial chemical production. *Nature* **555**, 683-687, doi:10.1038/nature26141 (2018).
19 Zhang, Y. *et al.* Xylose utilization stimulates mitochondrial production of isobutanol and 2-methyl-1-butanol in Saccharomyces cerevisiae. *Biotechnol Biofuels* **12**, 223, doi:10.1186/s13068-019-1560-2 (2019).
20 Zhao, E. M. *et al.* Design, characterization, and modeling of rapid optogenetic inverter circuits for dynamic control in yeast metabolic engineering, Under review. (2020).
21 Goldstein, A. L. & McCusker, J. H. Three new dominant drug resistance cassettes for gene disruption in Saccharomyces cerevisiae. *Yeast* **15**, 1541-1553, doi:10.1002/(SICI)1097-0061(199910)15:14<1541::AID-YEA476>3.0.CO;2-K (1999).
22 Avalos, J. L., Fink, G. R. & Stephanopoulos, G. Compartmentalization of metabolic pathways in yeast mitochondria improves the production of branched-chain alcohols. *Nat Biotechnol* **31**, 335-341, doi:10.1038/nbt.2509 (2013).
23 Gueldener, U., Heinisch, J., Koehler, G. J., Voss, D. & Hegemann, J. H. A second set of loxP marker cassettes for Cre-mediated multiple gene knockouts in budding yeast. *Nucleic Acids Res* **30**, e23, doi:10.1093/nar/30.6.e23 (2002).
24 Atsumi, S., Li, Z. & Liao, J. C. Acetolactate synthase from Bacillus subtilis serves as a 2-ketoisovalerate decarboxylase for isobutanol biosynthesis in Escherichia coli. *Appl Environ Microbiol* **75**, 6306-6311, doi:10.1128/AEM.01160-09 (2009).
25 Brinkmann-Chen, S. *et al.* General approach to reversing ketol-acid reductoisomerase cofactor dependence from NADPH to NADH. *Proc Natl Acad Sci U S A* **110**, 10946-10951, doi:10.1073/pnas.1306073110 (2013).
26 Urano, J. E., CO, US), Dundon, Catherine Asleson (Englewood, CO, US). Cytosolic isobutanol pathway localization for the production of isobutanol. United States patent (2012).
27 Batrakou, D. G., Heron, E. D. & Nieduszynski, C. A. Rapid high-resolution measurement of DNA replication timing by droplet digital PCR. *Nucleic Acids Res* **46**, e112, doi:10.1093/nar/gky590 (2018).
28 Kohlhaw, G. B. Leucine Biosynthesis in Fungi: Entering Metabolism through the Back Door. *Microbiol Mol Biol R* **67**, 1-15, doi:10.1128/mmbr.67.1.1-15.2003 (2003).
29 Hazelwood, L. A., Daran, J. M., van Maris, A. J. A., Pronk, J. T. & Dickinson, J. R. The ehrlich pathway for fusel alcohol production: a century of research on Saccharomyces cerevisiae metabolism. *Appl Environ Microb* **74**, 2259-2266, doi:10.1128/Aem.02625-07 (2008).